Witnessing entanglement in trapped-ion quantum error correction under realistic noise

Andrea Rodriguez-Blanco,[1,*] Farid Shahandeh,[2] and Alejandro Bermudez[3]
[1]*Departamento de Física Teorica, Universidad Complutense de Madrid, 28040 Madrid, Spain*
[2]*Department of Computer Science, Royal Holloway, University of London, Egham TW20 0EX, United Kingdom*
[3]*Instituto de Física Teórica, UAM-CSIC, Universidad Autónoma de Madrid, Cantoblanco, 28049 Madrid, Spain*

(Received 18 September 2023; revised 22 March 2024; accepted 26 March 2024; published 10 May 2024)

Quantum error correction (QEC) exploits redundancy by encoding logical information into multiple physical qubits. In current implementations of QEC, sequences of nonperfect two-qubit entangling gates are used to codify the information redundantly into multipartite entangled states. Also, to extract the error syndrome, a series of two-qubit gates are used to build parity-check readout circuits. In the case of noisy gates, both steps cannot be performed perfectly, and an error model needs to be provided to assess the performance of QEC. We present a detailed microscopic error model to estimate the average gate infidelity of two-qubit light-shift gates used in trapped-ion platforms. We analytically derive leading-error contributions in terms of microscopic parameters and present effective error models that connect the error rates typically used in phenomenological accounts to the microscopic gate infidelities hereby derived. We then apply this realistic error model to quantify the multipartite entanglement generated by circuits that act as QEC building blocks. We do so by using entanglement witnesses, complementing in this way the recent studies in Ref. [Phys. Rev. X **12**, 011032 (2022); PRX Quantum **2**, 020304 (2021)] by exploring the effects of a more realistic microscopic noise.

DOI: 10.1103/PhysRevA.109.052417

I. INTRODUCTION

Fault-tolerant quantum computation promises to solve hard computational problems by harnessing the power inherent in the laws of quantum physics [1]. In this way, quantum computers have the potential to outperform their classical counterparts for certain computations [2], and great efforts are being devoted to their development using various experimental platforms [3]. However, the sensitivity of these quantum systems to the interactions with the environment as well as the unavoidable imperfections of the quantum operations used to control them lead to processing errors that pose a hurdle for bringing these devices to the large scales required for useful quantum computations. At present, specific tasks have been designed where such noisy intermediate-scale quantum (NISQ) [4] computers can display quantum advantage with respect to classical devices, even in the presence of errors [5,6]. To benefit from such advantages in more generic algorithms, a possible solution is to fight against error accumulation by active quantum error correction (QEC) [7–9]. Using this strategy, the quantum information is encoded redundantly in logical qubits composed of multiple physical qubits using specific QEC codes. Such logical encodings allow for the detection and correction of the errors that occur during the computation without gaining any knowledge of the encoded information (and thus, without perturbing the quantum state by measurement) and the fed-forward correction operation. Since the operations used to infer and correct errors and those used to manipulate ancillary qubits will also be faulty, all operations on the quantum register must obey a fault-tolerant (FT) circuit design [10], ensuring that errors do not spread uncontrollably through the quantum register during the computation. These FT considerations usually entail an increase in the circuit complexity and, importantly, set stringent conditions for the accuracy of each gate [11,12].

Among the architectures for large-scale FT quantum computers, trapped ions provide one of the most promising platforms [13]. We note that there are different ion species, various possible qubit encodings, different ion-trap hardware, and a variety of quantum-information processing schemes. Although the performance and scaling capabilities of each of these approaches can vary, we can draw the following picture of current capabilities. In general, state preparation is achieved by illuminating the ions with laser radiation and exploiting optical-pumping schemes, which yields low error rates on the order of 10^{-3} to 10^{-4} [14]. The accuracy of state detection, which relies on collecting photons from a state-dependent fluorescence, depends on the specific qubit encoding as well as the scheme for collecting the scattered photons and the collection time. In general, measurements are performed with low error rates also on the order of 10^{-3}, while the 10^{-4} level can be achieved in specific cases [14]. Trapped-ion qubits also provide excellent realizations of quantum memory. When encoded in the ground-state manifold, relaxation T_1 times are essentially infinite, and decoherence T_2 times can reach seconds by using mu-metal magnetic-field shielding to minimize the dephasing noise [15]. By exploiting qubit states that are first-order insensitive to Zeeman shifts, as used in trapped-ion clocks, the coherence time can be even further increased [14].

*Present address: University of California, Berkeley, California, USA; rodriguezblanco@berkeley.edu

Quantum information can also be processed in qubit registers corresponding to trapped-ion crystals with remarkable levels of performance. High-fidelity single-qubit rotations have been achieved for all different qubit encodings, by shining either laser or microwave radiation onto the ions, achieving errors in the 10^{-2}–10^{-6} range [13]. Laser-driven single-qubit gates for Zeeman qubits which exploit two-photon transitions (discussed below in more details) have achieved error rates of 10^{-2} [15] which can be lowered to 10^{-3} by using rf radiation [16] at the expense of individual qubit addressing. Note that these numbers also include state-preparation and measurement errors and the subsequent randomized benchmarking [17] experiments have singled out the gate contribution to the error to be on the order of 10^{-4}.

Together with a two-qubit entangling gate, these operations lead to a universal gate set for quantum information processing and, combined with state preparations and measurements, allow for flexible trapped-ion computations which have enabled the very first implementations of several quantum algorithms such as a scalable Shor's factorization algorithm, quantum chemistry algorithms, and portfolio optimization. [18–20]. One should note that the two-qubit entangling gates typically display a higher error in comparison to other quantum operations which lies in the 10^{-2}–10^{-3} range and depends on the specific ion encoding and the gate scheme [13]. Mølmer-Sørensen gates [21,22] have reached an error on the order of 10^{-3} level using hyperfine [23] and optical [24] qubits. Among other schemes [25,26] that have stimulated high-fidelity implementations of entangling gates [27,28], the so-called light-shift gates [29] have reached errors as low as 10^{-3} for hyperfine qubits [30,31]. We also note that one of the advantages of trapped ions with respect to other solid-state platforms is the programmable connectivity of the two-qubit gates. Using accurate and fast ion-crystal reconfigurations, typically referred to as ion shuttling [32,33], it is possible to perform an entangling gate on any desired qubit pair [34–38]. Alternatively, in static ion crystals, any desired pair of qubits is individually addressed by laser beams and interactions mediated by radial phonons to achieve programmable entangling gates [39–41].

For Zeeman qubits, current light-shift gates have errors on the order of 10^{-2} and thus, fall short of the topological codes' fault-tolerance requirements [9].

Regardless of the qubit encoding, and the specific thresholds of the QEC strategy, one can see that current entangling-gate errors are a major bottleneck for increasing the depth of trapped-ion quantum circuits. It is also important to improve the two-qubit gates for the demonstration of practical advantages of QEC encodings where the encoded logical operations are expected to improve upon those performed on bare physical qubits. In this context, it is crucial to have realistic models of the microscopic errors that go beyond a single number and can be incorporated in the simulations of the corresponding circuits. The resulting models are then used to assess the performance and the required improvements of the current hardware and software, guiding near-term developments. There has been recent progress in this direction in the context of optical trapped-ion qubits [42–45], as well as hyperfine qubits [46–50]. The native set of operations, as in the case of optical qubits [51], includes the entangling Mølmer-Sørensen gate and ion-crystal reconfigurations [33]. In contrast, this type of study has not been carried out for Zeeman qubits with other entangling gates.

In this paper, we fill this gap by presenting a detailed microscopic error model for two-qubit light-shift gates. Various sources of state infidelities for light-shift gates have previously been discussed in the literature [52,53] in parallel with Mølmer-Sørensen gates [22]. Such microscopic derivations are very useful, as they provide insight into different contributions to errors (i.e., error budget) and experimental optimizations to minimize them. Note, however, that these estimations focus on a single target state that would be produced by the ideal gate acting on a single initial state. Nonetheless, the same entangling gates in a larger circuit will typically act on a variety of initial states and could exhibit a different error. Hence, it is desirable to obtain estimations for the gate infidelity which averages over the initial states. Moreover, it is desirable to relate these estimates to an accurate microscopic model of the noisy quantum dynamics as addressed for Mølmer-Sørensen gates [42,44]. This model is not characterized by a single quantum number, but rather by a dynamical quantum map that faithfully describes the noisy gate. The effective noise channels can then be used to study the performance of QEC primitives, going beyond the oversimplified phenomenological and circuit noise models.

As noted above, QEC exploits redundancy to protect logical information from external noise and correct errors. The encoded logical qubits typically display entanglement [54], and there is indeed a very interesting interplay between entanglement and QEC codes [55–58]. Following this connection, the generation and verification of entangled states can be used as a benchmarking protocol for QEC primitives, as advocated recently in Refs. [38,58]. In these works, key aspects of QEC circuits are characterized in terms of their power to generate maximally entangled output states, which can be efficiently and robustly witnessed when the QEC codes are described under the stabilizer formalism [1,59]. To model the noise at the circuit level, these works use an idealized depolarizing channel. In this paper, we take further steps in this direction, evaluating and comparing the performance of the witnessing methods under a microscopic trapped-ion noise model for Zeeman qubits and light-shift gates. We focus on entanglement witnesses that can be efficiently inferred from experimental data, those in which the number of measurements scales linearly with the number of qubits.

The paper is organized as follows: In Sec. II, we present the primitives of the topological QEC code we wish to characterize. We show the compilation of those QEC circuits into the trapped-ion native gates set and introduce the entanglement tests we use to characterize the aforementioned circuits in terms of their ability to generate maximally entangled output states. In Sec. III, we revise the construction of the entangling light-shift gate in terms of laser-ion interaction Hamiltonians. We then derive a microscopic noise model for this unitary under nonideal conditions and present effective error models for the entangling light-shift gate, which now connect the error probability of each model to the microscopic gate infidelities. Finally, in Sec. IV, we analyze the results of witnessing maximally entangled states for these trapped-ion QEC circuits with realistic noise.

II. QUANTUM ERROR CORRECTION PRIMITIVES, FAULT TOLERANCE, AND ENTANGLEMENT

Trapped-ion quantum computers are one of the leading experimental platforms in experimental QEC [60–67]. Recent experiments with trapped ions [37,38,68,69] have employed color codes [70], a family of topological QEC codes [9], in order to detect and correct errors in a fault-tolerant manner. In particular, these works have employed FT constructions via the so-called flag ancilla qubits [71–73] which have been used for an FT measurement of the stabilizers [38], a demonstration of repetitive rounds of fault-tolerant QEC cycles interleaved with logical operations [37,69], and implementing a universal set of logical single and two-qubit operations [68]. The target of these studies has mainly been the smallest-possible color code which corresponds to the 7-qubit Steane code [74]. In this work, we choose to work with this distance-3 topological color code and focus on the specific stabilizer measurements.

A. Stabilizer codes

A stabilizer QEC code of type $[[n_c, k, d]]$ encodes k logical qubits into n_c physical qubits with a code distance d, and can correct up to $t = \lfloor (d-1)/2 \rfloor$ errors. The stabilizers S are operators that act on the Hilbert space of physical qubits $\mathcal{H} = \mathbb{C}^{2n_c}$ and form an Abelian subgroup $\mathcal{S}_G$ of the n-qubit Pauli group $\mathcal{P}_{n_c} = \times\{c_0 I, c_1 X, c_2 Y, c_3 Z : \ c_i \in \{\pm 1, \pm \mathrm{i}\}\}^{\otimes n_c}$, where I, X, Y, Z are the identity and the single-qubit Pauli matrices. This group is obtained by taking n-fold tensor products of these Pauli matrices, and can also include the multiplicative factors $\pm 1, \pm i$. The stabilizer subgroup, which must fulfill $-I^{\otimes n_c} \notin \mathcal{S}_G$, has $|\mathcal{S}_G| = 2^G$ elements that can be generated by a subset of G linearly independent and mutually commuting Pauli operators, $g = \{g_i\}_{i=1}^{G}$. These generators, commonly known as *parity checks*, are Hermitian and involutory operators within the Pauli group $g_i^\dagger = g_i \in \mathcal{P}_{n_c} : g_i^2 = I^{\otimes n_c}$. Accordingly, any element of the stabilizer $S \in \mathcal{S}_G = \langle g_1, \ldots, g_G \rangle$ can be obtained as a certain product of generators specified by the indexing set $\mathcal{I}$:

$$S = \prod_{i \in \mathcal{I}} g_i \quad \text{with} \quad g_i \in g \; \forall \; i \in \mathcal{I}. \tag{1}$$

In light of the above constraints, the parity checks correspond to a set of compatible observables with ± 1 eigenvalues, such that the measurement of one of them projects the state onto a 2^{n_c-1}-dimensional subspace of the n_c-qubit Hilbert space $\mathcal{H}$. Since the parity checks commute, it is possible to unambiguously specify a 2^{n_c-G}-dimensional subspace through their common $+1$ eigenspace, namely,

$$\mathcal{L} = \{|\psi\rangle \in \mathbb{C}^{2n_c} : S|\psi\rangle = |\psi\rangle \; \forall \; S \in \mathcal{S}_G\}. \tag{2}$$

The subspace $\mathcal{L} \subset \mathcal{H}$ is known as the *code space* and can be used to embed or codify $k = n_c - G$ logical qubits. The logical operators $\{X_\ell^L, Z_\ell^L\}_{\ell=1}^{k} \notin \mathcal{S}_G$ correspond to Hermitian elements of the Pauli group $\mathcal{P}_n$ that commute with any stabilizer $[X_\ell^L, S] = [Z_\ell^L, S] = 0 \; \forall \; S \in \mathcal{S}_G$ and, thus, act nontrivially within the code space $X_\ell^L, Z_\ell^L : \mathcal{L} \to \mathcal{L}$. Moreover, they are required to fulfill the corresponding algebra for k independent logical qubits $(X_\ell^L)^2 = (Z_\ell^L)^2 = I^{\otimes n_c}$, and $X_\ell^L Z_{\ell'}^L = (1 - 2\delta_{\ell,\ell'}) Z_{\ell'}^L X_\ell^L, \; \forall \ell, \; \ell' \in \{1, \ldots, k\}$. Topological QEC codes are a specific type of stabilizer code in which the parity checks have local support on a lattice where the physical qubits reside, whereas the logical qubits are encoded in global topological properties. For instance, in topological color codes [70], the physical qubits are arranged on the vertices of a trivalent three-colorable planar lattice (see, e.g., Fig. 1 for the smallest-distance color code). The parity check operators are the following pair of X- and Z-type operators per plaquette q, and have local support, acting only on those qubits located at the plaquette vertices

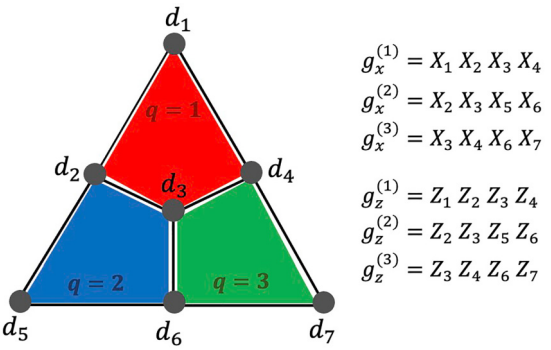

FIG. 1. Schematics of the standard $d = 3$ topological color code. The $n_c = 7$ physical data qubits that encode the logical qubit lay on the vertices of the three colorable plaquettes. There are two parity-check per colorable plaquette q: $g_x^{(q)}$ for detecting single qubit phase-flip errors, and $g_z^{(q)}$ for detecting bit-flip errors. That makes a total of $G = 6$ parity checks, leading to $k = n_c - G = 1$ logical qubits.

$$g_x^{(q)} = \bigotimes_{i \in v(q)} X_i, \quad g_z^{(q)} = \bigotimes_{i \in v(q)} Z_i, \tag{3}$$

where $v(q)$ is the set of vertices that belong to plaquette q. As depicted in Fig. 1, this color code has $n_c = 7$ physical qubits and $G = 6$ parity checks, each of which acts locally on only four qubits (i.e., weight-4 parity checks), so that the code space is two-dimensional $\dim \mathcal{L} = 2^{7-6} = 2$, encoding $k = n_c - G = 1$ logical qubit. Up to deformations by application of parity checks, the logical operators correspond to strings of Pauli operators along the sides of the triangle $X_L = X_5 X_6 X_7$, $Z_L = Z_1 Z_4 Z_7$, which clearly show that the distance of the code is $d = 3$, such that it can correct $t = 1$ error. These errors are typically referred to as single-qubit bit- and phase-flip errors $E \in \{X_i, Z_i\}_{i=1}^{7}$, and anticommute with some of the parity checks. Accordingly, the measurement of parity checks provides an error syndrome $s = \{s_x^{(1)}, s_x^{(2)}, s_x^{(3)}, s_z^{(1)}, s_z^{(2)}, s_z^{(3)}\}$, where $s_\alpha^{(q)} = \pm 1$, and $\alpha = x, z$, which allows inferring, and subsequently correcting, the most likely error $|\Psi(0)\rangle = c_0|0\rangle_L + c_1|1\rangle_L \mapsto E|\Psi(0)\rangle$ without obtaining any information about c_0 and c_1.

B. Trapped-ion parity-check measurements

Let us now discuss how the parity check measurements are performed in practice, considering a specific implementation based on trapped ions. The native trapped-ion entangling gates in current designs are not CNOT gates [1]. Instead, they are based on state-dependent dipole forces and effective phonon-mediated interactions that dynamically generate entanglement

between distant qubits [21,22,29,75,76]. In this work, we are concerned with Z-type state-dependent forces. These forces, which stem from bichromatic laser beams in a Λ-scheme configuration (see Fig. 4) in a specific parameter regime, will be discussed in the following section. Under certain conditions, we show that these forces give rise to the entangling light shift gates [29,35], namely,

$$U_{i,j}^{ZZ}(\theta) = e^{-\mathrm{i}\frac{\theta}{2}Z_iZ_j}, \tag{4}$$

where θ is the corresponding pulse area. This unitary leads to a fully entangling gate for $\theta = \pi/2$, i.e., they map product states onto GHZ-type entangled states. They are denoted by the symbol $U_{i,j}^{ZZ}(\pi/2) = \overset{i}{\underset{j}{\blacksquare\!\!-\!\!\blacksquare}}$ in the circuits below. In addition, we also consider single-qubit rotations. In particular, the unitaries

$$R_i^Z(\theta) = e^{-\mathrm{i}\frac{\theta}{2}Z_i} \tag{5}$$

are obtained by local ac-Stark shifts [77] and correspond to rotations about the z axis of the Bloch's sphere of each qubit. Rotations about an axis contained in the equatorial plane of the Bloch sphere are obtained by the driving of the so-called carrier transition [78], which leads to

$$R_{\phi,i}^{\perp}(\theta) = e^{-\mathrm{i}\frac{\theta}{2}\sum_i(\cos\phi X_i + \sin\phi Y_i)}. \tag{6}$$

With this notation, $R_{0,i}^{\perp}(\theta)$ and $R_{\pi/2,i}^{\perp}(\theta)$ correspond to rotations around x and y axes of the Bloch sphere, respectively. We note that, although these rotations act on all illuminated ions, the equatorial rotations can be applied to a particular set of ions by using spin-echo-type refocusing pulses that interleave these rotations with the addressable Z-type rotations [79]. Alternatively, one can also use laser addressing techniques for both single and two-qubit gates [39–41,80].

Although this collection of gates is not the standard one in quantum computation [1], it forms a universal gate set, so that any quantum algorithm can be decomposed into a sequence of such elementary operations [51,79]. Let us now discuss how this native gate set can be used for the measurement of the parity checks. Since we cannot measure the physical qubits directly, as this would project the state and thus perturb the encoded quantum information, the measurement needs to be performed on a set of ancillary qubits into which the parity-check information has been previously mapped. In principle, this would require an ancilla qubit per plaquette. In the following, we focus on a single plaquette and thus restrict momentarily to a single ancilla qubit, which we initialize in state $|+\rangle_s$, where the subscript refers to the syndrome readout and $|\pm\rangle_s = (|0\rangle_s \pm |1\rangle_s)/\sqrt{2}$. We note that the action of the maximally entangling light-shift gate and a single rotation on the target qubit about the z axis is equivalent, up to an irrelevant global phase, to a controlled-Z gate $\mathrm{CZ}_{c,t} = |0_c\rangle\langle 0_c| \otimes 1_t + |1_c\rangle\langle 1_c| \otimes Z_t$,

$$\begin{aligned}\mathrm{CZ}_{c,t} &= R_c^Z(-\pi/2)R_t^Z(-\pi/2)\ \overset{c}{\underset{t}{\blacksquare\!\!-\!\!\blacksquare}} \\ &= \overset{c}{\underset{t}{\blacksquare\!\!-\!\!\blacksquare}}\ R_t^Z(-\pi/2)R_c^Z(-\pi/2).\end{aligned} \tag{7}$$

In addition, the Hadamard gate $H_i = |+_i\rangle\langle 0_i| + |-_i\rangle\langle 1_i|$ can be decomposed, again up to an irrelevant global phase, as

$$H_i = R_i^Z(\pi)R_{\pi/2,i}^{\perp}(-\pi/2) = R_{\pi/2,i}^{\perp}(\pi/2)R_i^Z(\pi). \tag{8}$$

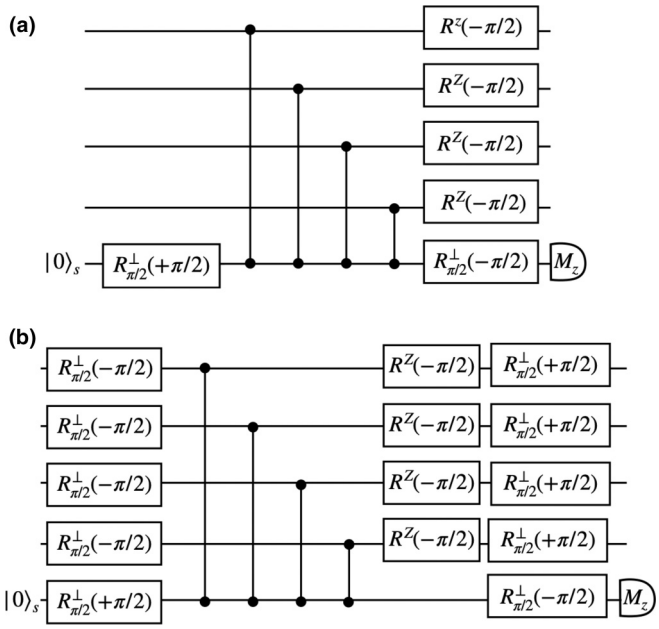

FIG. 2. Parity-check measurement circuit using the native trapped-ion gates. (a) Z-type parity checks, (b) X-type parity checks.

With these identities, it is straightforward to construct the circuits for the measurement of parity checks (3) starting from the generic circuit for measuring Hermitian involutory operators [1]. For the Z-type parity checks, the circuit is that of Fig. 2(a) which is obtained by using Eq. (7) for each of the target physical qubits together with Eq. (8) for the syndrome ancillary qubit. The latter can be simplified by noting that the action of the rotations about the z axis becomes trivial when acting on the initial state, or prior to the measurement M_z in the Z basis. For the X-type parity checks, the circuit is that of Fig. 2(b), and can be obtained by applying the Hadamard gate (8) to all physical qubits twice, right before and right after the gates of Fig. 2(a), which rotates the controlled-Z operations to the CNOTs required for the measurements of the X-type plaquette operators. For each of the Hadamards, one can choose a specific ordering (8) to simplify the circuits considering their commutation with the light-shift gates (4).

In this work, we are interested in assessing this QEC building block from the perspective of multipartite entanglement. We note that for an arbitrary state of the physical qubits $|0_s\rangle|\psi\rangle \mapsto |0_s\rangle\frac{1}{2}(I^{\otimes n} + g_\alpha^{(q)})|\psi\rangle + |1_s\rangle\frac{1}{2}(I^{\otimes n} - g_\alpha^{(q)})|\psi\rangle$, such that the measurement M_z on the ancilla qubit projects the state onto the respective ± 1 eigenspace of the parity check, giving access to the complete error syndrome $\{s_\alpha^{(q)}\}$ when performed over all plaquettes. To characterize this QEC primitive using its ability to generate multipartite entanglement, we dispense with the ancilla using a rotation about the y axis followed by a Z measurement in the circuit of a single X-type plaquette [cf. Fig. 2(b)]. Considering the specific initial state $|\psi_{+,z}\rangle = |0, 0, 0, 0\rangle$, one readily sees that a 5-qubit GHZ state

is produced deterministically,

$$|\psi_{+,z}\rangle|0_s\rangle \mapsto \frac{1}{\sqrt{2}}(|0\rangle^{\otimes 5} + |1\rangle^{\otimes 5}) = \left|\mathrm{GHZ}^5_{z,+}\right\rangle. \tag{9}$$

Analogously, in the circuit of a single Z-type plaquette [cf. Fig. 2(a)], we dispense with the ancilla using a single rotation about the z axis, $R^Z_s(\pi)$, prior to the last rotation of ancilla about the y axis followed by a Z measurement such that, altogether, they lead to the Hadamard gate (8). If we now consider the initial state $|\psi_{+,x}\rangle = |+,+,+,+\rangle$, one readily sees that a 5-qubit GHZ state is produced deterministically,

$$|\psi_{+,x}\rangle|0_s\rangle \mapsto \frac{1}{\sqrt{2}}(|+\rangle^{\otimes 5} + |-\rangle^{\otimes 5}) = \left|\mathrm{GHZ}^5_{x,+}\right\rangle. \tag{10}$$

Both of these states are maximally entangled. Let us note that none of the above schemes are fault-tolerant, as a single qubit error could propagate through the entangling gates, which leads to a pair of errors. Such errors could not be corrected by the small 7-qubit color code. To see that, recall the error-propagation relations [58]

$$\begin{aligned} \overset{c}{\underset{t}{\bullet}}\!\!-\!\!\!\oplus\; X_c = Y_c Z_t \;\overset{c}{\underset{t}{\bullet}}\!\!-\!\!\!\oplus, \quad & \overset{c}{\underset{t}{\bullet}}\!\!-\!\!\!\oplus\; X_t = Z_c Y_t \;\overset{c}{\underset{t}{\bullet}}\!\!-\!\!\!\oplus, \\ \overset{c}{\underset{t}{\bullet}}\!\!-\!\!\!\oplus\; Z_c = Z_c \;\overset{c}{\underset{t}{\bullet}}\!\!-\!\!\!\oplus, \quad & \overset{c}{\underset{t}{\bullet}}\!\!-\!\!\!\oplus\; Z_t = Z_t \;\overset{c}{\underset{t}{\bullet}}\!\!-\!\!\!\oplus. \end{aligned} \tag{11}$$

Accordingly, phase-flip errors commute through the gates and no further errors are triggered. On the other hand, the bit flip errors occurring on any of the two qubits are rotated into a Y-type error, and also triggers an additional phase-flip error in the other qubit. In light of this, recalling propagation rules for Y-type errors is also useful:

$$\overset{c}{\underset{t}{\bullet}}\!\!-\!\!\!\oplus\; Y_c = X_c Z_t \;\overset{c}{\underset{t}{\bullet}}\!\!-\!\!\!\oplus, \quad \overset{c}{\underset{t}{\bullet}}\!\!-\!\!\!\oplus\; Y_t = Z_c X_t \;\overset{c}{\underset{t}{\bullet}}\!\!-\!\!\!\oplus. \tag{12}$$

In both circuits (a) and (b) of Fig. 2, we see that a bit-flip error between the second and the third light-shift gates results in a pair of phase-flip errors in the plaquette, which leads to an uncorrectable error in the 7-qubit code. On the contrary, phase-flip errors do not lead to this cascading of errors and, as shall be discussed below, circuits based on light-shift gates can be beneficial for certain biased noise models.

A possibility to make parity-check circuits fault tolerant (FT) is to add as many ancilla qubits as the weight of the parity checks [42]. This method requires preparing and verifying those ancillae in a GHZ state [81,82], which increases the complexity of the trapped-ion circuits considerably, and thus, requires further improvements before one can see the benefits of QEC [42]. More recent FT schemes exploit the so-called flag qubits, which are ancillary qubits introduced to detect the dangerous cascading of errors. The flag-based technique reduces qubit overhead and circuit complexity [44,71–73,83–86]. For the distance-3 color code, this technique uses a single additional ancilla, the *flag* qubit, which is coupled to the syndrome qubit by a pair of light-shift gates. These extra gates serve to detect the single-qubit errors that occur on the ancillary qubit and propagate into a pair of errors in the data qubits [see Fig. 3(a)]. These additional gates ensure that these weight-2 errors also propagate onto the flag qubit, which would be signalled by a -1 outcome of the flag-qubit measurement. The flag readout, when combined with the subsequent parity check measurements, can be used to unequivocally identify and deterministically correct dangerous errors, achieving the desired fault tolerance [44,71].

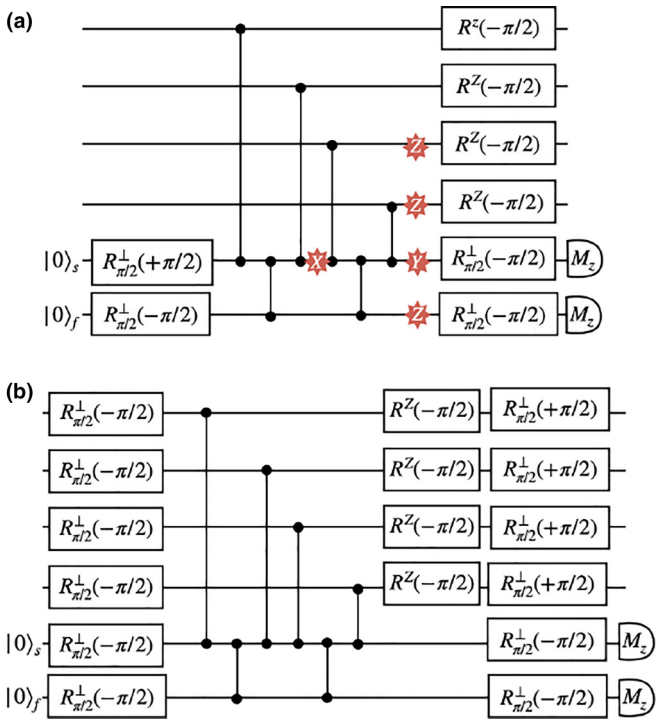

FIG. 3. Parity-check measurement circuit using flag qubits. (a) Z-type parity checks, (b) X-type parity checks.

In the present context, we instead consider a postselection scheme in which, after running the circuits from Fig. 3, one only keeps the events where the flag is not triggered, and the circuit generates the GHZ entangled states in Eqs. (9) and (10) depending on the initial state with the corresponding Z- or X-type stabilizer.

C. Entanglement witnesses for quantum error correction primitives

In this section, following the work presented in Ref. [38,58], we discuss how to quantify the capability of the parity-check circuits to generate maximally entangled states in the presence of noise. As argued in Ref. [58], verifying genuine multipartite entanglement is not an easy task as the number of bipartitions in which entanglement must be checked grows exponentially with the number of qubits. Moreover, in some cases, the required measurements designed theoretically are difficult to implement experimentally. An interesting strategy to overcome these limitations for entanglement detection is to use entanglement witnesses [87–91], which are observables signaling the entanglement of the state when a negative expectation value is obtained. Interestingly, entanglement witnesses can be constructed from local and experimentally friendly observables [58,92]. We consider noisy parity-check circuits using imperfect measurements in two different ways: (*i*) *standard linear witnessing* (SL) with a single witness that only relies on a linear number of measurements [92], and (*ii*) *conditional linear witnessing* (CL) that requires a linear number of witnesses and measurements [58].

Let us start by discussing how to construct these witness operators W_n for the parity-check circuits, following the design principles discussed in Refs. [92,93] for stabilizer states. An entanglement witness W is an observable whose expectation value is, by construction, non-negative $\mathrm{tr}(W\rho_s) \geqslant 0$ for all separable states $\rho_s = \sum_k p_k \rho_1^{(k)} \otimes \rho_2^{(k)} \otimes \cdots \otimes \rho_n^{(k)}$ [94]. Therefore, if the witness is negative for a certain state, $\mathrm{tr}(W\rho) < 0$, one can ascertain that ρ is not separable and, thus, that it contains some sort of entanglement. Note that, however, with the above definition of the witness using fully separable states with n parties, the witnessed entanglement may be present only within a specific bipartition of the system, whereas other bipartitions may be consistent with separability.

A stronger entanglement criteria is obtained by considering states that are not biseparable, i.e., those who do not admit a decomposition of the form $\rho_s = \sum_k p_k \rho_A^{(k)} \otimes \rho_B^{(k)}$ in any bipartition AB. A state possesses the strongest form of entanglement, namely, genuine multipartite entanglement (GME), if it further cannot be written as a convex combination of biseparable states with respect to different bipartitions.

If a noisy imperfect evolution produces a state ρ that is expected to be close to a target entangled n-qubit pure state $|\psi^{(n)}\rangle$, one can construct a projector-type witness

$$W_n = l_n \mathbb{I} - |\psi^{(n)}\rangle\langle\psi^{(n)}|, \tag{13}$$

where l_n is the smallest constant for which every biseparable state ρ_s satisfies $\mathrm{tr}(W_n\rho_s) \geqslant 0$ [92,93]. Accordingly, when the fidelity of a state with respect to the target entangled state fulfils $\mathcal{F} = \langle\psi^{(n)}|\rho|\psi^{(n)}\rangle > l_n$, the state is sufficiently close to the target state so that $\mathrm{tr}(W_n\rho) < 0$ and one concludes that ρ is indeed entangled. For the specific target states in Eqs. (9) and (10), the GME witness bound is $l_n = 1/2$ [93].

Depending on the specific target state, the above witnesses might be complicated observables with a large overhead in measurement complexity. In general, they require $2^{n-1} - 1$ different local Pauli measurements, which is exponential in the number of qubits n. This has motivated the development of alternative witnesses, such as the witnesses proposed by Tóth and Gühne [92,93], or the conditional witness method [58], both of which are efficient in the number of bipartitions in which entanglement must be checked. They reduce the overhead on the required number of measurements to n rather than $2^{n-1} - 1$.

We describe below both protocols by focusing on a specific type of entangled state. These are stabilizer states fulfilling

$$g_i|\psi^{(n)}\rangle = +|\psi^{(n)}\rangle \; \forall \; i \in \{1, \ldots, n\}, \tag{14}$$

where the n Hermitian, involutory, and mutually commuting operators of the Pauli group $g_i \in \mathcal{P}_n$ generate the stabilizer group $\mathcal{S}_n = \langle g_1, g_2 \ldots, g_n\rangle$, and uniquely determine the target entangled state $|\psi^{(n)}\rangle$. We note that the number of qubits of the multipartite state n should not be confused with the number of physical qubits in the code n_c and that, likewise, the stabilizer group associated with the state $\tilde{\mathcal{S}}_n$ should not be confused with that of the QEC codes $\mathcal{S}_G$ discussed above. In our case, the target state for the X-type (9) [Z-type (10)] circuit contains $n = 5$ qubits, such that the respective generators g_i^x (g_i^z) are not the two parity checks (3) of the corresponding plaquette, rather the two following sets:

$$g_i^x = Z_i Z_{i+1} \; \forall \; i \in \{1, \ldots, 4\}, \quad g_5^x = \prod_{i=1}^{5} X_i,$$
$$g_i^z = X_i X_{i+1} \; \forall \; i \in \{1, \ldots, 4\}, \quad g_5^z = \prod_{i=1}^{5} Z_i. \tag{15}$$

Note that, in light of the GHZ-type target states in Eqs. (9) and (10), one could also define the weight-2 parity checks as being composed of other pairs of physical qubits. This will be important when considering the robustness of the witness against biased noise.

The projector that appears in the general entanglement witness for n-partite pure states (13) can be expressed in terms of these stabilizer generators. In particular, the projector used in the construction of the witness can be obtained by the product of all projectors onto the $+1$ eigenspace of the generators $|\psi^{(n)}\rangle\langle\psi^{(n)}| = \prod_{i=1}^{n} \frac{1}{2}(I^{\otimes n} + g_i) = L_n$, where L_n will be denoted as the entanglement test operator. This operator contains all products of the stabilizers and, since they belong to the Pauli group, can be inferred from local measurements. However, the corresponding product increases the number of required measurement basis. We now discuss two witnesses that minimize the measurement overhead.

1. Standard linear witnessing

As discussed in Ref. [92], a GME witness that only requires a linear number of measurements can be defined by

$$W_n^{\mathrm{SL}} = (n-1)I^{\otimes n} - \sum_{i=1}^{n} g_i, \tag{16}$$

where $l_n = (n-1)$ is the corresponding entanglement bound [92]. In this case, the linear number of measurements is given by measuring the expectation value of the n generators of the target state, rather than all stabilizers. In this work, for convenience, we choose a normalized version

$$\widetilde{W}_n^{\mathrm{SL}} = \tilde{l}_n^{\mathrm{SL}} I^{\otimes n} - L_n^{\mathrm{SL}}, \tag{17}$$

where the test operator L_n^{SL} is the average of the generators

$$L_n^{\mathrm{SL}} = \frac{1}{n}\sum_{i}^{n} g_i, \tag{18}$$

and the witness bound is

$$\tilde{l}_n^{\mathrm{SL}} = \frac{n-1}{n}. \tag{19}$$

One can see that the expectation value of the test operator becomes $+1$ for the ideal GME states in Eqs. (9) and (10). If $\langle L_n^{\mathrm{SL}}\rangle$ surpasses the critical value of $\tilde{l}_n^{\mathrm{SL}}$, one would obtain $\langle\widetilde{W}_n^{\mathrm{SL}}\rangle < 0$, signaling a GME state of n qubits.

In the SL witnessing, we need to measure n different stabilizer generators, which could, in principle, require up to n different measurement settings. For the particular case of parity check circuits whose output states have CSS-type stabilizers [95], i.e., its generators g_i are formed of either X- or Z-type Pauli operators only as in Eqs. (15), it has been shown that the required number of measurement settings

reduces from n to just two settings: measuring all qubits in the X- and the Z- basis suffices to determine the expectation value of all operators contributing to the witness $\widetilde{W}_n^{\mathrm{SL}}$ [93]. For both, non-FT and FT circuits that allow us to measure the X-type parity checks, as shown in Fig. 2(b) and in Fig. 3(b), the target 5-qubit output state is $|\mathrm{GHZ}^5_{z,+}\rangle$, as given in Eq. (9). For the case of the FT-circuit, we obtain the target 5-qubit GME state after postselecting on the measurement events in which the flag-qubit is not triggered. This state is stabilized by the Z-type operators of Eq. (15) and, therefore, just two measurement settings are needed. Likewise, for the non-FT and FT Z-type circuits shown in Figs. 2(a) and 3(a), the target output state is given by the 5-qubit GME state $|\mathrm{GHZ}^5_{x,+}\rangle$ shown in Eq. (10). For the FT circuit, we again postselect on the flag qubit. In this case, the stabilizer generators are the x-type operators of Eq. (15), showing that two measurement settings suffice.

2. *Conditional linear witnessing*

With the same goal, namely, reducing the exponential number of bipartitions that need to be checked to a linear one, and hence, making the entanglement detection efficient, we have introduced conditional entanglement witnessing in Ref. [58] as a robust and efficient technique to test multipartite entanglement (ME) in quantum systems. For the conditional witness, we refer to the verification of ME instead of GME, following the definition as in Refs. [96,97]. In this definition, GME detection terminology is explicitly used for states that are not within the convex hull of all biseparable states, while ME describes the states that are not separable within any bipartition. We proved that, given an n-partite system, certification of entanglement between the subsystems s_1 and s_x for all $s_x \in \{s_1\}^{\mathrm{c}} = \{s_1, \ldots, s_n\} \setminus \{s_1\}$, conditioned on an outcome i of suitable local measurements on the remaining $n-2$ subsystems, is actually sufficient for the certification of ME. Moreover, the number of bipartitions needed to be checked gets reduced to $n-1$ [58]. In this case, the conditional entanglement witness has an analogous form as before in (17), namely,

$$W^{\mathrm{CL}} = l^{\mathrm{CL}}\mathbb{I} - L^{\mathrm{CL}}, \tag{20}$$

where L^{CL} is the conditional test operator, and l^{CL} is the corresponding witness bound. Let us now give the explicit expressions of the conditional witness for the 5-qubit target multipartite entangled state in Eqs. (9) and (10). In a standard scenario to certify n-party entanglement in a $n=5$ partite system, we would need to test entanglement in $N^b = 2^4 - 1 = 15$ bipartitions; a number that grows exponentially with the number of subsystems n. On the contrary, conditional entanglement achieves the verification of entanglement in a number of bipartitions that just grows linearly with the number of subsystems. The method works by localizing entanglement between two partitions of the 5-qubit multipartite system, by performing local measurements on the three remaining subsystems [98,99]. This reduces the exponential complexity of the n-party entanglement detection to a linear number of tests. For the particular case of study, it would be then enough to test entanglement in $n-1=4$ bipartitions instead of in 15. We are going to focus merely on the four bipartitions $[s_5|s_1]$, $[s_5|s_2]$, $[s_5|s_3]$, and $[s_5|s_4]$. In this case, within each bipartition, we check if each subsystem data qubit is entangled with the syndrome ancilla subsystem. However, a different choice of bipartitions is also valid. Then, for the certification of multipartite entanglement in the 5-qubit states from Eqs. (9) and (10), it suffices to test entanglement in each bipartition $[s_5|s_x]$ for $x \in \{1, 2, 3, 4\}$, conditioned on the outcome of a projective measurement on the remaining three qubits $s_{x'} \in \{s_5, s_x\}^{\mathrm{c}}$. The conditional entanglement test operators for each bipartition are

$$\begin{aligned} L^{\mathrm{CL,z}}_{[s_5|s_x]} &= \left|\mathrm{Bell}^{\mathrm{z}}_{s_5|s_x}\right\rangle\!\left\langle\mathrm{Bell}^{\mathrm{z}}_{s_5|s_x}\right| \otimes P^0_{\{s_5,s_x\}^c}, \\ L^{\mathrm{CL,x}}_{[s_5|s_x]} &= \left|\mathrm{Bell}^{\mathrm{x}}_{s_5|s_x}\right\rangle\!\left\langle\mathrm{Bell}^{\mathrm{x}}_{s_5|s_x}\right| \otimes P^+_{\{s_5,s_x\}^c}, \end{aligned} \tag{21}$$

where $L^{\mathrm{CL,z}}_{[s_5|s_x]}$ is the conditional test operator for the Z-type parity-check circuit output state, whereas $L^{\mathrm{CL,x}}_{[s_5|s_x]}$ is the conditional test operator for the X-type. In this case, in addition to the projector of the qubit pair s_5 and s_x onto the Bell state $|\mathrm{Bell}^{\mathrm{z}}\rangle = (|{+}{+}\rangle + |{-}{-}\rangle)/\sqrt{2}$, we condition on the projection of the remaining qubits into

$$P^0_{\{s_5,s_x\}^c} = \bigotimes_{s_{x'}\in\{s_5,s_x\}^c} \left|0_{s_{x'}}\right\rangle\!\left\langle 0_{s_{x'}}\right|. \tag{22}$$

The test operator in the X-type circuit for the bipartition $[s_5|s_x]$ is given by $L^{\mathrm{CL,x}}_{[s_5|s_x]}$. The main difference with respect to the Z-type conditional test operator is that now the projector on the remaining three qubits is

$$P^+_{\{s_5,s_x\}^c} = \bigotimes_{s_{x'}\in\{s_5,s_x\}^c} |{+}_{s_{x'}}\rangle\langle{+}_{s_{x'}}|, \tag{23}$$

and the conditional Bell pair is $|\mathrm{Bell}^{\mathrm{x}}\rangle = (|00\rangle + |11\rangle)/\sqrt{2}$.

The Bell pairs can be described in terms of the same weight-2 stabilizer generators $\{X_{s_x}X_{s_5}, Z_{s_x}Z_{s_5}\}$, so that the projector can be specified by the product of these two generators and, thus, the conditional test operators can be expressed as a linear combination of two-point correlations

$$L^{\mathrm{CL,x/z}}_{[s_5|s_x]} = \frac{I_{s_x}I_{s_5} + X_{s_x}X_{s_5} - Y_{s_x}Y_{s_5} + Z_{s_x}Z_{s_5}}{4}. \tag{24}$$

In addition, the entanglement bounds for Bell states are $l^{\mathrm{CL,x/z}}_{[s_5|s_x]} = 1/2$ [58,93] for all the bipartitions. Thus, the conditional test operator must surpass this value, $\langle L^{\mathrm{CL,x/z}}_{[s_5|s_x]}\rangle > 1/2$, in order to obtain a negative value for the conditional witness; that is, $\langle W^{\mathrm{CL,x/z}}_{[s_5|s_x]}\rangle < 0$.

In this occasion, we need three measurement settings $\{XX, ZZ, YY\}$ per bipartition. Hence, for the $n-1=4$ bipartitions, a total of twelve measurement settings would be required for this witnessing method. One can argue that this number is considerably higher than the two settings needed in the SL witness. However, this method has a larger witness bound. For the SL method, we have a $\tilde{l}^{\mathrm{SL}} = 5/6$, which is larger than the one required in the CL method, $l^{\mathrm{CL}} = 1/2$. This implies that, with the SL method, we lose sensitivity in the verification of entanglement. There are states that lie within the convex hull of all biseparable states that would not be detected by using the SL witness [58]. On the contrary, with the CL method, we build $n-1$ witnesses that can be tangent

to the set of biseparable states, thus increasing the sensitivity on detecting multipartite entanglement [58]. We see later in the text that the CL method is more robust than the SL against the circuit noise models considered.

III. ERROR MODEL FOR LIGHT-SHIFT GATES

So far, we have presented the native trapped-ion gate set in Eqs. (4)–(6) from a high-level perspective. This suffices to find trapped-ion compilations of specific circuits and analyze the propagation of generic phenomenological errors, as discussed in the previous section. However, in order to give a realistic account of the performance of the circuits and, in the present context, assess the detection of multipartite entanglement, one needs to delve into a lower-level description and derive a microscopic noise model that captures how the gates deviate in practice from the ideal unitaries (4)–(6). In Ref. [58], we evaluated the robustness of the previous entanglement witnesses for a phenomenological noise model that consisted of a depolarizing channel [1], together with bit-flip errors in the measurements. Each of these noise sources was controlled by a specific error rate, and the robustness of the witness was studied as one increases the severity of both noise sources. We note that, however, it is possible to go beyond this simplified model and derive more realistic microscopic error channels with rates that are fixed by specific experimental parameters. As noted in the introduction, this research direction has been developed to some extent for optical [42–45] and hyperfine [46–50] trapped-ion qubits operated with Mølmer-Sorensen entangling gates [22]. The goal of this section is to derive a microscopic noise model for trapped-ion Zeeman qubits operated with single-qubit rotations and entangling light-shift gates. As mentioned before, the bottleneck is the performance of entangling gates, and we thus focus on the error model for them.

A. Ideal entangling light-shift gates

To discuss sources of error, we first need to review the ideal scheme of a light-shift gate. We consider a crystal of N trapped $^{40}Ca^{+}$ ions, where the qubit is encoded in the two Zeeman sublevels of the $S_{1/2}$ ground-state [38], with $m_J = -1/2$ for $|\downarrow\rangle = |0\rangle$ and $m_J = 1/2$ for $|\uparrow\rangle = |1\rangle$, with $\omega_0/2\pi = 10.5\,\mathrm{MHz}$ as the transition frequency splitting between those states obtained by applying an external magnetic field [38]. The ions' equilibrium positions $\vec{r}_i^{\,0}$ are confined along the null of the rf-fields of a segmented linear Paul trap [38]. The light-shift gates [29] can be obtained from a pair of noncopropagating laser beams of frequency ω_L for $L \in \{1, 2\}$, which are far off-resonant from the dipole-allowed transitions $S_{1/2} \to P_{1/2}, P_{3/2}$ (see Fig. 4). The detuning of the laser beams from the dipole-allowed transition from $s \in \{|\uparrow\rangle, |\downarrow\rangle\}$, is assumed to be much larger than the qubit frequency splitting, $\omega_0 \ll \Delta_{l,\downarrow} \approx \Delta_{l,\uparrow} = \Delta$. It is also assumed in the last step that both detunings are approximately equal. Likewise, the detuning must be much larger than the linewidth of the dipole-allowed transition, $\Delta \gg \Gamma$, such that the residual spontaneous scattering is reduced. As we see below, the effect of such laser beams is a collection of ac-Stark shifts that arise due to second-order (two-photon) processes.

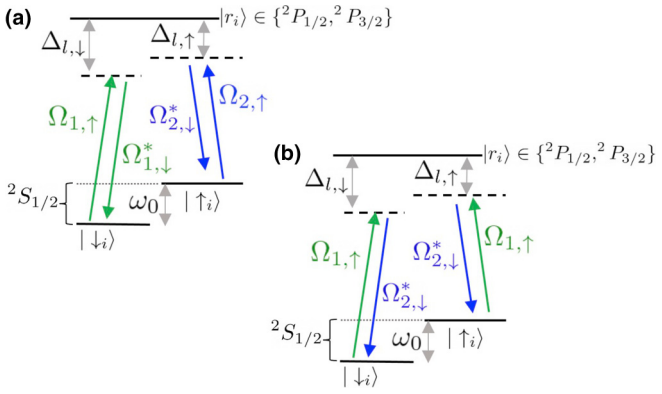

FIG. 4. Atomic levels and laser beam configurations used to create light-shift gates in $^{40}Ca^{+}$ ions with the qubit $s \in \{|\uparrow\rangle, |\downarrow\rangle\}$ encoded in the Zeeman sublevels of the $S_{1/2}$ ground state. $\Omega_{l,s}$ are the Rabi frequencies of the dipole-allowed transitions, with $l \in \{1, 2\}$ labeling a pair of noncopropagating laser beams. We consider that the detunings of these laser beams $\Delta_{l,s}$ are much bigger than the qubit frequency splitting $\omega_0 \ll \Delta_{l,\downarrow} \approx \Delta_{l,\uparrow} = \Delta$. The effect of this laser-beam configuration leads to second order (two-photon) process depicted in panel (a) where the ion virtually absorbs and emits a photon from and into the same laser, and panel (b) where the ion virtually absorbs from one laser and emits into the other one.

In addition to the internal electronic states, the ions also vibrate around the crystal equilibrium positions, giving rise to collective oscillations.

Following standard steps [78,100], let us define the beat-note frequency of the lasers $\Delta\omega_L = \omega_{L,1} - \omega_{L,2}$ and denote the three photon axes, the so-called radial $\alpha \in \{x, y\}$ and axial $\alpha = z$, with normal-mode frequencies $\omega_{\alpha,m}$ and creation and annihilation operators $a^\dagger_{\alpha,m}, a_{\alpha,m}$. With $N = 2$ trapped ions, we have $m = 2$ frequency modes for each α axis. In particular, the center of mass (COM) frequency mode, and the zigzag (ZZ) frequency mode. Ion crystals, in general, have micromotions, i.e., periodic motions due to oscillations of the Paul trap's potential. Excess micromotion are classically driven motions of the ions that off the rf null, and intrinsic micromotions which is a quantum-mechanical driven motion with the rf frequency [101]. Assuming the ions lie in the rf null and restricting to beat note frequencies far detuned from the rf frequencies, it is possible to neglect the excess and intrinsic micromotions and describe the ions' motional degrees of freedom as three decoupled branches. The internal and motional Hamiltonian of ions is then described by

$$H_0 = \frac{1}{2}\sum_{i=1}^{N}[\omega_0 + \delta\tilde{\omega}_{0,i}(t)]Z_i + \sum_{m=1}^{N}\sum_{\alpha=x,y,z}\omega_{\alpha,m}a^\dagger_{\alpha,m}a_{\alpha,m}, \tag{25}$$

wherein

$$\delta\tilde{\omega}_{0,i}(t) = \delta\omega_{0,i} + \delta\omega_{L,i} \tag{26}$$

reflects the contribution of the differential ac-Stark shifts. The first term in $\delta\tilde{\omega}_{0,i}$ represents an energy shift of the qubit frequency due to an ion virtually absorbing and emitting a photon from and into the same laser beam [see Fig. 4(a)]. The second term occurs when an ion virtually absorbs a photon from a

laser beam and then emits it into the other [see Fig. 4(b)], leading to crossed-beam oscillating ac-Stark shifts.

In more detail,

$$\delta\omega_{0,i} = \sum_l \left(\left|\Omega^i_{l,\uparrow}\right|^2 - \left|\Omega^i_{l,\downarrow}\right|^2\right)/4\Delta, \tag{27}$$

where $\Omega^i_{l,s}$ is the Rabi frequency of the corresponding dipole-allowed transition for the ith ion. Furthermore,

$$\delta\omega_{L,i} = |\tilde{\Omega}_{L,i}|\cos\left(\Delta\vec{k}\vec{r}_i^{\,0} - \Delta\Omega_L t + \phi_l\right). \tag{28}$$

In this expression, $\Delta\vec{k}_L = \vec{k}_{L,1} - \vec{k}_{L,2}$ is the differential wave-vector of the laser beams, and $\phi_L = \phi_{L,1} - \phi_{L,2}$ is the corresponding phase mismatch. The $\tilde{\Omega}_{L,i} = (\Omega_{1,\uparrow}\Omega^*_{2,\uparrow} - \Omega_{1,\downarrow}\Omega^*_{2,\downarrow})\exp\{-\frac{1}{2}\sum_m(\eta_{\alpha,m}M^\alpha_{i,m})^2\}/(4\Delta)$ contains contains the correction of the differential ac-Stark shifts by the Debye-Waller factors due to zero-point fluctuations of ion's vibrations [78], where $M^\alpha_{i,m}$ is the ith ion displacement in the mth mode along the α axis, and $\eta_{\alpha,m} = \Delta\vec{k}_L \cdot \mathbf{e}_\alpha/\sqrt{2m_{\mathrm{Ca}}\omega_{\alpha,m}} \ll 1$ is the Lamb-Dicke parameter [78] with m_{Ca} being the ion's mass.

The light-matter interaction Hamiltonian is given by

$$H_{\mathrm{int}} = \sum_{\alpha,i,m} \mathrm{i}\mathcal{F}^\alpha_{i,m} e^{\mathrm{i}(\Delta\vec{k}_L\cdot\vec{r}_i^{\,0} - \Delta\omega_L t + \phi_L)} Z_i(a_{\alpha,m} + a^\dagger_{\alpha,m}) + \mathrm{H.c.}, \tag{29}$$

where $\mathcal{F}^\alpha_{i,m}$ is a state-dependent dipole force,

$$\mathcal{F}^\alpha_{i,m} = \mathrm{i}\frac{|\tilde{\Omega}_{L,i}|}{2}\eta_{\alpha,m}M^\alpha_{i,m}. \tag{30}$$

The total light-matter Hamiltonian of the trapped ions interacting with the laser beams is then $H = H_0 + H_{\mathrm{int}}$ ($\hbar = 1$).

For the ideal performance of the gate, we assume that $\Delta\vec{k}_L$ is perfectly aligned with one of the radial vibrational branches, e.g., $\Delta\vec{k}_L \parallel \mathbf{e}_x$. Note that we have focused on the radial modes as they are more robust to successive shuttling and reconfiguration operations which, as discussed in the introduction, form a crucial part of the native trapped-ion toolbox in scalable shuttling-based approaches for quantum information processing (QIP) [33]. Now, moving to the interaction picture with respect to H_0, the resulting Hamiltonian is

$$H_{\mathrm{int}}(t) \simeq \sum_{i,m}^{N,M} \mathrm{i}\mathcal{F}^x_{i,m} Z_i a^\dagger_{x,m} e^{i\left(\Delta\vec{k}\vec{r}_i^{\,0} + \delta^x_m t + \phi_L\right)} + \mathrm{H.c.} \tag{31}$$

Here, we have defined the detunings $\delta^\alpha_m = \omega_{x,m} - \Delta\omega_L \ll \omega_{x,m}$, and used the underlying assumption $|\Omega_{L,i}| \ll \Delta\omega_L \simeq \omega_{x,m}$ which is used to neglect other powers of the vibrational operators in the Lamb-Dicke expansion of the laser-ion interaction. One thus sees that, when the laser beat note is tuned close to the target vibrational branch, it induces a state-dependent displacement that pushes the ions along different trajectories in phase space depending on the internal state. This results in a geometric phase gate capable of generating entanglement.

We can obtain the exact time evolution operator using the so-called Magnus expansion [102,103] which, under the assumption of perfectly aligned laser and the neglect of high-order vibrational operators, closes at second order. This results in

$$U(t) = e^{-\mathrm{i}H_0 t} e^{\sum_{i,m}(\Phi^x_{i,m}(t)a^\dagger_{x,m} - \mathrm{H.c.})Z_i} \times e^{-\mathrm{i}\sum_{i,j}Z_iZ_j(\frac{J_{ijt}}{2} - 2\sum_m \mathrm{Re}\{\Phi^\alpha_{i,m}(t)(\Phi^\alpha_{i,m}(0))^*\})}, \tag{32}$$

where we have defined

$$\Phi^x_{i,m}(t) = \frac{\mathcal{F}^x_{i,m}}{\delta^x_m} e^{\mathrm{i}(\Delta\vec{k}_L\cdot\vec{r}_i^{\,0} + \phi_L)}(1 - e^{\mathrm{i}\delta^x_m t}). \tag{33}$$

We thus see that the time-evolution operator contains state-dependent displacement operators, i.e., $\mathcal{D}_\pm(\Phi^x_{i,m}(t)) = \exp(\pm\Phi^x_{i,m}(t)a^\dagger_{x,m} \mp \Phi^x_{i,m}(t)^* a_{x,m})$ for $|\uparrow\rangle, |\downarrow\rangle$, which can lead to residual qubit-phonon entanglement if the trajectories are not closed, i.e., if $\Phi^x_{i,m}(t) \neq 0$. The evolution operator also contains a qubit-qubit coupling term of strength

$$J_{ij} = -2\sum_m \frac{\mathcal{F}^x_{i,m}\mathcal{F}^x_{j,m}}{\delta^x_m}\cos\left(\phi^0_{ij}\right), \tag{34}$$

that generates entanglement through phonon-mediated interactions [104–107]. The phase $\phi^0_{ij} = \Delta\vec{k}_L \cdot (\vec{r}_i^{\,0} - \vec{r}_j^{\,0})$ causes the coupling strength J_{ij} to oscillate with the distance between ions in a generic situation. However, for radial phonons, this oscillation disappears. We note that off-resonant terms additional to the force in Eq. (31) can also be accounted for in the Magnus expansion, which lead to small perturbations to the spin-spin couplings [106].

An ideal implementation of the two-qubit light-shift gate exploits these phonon-mediated interactions to generate entanglement and minimizes the residual qubit-phonon entanglement with the active phonons mediating the entangling operations. By active mode we refer to the mode m along an α-axis direction used to perform the entangling gate, the remaining $3N - 1$ modes are refereed to as the spectator modes, which in an ideal scenario are not involved in the entangling operation. Using a single pulse per ion qubit, this can be achieved as follows. For radial modes, there is no large separation between the center-of-mass mode (COM, $m = 1$) and the remaining zigzag (ZZ, $m = 2$) mode. As a consequence, we cannot divide the radial modes that the state-dependant force excites into active and spectator modes, as occurs for forces coupling to the axial modes [22], and both modes mediate the interaction. This means that we excite two trajectories in the phase spaces of each mode with large excursions that both must be closed at the final gate time duration t_g, in order to minimize the residual qubit-phonon entanglement and achieve a high gate fidelity. This leads to the following two conditions:

$$\begin{aligned}\Phi^x_{i,\mathrm{com}}(t_g) = 0 &\Rightarrow \frac{\mathcal{F}^x_{i,\mathrm{com}}}{\delta^x_{\mathrm{com}}}(1 - e^{\mathrm{i}\delta^x_{\mathrm{com}}t_g}) = 0,\\ \Phi^x_{i,\mathrm{zz}}(t_g) = 0 &\Rightarrow \frac{\mathcal{F}^x_{i,\mathrm{zz}}}{\delta^x_{\mathrm{zz}}}(1 - e^{\mathrm{i}\delta^x_{\mathrm{zz}}t_g}) = 0.\end{aligned} \tag{35}$$

The only possibility to satisfy both conditions with a single pulse is to have two detunings are multiples of each other, $\delta^x_{\mathrm{zz}} = p\delta^x_{\mathrm{com}}$, such that

$$\delta^x_{\mathrm{com}}t_g = 2\pi r, \quad \delta^x_{\mathrm{zz}}t_g = 2\pi rp, \quad r, p \in \mathbb{Z}. \tag{36}$$

Here, r is the number of closed loops in the phase space of the COM mode, and $|pr|$ is the number of loops in the ZZ mode. One possibility is to fix $r = 1$, $p = -1$, such that, $\delta^x \equiv \delta^x_{\rm zz} = -\delta^x_{\rm com}$, and the state-dependent force lies midway from both resonances $\Delta\omega_L \simeq (\omega_{x,\rm com} + \omega_{x,\rm zz})/2$. In this case, the trajectories correspond to two circles winding in opposite directions with $t_g = 2\pi/\delta^x$. Using the normal-mode displacements $M^x_{1,\rm com} = M^x_{2,\rm com} = 1/\sqrt{2}$ and $M^x_{1,\rm zz} = -M^x_{2,\rm zz} = 1/\sqrt{2}$, the phonon-mediated interactions have a strength

$$J_{12,x} = -\frac{1}{2\delta^x}\left(\frac{\omega_L \eta_{x,\rm com}}{\sqrt{2}}\right)^2 e^{-\frac{1}{2}(\eta^2_{x,\rm com}+\eta^2_{x,\rm zz})}\left(1+\frac{\omega_{x,\rm com}}{\omega_{x,\rm zz}}\right). \tag{37}$$

In the interaction picture, the ideal unitary evolution operator for $N = 2$ ions becomes

$$U_{\rm id}(t_g) = e^{-{\rm i}(J_x t_g)\sigma^z_1\sigma^z_2}, \tag{38}$$

where $J_{12,x} = J_{21,x} = J_x$. The unitary at multiples of this gate time describes decoupled dynamics of the gate-mediated phonons and qubits and yields a maximally entangling gate for $J_x t_g = \pi/4$, $U_{\rm id} = U_{\rm id}(\pi/4J_x)$, that generates an entangled pair from an initial separable state $|\Psi_0\rangle = |{+}{+}\rangle$. In the interaction picture, this reads

$$|\psi_{\rm id}\rangle = U_{\rm id}|\psi(0)\rangle = \frac{1}{\sqrt{2}}(|{-}{-}\rangle - {\rm i}|{+}{+}\rangle). \tag{39}$$

In contrast with the use of axial modes, where δ is pretty much free [22], here we have to place it between the COM and ZZ modes to close both trajectories simultaneously.

In the following section, we study the effect of noise and experimental imperfections on this maximally entangling gate. As noted in the introduction, previous results [52,53] follow similar calculations of state infidelities in the Mølmer-Sørensen gate [22] and identify different contributions to deviations from the target state (39). These deviations can be quantified through the state fidelity $\mathcal{F}_s = \langle\Psi_{\rm id}(t_g)|\mathcal{E}(\rho_0)|\Psi_{\rm id}(t_g)\rangle$, where $\mathcal{E}(\rho_0)$ describes the noisy evolution of the initial state, which is typically considered to be in a product state of the internal and vibrational degrees of freedom $\rho_0 = |{+}{+}\rangle\langle{+}{+}| \otimes \rho_{\rm vib}$. In general, however, the gate embedded in a larger circuit will act on other states and, in order to provide a more representative of the gate performance, one should instead compute the gate error $\epsilon_g = 1 - \bar{\mathcal{F}}_g$, which is obtained by averaging the corresponding fidelities for all possible initial states $\rho_0 = |\Psi_0\rangle\langle\Psi_0| \otimes \rho_{\rm vib}$. Below we give explicit expressions for these errors, investigating the influence of thermal fluctuations in all vibrational branches $\epsilon^{\rm th}_g$, off-resonant couplings $\epsilon^{\rm off}_g$, dephasing noise due to fluctuating unshielded magnetic fields of laser phase noise $\epsilon^{\rm d}_g$, and residual spontaneous photon scattering $\epsilon^{\rm sp}_g$. For small or weak errors, the effect of distinct sources of noise is additive [1]. Therefore,

$$\epsilon^{\rm tot}_g = \epsilon^{\rm th}_g + \epsilon^{\rm off}_g + \epsilon^{\rm deph}_g + \epsilon^{\rm scatt}_g. \tag{40}$$

B. Average gate fidelity

The light-shift gate fidelity can be calculated by averaging the state fidelities of the real time-evolved states for all possible initial states of the two qubits [1], with respect to the ideal target state for each of them, namely, $U_{\rm id}|\Psi_0\rangle$. Accordingly, the gate fidelity is

$$\bar{\mathcal{F}}_g(U_{\rm id},\mathcal{E}) = \int {\rm d}\Psi_0 \langle\Psi_0|U^\dagger_{\rm id}\mathcal{E}(\rho_0)U_{\rm id}|\Psi_0\rangle, \tag{41}$$

where the integral is taken with respect to the Haar measure over the two-qubit Hilbert space, and thus averages over all possible two-qubit states $|\Psi_0\rangle$. Here, $\mathcal{E}(\rho_0)$ describes the real evolution of the initial state ρ_0 under a noisy quantum channel. To account for sources of errors added to the thermal fluctuations of the vibrational modes, we consider $\mathcal{E}(\rho_0) = \langle{\rm Tr}_{\rm aux}\{U_{g(t)}|\Psi_0\rangle\langle\Psi_0| \otimes \rho_{\rm aux}U^\dagger_{g(t)}\}\rangle_{\rm stoch}$, where $\rho_{\rm aux}$ describes "auxiliary" degrees of freedom, including all the phonon branches, other electronic states such as the virtually populated P levels used to induce the state-dependent dipole forces, as well as the photons of the surrounding electromagnetic environment. Additionally, the unitary evolution of the complete system $U_{g(t)}$ may depend on external fluctuations, such as un-shielded magnetic fields or fluctuating control parameters, which can be modeled by stochastic processes $\{g(t)\}$. Accordingly, the quantum channel will also result from statistical averaging over such stochastic processes, which corresponds to $\langle\cdot\rangle_{\rm stoch}$ in the previous expression. As a result of this average and the partial trace, the evolution of the system will no longer be unitary as in the ideal case (38). The goal of this section is to find contributions to the gate infidelity in the limit of small errors, which can be calculated analytically, and then fed into effective noise models.

To avoid the integral over the two-qubit Hilbert space, we can alternatively calculate the entanglement fidelity [108–110] given by

$$\bar{\mathcal{F}}_e(U_{\rm id},\mathcal{E}) = \langle\phi_m|I^d \otimes U^\dagger_{\rm id}\,\mathcal{E}(\rho_m)\,I^d \otimes U_{\rm id}|\phi_m\rangle. \tag{42}$$

The entanglement fidelity is defined in an enlarged Hilbert space with partitions A and B, where A is auxiliary with the same number of qubits as B and $|\phi_m\rangle = \sum_{\xi=1}^d |\xi\rangle_A \otimes |\xi\rangle_B/\sqrt{d}$ is a maximally entangled state. Here, $d = 2^N$, where N is the number of physical qubits involved in the gate, and the set $\{|\xi\rangle\}$ of d quantum states is chosen to form an orthonormal basis. For the current case of $N = 2$, we have $d = 4$ basis states $\{|{+}{+}\rangle, |{+}{-}\rangle, |{-}{+}\rangle, |{-}{-}\rangle\}$. In the above equation (42), the auxiliary qubits are not subjected to the ideal or noisy time evolution, such that $\mathcal{E}(\rho_m) = \langle{\rm Tr}_{\rm aux}\{I^d \otimes U_{g(t)}\,|\Phi_m\rangle\langle\Phi_m| \otimes \rho_{\rm aux}\,I^d \otimes U^\dagger_{g(t)}\}\rangle_{\rm stoch}$. By doubling the number of qubits, and exploiting their entanglement, one can prove [108,110] that a single state fidelity of the enlarged system can be used to infer the gate fidelity of the original physical system via

$$\bar{\mathcal{F}}_{\rm g}(U_{\rm id},\mathcal{E}) = \frac{d\bar{\mathcal{F}}_e(U_{\rm id},\mathcal{E})+1}{d+1}. \tag{43}$$

Equipped with this formal tool, it is possible to derive analytical expressions for various sources of gate infidelities. As advanced previously, we are interested in a perturbative

regime where different error sources are additive and thus can be thus discussed sequentially.

C. Gate infidelity due to thermal errors

The light-shift gates, just like Mølmer-Sørensen gates [21,22], are robust against the thermal occupation of the active phonon modes in the Lamb-Dicke approximation. In this section, we analyze the effect of thermal occupation due to higher-order terms in the Lamb-Dicke expansion for both the active vibrational modes as well as the spectator modes.

1. Warm active phonons

There are higher-order terms in the Lamb-Dicke expansion of Eq. (29), there are additional corrections that stem from higher-order terms in the Lamb-Dicke parameters which are not far-off resonant and thus must be taken into account. Under these circumstances, ensuring that the beat note laser frequencies are still satisfying $|\tilde{\Omega}_{L,i}| \ll \Delta\omega_L \simeq \omega_{x,m}$, the force parameter from Eq. (30) transforms into

$$\widetilde{\mathcal{F}^x_{i,m}} = \mathrm{i}\frac{|\tilde{\Omega}_{L,i}|}{2}\eta_{x,m}M^x_{i,m}\mathcal{G}^x_{i,m}(\{a^\dagger_{x,m}a_{x,m}\}), \tag{44}$$

where we have introduced the operator

$$\mathcal{G}^x_{i,m} = \left(\sum_{l=0}^{\infty}\frac{\left[-\left(\eta_{x,m}M^x_{i,m}\right)^2\right]^l}{(l!)^2(l+1)}(a^\dagger_{x,m}a_{x,m})^l\right) \times \prod_{m'\neq m}\left(\sum_{l=0}^{\infty}\frac{\left[-\left(\eta_{x,m'}M^x_{i,m'}\right)^2\right]^l}{(l!)^2}(a^\dagger_{x,m'}a_{x,m'})^l\right). \tag{45}$$

Depending on the motional state, this operator will result in fluctuations in the amplitude of the force.

As highlighted before, one important difference between axial and radial-mediated entangling gates is that in the former case, there is only one active vibrational mode. Typically, it is chosen to be the COM mode, whereas the other breathing mode is off-resonant, and merely acts as a spectator. In our case, since we are focusing on radial modes along the $\alpha = x$ axis, both COM and ZZ modes are active, and they contribute to the gate equally. We consider the initial vibrational state described by the tensor product of two thermal Gibbs states $\rho^{\mathrm{th}}_{\mathrm{vib},x} = \rho^{\mathrm{th}}_{\mathrm{com}} \otimes \rho^{\mathrm{th}}_{\mathrm{zz}}$ of the form

$$\rho^{\mathrm{th}}_m = \sum_{n_m=0}^{\infty} p_m(n_m)|n_m\rangle\langle n_m|, \tag{46}$$

where the probability $p_{\mathrm{m}}(n_{\mathrm{m}})$ is given by a thermal distribution

$$p_{\mathrm{m}}(n_{\mathrm{m}}) = \frac{1}{1+\bar{n}_m}\left(\frac{\bar{n}_m}{1+\bar{n}_m}\right)^{n_m}. \tag{47}$$

Here, $\bar{n}_m = 1/(e^{k_{\mathrm{B}}T_m/\hbar\omega_m} - 1)$ is the Bose-Einstein distribution, ω_m is the frequency of the m mode, and T_m is the effective temperature for each mode used to model situations in which resolved sideband cooling is used.

By considering the new force operator (44), one can revisit the Magnus expansion that leads to the evolution in Eq. (32). We find that, the closure conditions $\Phi^x_{i,\mathrm{com}}(t_g) = \Phi^x_{i,zz}(t_g) = 0$, are not modified by thermal fluctuations. On the other hand, the spin-spin interactions (34) depend on the number of phonons. To the lowest order of the Lamb-Dicke parameters, they read

$$J_{ij,x} = -2\sum_m \frac{\mathcal{F}^x_{i,m}\mathcal{F}^x_{j,m}}{\delta_m}\left(1 - \sum_{m'}\eta^2_{x,m'}a^\dagger_{x,m'}a_{x,m'}\right). \tag{48}$$

Therefore, the $J_x t_g = \pi/4$ condition, which leads to the ideal maximally entangling gate (38) for phonons in the vacuum state, now leads to qubit-qubit interactions that depend on the thermal fluctuations of phonons, affecting the gate fidelity. Using the entanglement fidelity (43) with the auxiliary qubits in the specific entangled state, it is possible to evaluate the gate fidelity for the initial thermal states analytically, arriving at an error due to warm active phonons,

$$\epsilon^{\mathrm{act}}_{\mathrm{th}} = \frac{\pi^2}{20}\sum_{m,m'}\eta^2_{x,m}\eta^2_{x,m'}\langle\hat{n}_{x,m}\hat{n}_{x,m'}\rangle, \tag{49}$$

where $\langle\hat{n}_{x,m}\hat{n}_{x,m'}\rangle = (2\bar{n}^2_m + \bar{n}_m)\delta_{m,m'} + \bar{n}_m\bar{n}_{m'}(1-\delta_{m,m'})$ for the above thermal states. We note that the condition $J_x t_g = \pi/4$ for the entangling gate could be modified to account for the mean number of phonons, and the above gate errors would only depend on the thermal fluctuations because of the variances on the phonon number. However, since we are interested in modeling shuttling-based QIP, the phonon state will change between different gates, and such optimal conditions will not hold for the whole circuit. Accordingly, we follow a conservative approach by considering that the errors (49) follow from setting the vacuum condition $J_x t_g = \pi/4$ throughout the circuit. In Table I, we give the specific error (49) for $N = 2$ ions.

2. Warm spectator phonons

So far, we have assumed that the spectator modes (i.e., those along the remaining radial $\alpha = x$ direction, along the radial $\alpha = y$ axis, and those along the $\alpha = z$ axial direction) do not affect the gate performance. This is strictly so if the alignment of the beams is perfect $\Delta\vec{k}_L = \Delta k_L \mathbf{e}_x$. However, if there is a small misalignment, such that the corresponding Lamb-Dicke parameters no longer vanish $\eta_{z,m}, \eta_{y,m} \neq 0$, the spectator modes could contribute to fluctuations of the effective Rabi frequency of the state-dependant dipole force, off-resonant drivings, and unclosed trajectories in phase space. Following a similar calculation as above, the force parameter, when considering the spectator phonons transforms into

$$\widetilde{\widetilde{\mathcal{F}^x_{i,m}}} = \mathrm{i}\frac{|\widetilde{\tilde{\Omega}_{L,i}}|}{2}\eta_{x,m}M^x_{i,m}\mathcal{G}^x_{i,m}(\{a^\dagger a\})\mathcal{K}^{y,z}_i(\{a^\dagger a\}), \tag{50}$$

where, in this case, the Debye-Waller factor must also account for the vacuum contributions of the additional vibrational modes,

$$\widetilde{\tilde{\Omega}_{L,i}} = \Omega_{L,i}e^{-\frac{1}{2}\left(\sum_m(\eta_{x,m}M^x_{i,m})^2 + \sum_{\alpha=y,z}\sum_m(\eta_{\alpha,m}M^\alpha_{i,m})^2\right)}. \tag{51}$$

TABLE I. Summary of the different error source contributions to the gate infidelity. For low values of $\bar{n}_{\alpha,m}$, the leading error contribution is due to off-resonant forces. However, for increasing $\bar{n}_{\alpha,m}$, the thermal error contribution becomes more predominant. For $\bar{n}_{\alpha,m} \approx 10$ becomes the leading error source. The contribution to the infidelity due to dephasing and residual photon scattering is much lower than the other two sources, with the one due to dephasing one order of magnitude higher.

Thermal errors	Warm active phonons (49)	$\epsilon_{\rm th}^{\rm act} = \frac{\pi^2}{20}\sum_{m,m'}\eta_{x,m}^2\eta_{x,m'}^2\langle\hat{n}_{x,m}\hat{n}_{x,m'}\rangle$ (A 1)
	Warm spectator phonons (54)	$\epsilon_{\rm th}^{\rm spec} = \frac{\pi^2}{20}\sum_{m,m'}\sum_{\alpha,\alpha'}C_{\alpha,\alpha'}\eta_{\alpha,m}^2\eta_{\alpha',m'}^2\langle\hat{n}_{\alpha,m}\hat{n}_{\alpha',m'}\rangle$ (A 2)
Off-resonant coupling	Active phonons (57)	$\epsilon_{\rm off}^{\rm act} = \sum_{i,m}\frac{\tilde{\Omega}_{L,i}^2}{5}\eta_{x,m}^2\frac{2\pi}{(\omega_{x,m}^2-\Delta\Omega_L^2)}$
	Spectator phonons (59)	$\epsilon_{\rm off}^{\rm spec} = \frac{4}{5}\sum_{\alpha=y,z}\sum_m \frac{(\tilde{\Omega}_L\eta_{\alpha,m}^2)^2}{\Delta\omega_L^2-\omega_{\alpha,m}^2}\left\lvert\frac{\Delta\omega_L^2+\omega_{\alpha,m}^2}{\Delta\omega_L^2-\omega_{\alpha,m}^2}(2\bar{n}_{\alpha,m}+1)+{\rm i}\frac{2\pi\omega_{\alpha,m}}{\omega_{\alpha,m}-\Delta\omega_L}\right\rvert$
Dephasing noise	Local B-field (63)	$\epsilon_g^{\rm deph,l} \approx \frac{8}{5}(t_g/2T_2)$
	Correlated B-field (66)	$\epsilon_g^{\rm deph,c} \approx \frac{8}{5}(t_g/2T_2)$
Residual photon scattering	Rayleigh (72)	$\epsilon_{\rm Rai}^{\rm scatt} = \frac{8}{5}(t_g/2T_2^{\rm eff})$
	Raman (75)	$\epsilon_{\rm Ram}^{\rm scatt} = \frac{12}{5}(t_g/T_1)$

In addition, the force can fluctuate depending on the moments of the number of spectator phonons,

$$\mathcal{K}_i^{y,z} = \prod_{\alpha=y,z}\prod_m\left(\sum_{l=0}^{\infty}\frac{\left[-\left(\eta_{\alpha,m}M_{i,m}^{\alpha}\right)^2\right]^l}{(l!)^2}(a_{\alpha,m}^{\dagger}a_{\alpha,m})^l\right). \quad (52)$$

In a shuttling-based approach to QIP, since the axial modes (along the trap axis) are more susceptible to heating by the crystal reconfigurations, the modes in $\alpha = z$ will have higher contributions to this source of error. To calculate it explicitly, we check how it affects the Magnus expansion and the spin-spin interactions. The closure conditions of the phase-space trajectories are the same in spite of the additional spectator modes; that is, $\Phi_{i,\rm com}^x(t_g) = \Phi_{i,\rm zz}^x(t_g) = 0$. However, as in the case of warm active phonons, the spin-spin strength will depend on the phonon operators as

$$J_{ij,x} = -2\sum_m\frac{\mathcal{F}_{i,m}^x\mathcal{F}_{j,m}^x}{\delta_m}\left(1-\sum_{m'}\eta_{x,m'}^2a_{x,m'}^{\dagger}a_{x,m'} - \frac{1}{2}\sum_{\alpha=y,z}\sum_{m'}\eta_{x,m'}^2a_{\alpha,m'}^{\dagger}a_{\alpha,m'}\right). \quad (53)$$

The calculation of the gate fidelity goes along the same lines as before and leads to the following error due to spectator modes:

$$\epsilon_{\rm th}^{\rm spec} = \frac{\pi^2}{20}\sum_{m,m'}\sum_{\alpha,\alpha'}C_{\alpha,\alpha'}\eta_{\alpha,m}^2\eta_{\alpha',m'}^2\langle\hat{n}_{\alpha,m}\hat{n}_{\alpha',m'}\rangle, \quad (54)$$

where we have introduced the symmetric matrix with coefficients $C_{x,y} = C_{x,z} = 1/2$ and $C_{y,z} = C_{x,z} = 1/4$, otherwise zero. The total gate error due to thermal noise in Eq. (40) is then $\epsilon_g^{\rm th} = \epsilon_{\rm th}^{\rm ac} + \epsilon_{\rm th}^{\rm spec}$. In Table I, we give the specific error for $N = 2$ ions.

D. Gate infidelity due to off-resonant forces

When moving to the interaction picture in Eq. (31), we neglected off-resonant contributions to the state-dependent forces of both active and spectator modes. In this section, we calculate the contribution of those errors to gate infidelity.

1. Off-resonant forces on active phonons

In Eq. (31), we kept just the contributions of $e^{i(\Delta\vec{k}_L\cdot\vec{r}_i^{\,0}+\delta_m^x t+\phi_L)}$ to the dipole force, where $\delta_m^x = \omega_{x,m} - \Delta\omega_L$. With the beat-note laser frequency set close to the vibrational modes $\Delta\omega_L \approx \omega_{x,m}$ so that the neglected terms rotate with $\omega_{\alpha,m} + \Delta\omega_L$, and are thus off-resonant contributing perturbatively to the gate. To account for the error, we treat this perturbation

$$V_I = \sum_{i,m}{\rm i}\mathcal{F}_{i,m}^x e^{{\rm i}(\Delta\vec{k}_L\cdot\vec{r}_i^{\,0}+(\omega_{x,m}+\Delta\omega_L)t+\phi_L)}Z_ia_{x,m} + {\rm H.c.} \quad (55)$$

in the interaction picture with respect to the ideal unitary evolution (32), such that

$$\tilde{U}(t_g) = e^{-{\rm i}H_0t_g}U(t_g)\mathcal{T}\{e^{-{\rm i}\int_0^{t_g}dt'V_I(t')}\}. \quad (56)$$

We evaluate the leading contribution to the error using the Dyson series expansion of the time-ordered operator. The leading error contribution is calculated by assuming the symmetric closure conditions for the ideal gate $t_g = 2\pi/\delta^x$, with $\delta_{\rm com}^x = -\delta_{\rm zz}^x = \delta^x$. By substituting the Dyson expansion in the expression for entanglement fidelity (42), we get the following contribution to the gate infidelity for $N = 2$ ions:

$$\epsilon_{\rm off}^{\rm act} = \sum_{i,m}\frac{\tilde{\Omega}_{L,i}^2}{5}\eta_{x,m}^2\frac{2\pi}{\left(\omega_{x,m}^2-\Delta\Omega_L^2\right)}, \quad (57)$$

as shown in Table I. Let us note that, from the Dyson expansion, one finds two processes with opposite detunings contributing to the error, such that the dependence on the mean phonon numbers cancels. In that regard, the contribution to the off-resonant error (57) could indeed be accounted for by a small renormalization of the phonon-mediated interaction strength, leading to an under-rotation. As such, one could modify the required laser intensity needed to meet the constraint for a maximally entangling gate $J_xt_g = \pi/4$, by using the qubit-qubit interactions that also take into account these off-resonant contributions [111]. The situation is different for spectator modes.

2. Off-resonant forces on spectator phonons

The spectator modes will also be subject to off-resonant forces when the laser wave vector is misaligned. We now include the spectator modes for $\alpha = y, z$ in Eq. (31), and consider the following perturbation due to off-resonant terms,

$$V_I \simeq \sum_{\alpha=y,z}\sum_{i,m} \mathrm{i}\mathcal{F}^{\alpha}_{i,m}\big[e^{\mathrm{i}\left(\Delta\vec{k}_L\cdot\vec{r}^{\,0}_i+\delta^{\alpha}_m t+\phi_L\right)} + e^{-\mathrm{i}\left(\Delta\vec{k}_L\cdot\vec{r}^{\,0}_i+(\omega_{\alpha,m}+\Delta\omega_L)t+\phi_L\right)}\big]Z_i a^{\dagger}_{\alpha,m} + \mathrm{H.c.} \tag{58}$$

Proceeding similarly as in Eq. (56), we estimate the leading error to the gate fidelity which, in contrast with the active modes, depends on the mean number of phonons. In this case, the contribution to the gate error is given by

$$\epsilon^{\mathrm{spec}}_{\mathrm{off}} = \frac{4}{5}\sum_{\alpha=y,z}\sum_{m}\frac{\left(\tilde{\Omega}_L\eta^2_{\alpha,m}\right)^2}{\Delta\omega^2-\omega^2_{\alpha,m}} \times\left|\frac{\Delta\omega_L^2+\omega^2_{\alpha,m}}{\Delta\omega_L^2-\omega^2_{\alpha,m}}(2\bar{n}_{\alpha,m}+1)+\mathrm{i}\frac{2\pi\omega_{\alpha,m}}{\omega_{\alpha,m}-\Delta\omega_L}\right|. \tag{59}$$

Note that, the second contribution in the equation above is indeed caused by an under/over-rotation that could be accounted for by summing also over the spectator modes in the definition of the qubit-qubit couplings (34) and by modifying the condition for a maximally entangling gate. The thermal contribution, on the other hand, cannot be minimized and contributes to the $N = 2$ error of Table I. Altogether, the gate error from off-resonant forces is $\epsilon^{\mathrm{off}}_g = \epsilon^{\mathrm{spec}}_{\mathrm{act}} + \epsilon^{\mathrm{spec}}_{\mathrm{off}}$.

E. Gate infidelity due to dephasing noise

As noted in the introduction to the light-shift gate III A, there could also be possible errors due to magnetic field and laser-phase fluctuations on the Zeeman sublevels forming our qubit. We can study these fluctuations in two regimes; when the magnetic-field fluctuations act locally on the ions and they are fully uncorrelated, and when they act globally and affect both qubits in a correlated manner. In both cases, we assume that the stochastic process describing this noise is Markovian, and model its effect by a standard dephasing master equation in the Lindblad form [1], namely,

$$\dot{\rho}(t) = -\mathrm{i}[H_0 + H_{\mathrm{int}}, \rho(t)] + \mathcal{D}_d(\rho(t)). \tag{60}$$

The form of the coherent evolution with H_0 and H_{int} is that of the Hamiltonians in Eqs. (25) and (29), respectively. The superoperator $\mathcal{D}_d(\rho(t))$ stems from averaging the stochastic noise describing local and global magnetic-field fluctuations in the weak-coupling limit.

1. Individual dephasing noise

In this scenario, the fluctuations are local, and there are no spatial correlations in the noise. We also assume that the noise is Markovian and the Lindblad operators for the dephasing are $L_i = \sqrt{\Gamma_d/2}Z_i$, where $\Gamma_d = 1/T_2$ is the dephasing rate, and T_2 the dephasing time of the qubits. Since all terms in the Hamiltonian and noise commute, it is straightforward to move to the interaction picture in Eq. (60) to find that the ideal evolution of the form

$$\dot{\rho}_I(t) = \frac{\Gamma_d}{2}\sum_i [Z_i\rho_I(t)Z_i - \rho_I(t)], \tag{61}$$

where $\rho_I(t) = U^{\dagger}(t)\rho(t)U(t)$ is the evolution of the system in an interaction picture with respect to the coherent terms $U(t) = \mathcal{T}(\exp\{-\mathrm{i}\int_0^t \mathrm{d}t'[H_0 + H_{\mathrm{int}}(t')]\})$. The solution to this equation is simply the composition of two dephasing channels which read

$$\rho_I(t_g) = [1-p_d(t_g)]^2\rho(0) + p_d^2(t_g)Z_1Z_2\rho(0)Z_1Z_2 + [1-p_d(t_g)]p_d(t_g)\sum_i Z_i\rho(0)Z_i, \tag{62}$$

where $p_d(t_g) = \frac{1}{2}(1-e^{-t_g/T_2})$ is the phase-flip error rate. We should bear in mind that, when moving back to the original picture, $\rho(t_g) = U(t_g)\rho_I(t)U^{\dagger}(t_g)$, one gets the additional evolution under coherent terms (32), which would lead to the light-shift gate (38) under idealized conditions. Substituting this expression into the entanglement fidelity formula in Eq. (42), and neglecting the combination of thermal and dephasing errors, as these will only appear in higher-order perturbations, we find that the leading error to the gate infidelity is given by

$$\epsilon^{\mathrm{deph,1}}_g = \tfrac{4}{5}\big[2p_d(t_g) - p_d^2(t_g)\big]. \tag{63}$$

If one assumes a weak dephasing during the extent of the gate $t_g \ll T_2$, with $t_g = 2\pi/\delta^x$, the dephasing gate error can be approximated by $\epsilon^{\mathrm{deph,1}}_g \approx \frac{4N}{5}(t_g/2T_2)$. In this case, the gate infidelity scales linearly with N. In this paper, we restrict to $N = 2$ as summarized in Table I.

2. Correlated dephasing noise

Let us now discuss the limit where the magnetic -field fluctuations or the laser phase noise are global and affect both qubits in a correlated manner. In this case, moving to the interaction picture in Eq. (60), the master equation becomes

$$\dot{\rho}_I(t) = 2\Gamma_d\big(S_z\rho_I(t)S_z - \tfrac{1}{2}S_z^2\rho_I(t) - \tfrac{1}{2}\rho_I(t)S_z^2\big), \tag{64}$$

with $S^z = (Z_1 + Z_2)/2$ being the total spin operator. The solution to this master equation can be written in terms of $\chi(t) \equiv e^{-Nt/T_2}$, which decays twice as fast as the case of individual dephasing. The quantum channel admits an analytical solution in Kraus form $\rho_I(t_g) = \sum_n K_n^{\dagger}(t_g)\rho(0)K_n(t_g)$,

$$\begin{aligned}
K_1(t_g) &= \tfrac{1}{2}\big(\sqrt{\chi(t_g)}+1\big)I + \tfrac{1}{2}\big(\sqrt{\chi(t_g)}-1\big)Z_1Z_2,\\
K_2(t_g) &= \tfrac{1}{2}\sqrt{\chi(t_g)[1-\chi(t_g)]}(Z_1+Z_2),\\
K_3(t_g) &= \tfrac{1}{4}[1-\chi(t_g)](1+Z_1+Z_2+Z_1Z_2),\\
K_4(t_g) &= \tfrac{1}{4}[1-\chi(t_g)](1-Z_1-Z_2+Z_1Z_2).
\end{aligned} \tag{65}$$

It is worth mentioning that if one is interested in the state fidelity for the maximally entangled pair obtained by Mølmer-Sørensen gates [42], it scales as N^2 due to the global nature of the noise. In the present case, however, we are interested in light-shift gates and, moreover, not the fidelity of producing a single state but rather the average gate fidelity. Substituting the previous Kraus channel n the expression of the entanglement

fidelity (42) to estimate the contribution to the gate infidelity, we find that

$$\epsilon_g^{\text{deph,c}} \simeq \tfrac{4}{5}\big[2p_d(t_g) - 3p_d^2(t_g) + 4p_d^3(t_g) - 2p_d^4(t_g)\big]. \quad (66)$$

Although this expression differs from the uncorrelated one in Eq. (63), for weak dephasing during the gate time, one finds that $\epsilon_g^{\text{deph,c}} \approx \epsilon_g^{\text{deph,c}}$.

F. Gate infidelity due to residual photon scattering

So far, when using the expression of the state-dependent force (31), we have neglected the possible irreversible dynamics due to the emission of photons from the excited P levels to the background of electromagnetic modes (see Fig. 4). This is justified for very large detunings of the lasers, but, in general, it will have some contribution to the error. To determine this contribution, we consider the Markovian master equation

$$\dot{\rho}(t) = -\mathrm{i}[H_0 + H_{\text{int}}, \rho(t)] + \mathcal{D}_{sc}(\rho(t)) \quad (67)$$

which is obtained after tracing over the excited $P_{1/2}, P_{3/2}$ levels of linewidth $1/\Gamma$ and the electromagnetic photons [1]. In addition to the coherent terms in Eq. (67), we get a Lindblad-type term $\mathcal{D}_{sc}(\rho(t))$ describing the effect of the residual spontaneous emission within the qubit computational subspace due to off-resonant scattering of photons. Following Refs. [112,113], we get

$$\mathcal{D}_{sc}(\rho) = \sum_i \sum_n \left(L_{i,n}\rho L_{i,n}^\dagger - \frac{1}{2}\{L_{i,n}^\dagger L_{i,n}, \rho\}\right). \quad (68)$$

where one finds two possible decoherence effects, the so-called Raman and Rayleigh scattering of photons [114,115]. These are described by the following effective jump operators

$$L_{i,1} = \frac{\sqrt{\Gamma}}{\Delta}\sum_{l=1,2}\Omega_{l,\downarrow}^i e^{\mathrm{i}(\vec{k}_{L,l}\cdot\vec{r}_i - \omega_{L,l}t)}(|\downarrow_i\rangle\langle\downarrow_i| + |\downarrow_i\rangle\langle\uparrow_i|),$$

$$L_{i,2} = \frac{\sqrt{\Gamma}}{\Delta}\sum_{l=1,2}\Omega_{l,\uparrow}^i e^{\mathrm{i}(\vec{k}_{L,l}\cdot\vec{r}_i - \omega_{L,l}t)}(|\uparrow_i\rangle\langle\uparrow_i| + |\uparrow_i\rangle\langle\downarrow_i|). \quad (69)$$

These jump operators lead to an effective scattering rate of $\Gamma_{\text{eff}} \sim \Gamma(\Omega_{l,s}^i/\Delta)^2$ which, in the limit of very large detunings, can be made much smaller than the dipole-force amplitudes in Eq. (30) which scale with $(\Omega_{l,s}^i)^2/\Delta$.

In the expressions of the effective jump operators in Eq. (69), the first addend terms on the right, which are proportional to $(I \pm Z_i)/2$ correspond to the elastic Rayleigh photon scattering that does not modify the internal qubit states. The second addend terms in Eq. (69), which are proportional to the raising and lowering spin operators $\sigma_i^+ = (X_i + \mathrm{i}Y_i)/2$ and $\sigma_i^- = (X_i - \mathrm{i}Y_i)/2$, correspond to the Raman scattering, where the qubit state is flipped after the emission of the photon. Let us now calculate the contribution of each scattering event to the light-shift gate fidelity.

1. Rayleigh scattering errors

Moving to the interaction picture with respect to the complete Hamiltonian, the contribution to Eq. (67) from Rayleigh scattering is

$$\mathcal{D}_{sc}^{\text{Rai}}(\rho_I(t)) = \sum_i \Gamma_{\text{sc,i}}^{\text{Rai}}[Z_i\rho_I(t)Z_i - \rho_I(t)], \quad (70)$$

which induces pure dephasing as in Eq. (61). $\Gamma_{\text{sc,i}}^{\text{Rai}}$ is the dephasing rate due to the elastic Rayleigh scattering given by

$$\Gamma_{\text{sc},i}^{\text{Rai}} = \frac{\Gamma}{\Delta}\delta\tilde{\omega}_{0,i} \approx \frac{\Gamma}{\Delta}\left(\sum_{l=1,2}\frac{|\Omega_{l,\downarrow}^i|^2 + |\Omega_{l,\uparrow}^i|^2}{4\Delta}\right), \quad (71)$$

where $\delta\tilde{\omega}_{0,i}(t)$ as in Eq. (26). In the last step, since $(\Gamma/\Delta) \ll 1$, we can also assume that $\frac{\Gamma}{\Delta}(\frac{\Omega_{l,s}^2}{\Delta}) \ll \Delta\omega_L \simeq \omega_x$, and thus, the oscillating part in $\delta\tilde{\omega}_{0,i}(t)$ can be neglected in a rotating-wave approximation. Since the effect of Rayleigh scattering is analogous to uncorrelated dephasing, we can use the results of the previous section, and express the gate infidelity as

$$\epsilon_{\text{Rai}}^{\text{scatt}} = \tfrac{4}{5}N\big(t_g/2T_2^{\text{eff}}\big), \quad (72)$$

with the particularity that now the coherence time is related to the elastic-scattering rate as $T_2^{\text{eff}} = 1/\Gamma_{\text{Rai},i}^{\text{sc}}$.

2. Raman scattering errors

Next, we calculate the leading error due to Raman scattering, which, in contrast with Rayleigh scattering, leads to the damping of the qubit populations. The contribution to Eq. (67) from Raman scattering in the interaction picture is

$$\mathcal{D}_{sc}^{\text{Ram}}(\tilde{\rho}) = \sum_{i=1}^N\left[\Gamma_{\text{em},i}^{\text{Ram}}\left(\tilde{\sigma}_i^-\tilde{\rho}\tilde{\sigma}_i^+ - \frac{1}{2}\{\tilde{\sigma}_i^+\tilde{\sigma}_i^-, \tilde{\rho}\}\right) + \Gamma_{\text{ab},i}^{\text{Ram}}\left(\tilde{\sigma}_i^+\tilde{\rho}\tilde{\sigma}_i^- - \frac{1}{2}\{\tilde{\sigma}_i^-\tilde{\sigma}_i^+, \tilde{\rho}\}\right)\right], \quad (73)$$

with $\tilde{\sigma}_i^\pm = U_{id}(t)\sigma_i^\pm U_{id}^\dagger(t)$ being the rotating-frame spin ladder operators, $\tilde{\rho} = U_{id}(t)\rho U_{id}^\dagger(t)$ the evolution operator in the interaction picture, and $U_{id}(t)$ describing the perfect unitary evolution (32). $\Gamma_{\text{abs},i}^{\text{Ram}}$ and $\Gamma_{\text{em},i}^{\text{Ram}}$ are the absorption and emission rates, respectively, given by

$$\Gamma_{\text{em},i}^{\text{Ram}} = \frac{\Gamma}{\Delta}\left(\sum_{l=1,2}\frac{\Omega_{l,\downarrow}^i\Omega_{l,\uparrow}^{i*}}{\Delta}\right) = \big(\Gamma_{\text{abs},i}^{\text{Ram}}\big)^*, \quad (74)$$

which are approximately equal.

The effect of the Raman absorption and emission on the gate error can be calculated following a strategy as with other weak sources of noise. In this case, the solution to the interaction-picture master equation $\dot{\rho}_I(t_g) = \mathcal{D}_{sc}^{\text{Ram}}(\rho_I(t_g))$ for the specific matrix element that appears in the calculation of entanglement fidelity (42) allows us to find the following contribution to the gate error:

$$\epsilon_{\text{Ram}}^{\text{scatt}} = \tfrac{6}{5}N(t_g/T_1), \quad (75)$$

where the amplitude damping time is defined as $T_1 = 1/2|\Gamma_{\text{em}}^{\text{Ram}}|$. The total error due to the residual photon scattering involving the contributions from Rayleigh and Raman scattering is $\epsilon_g^{\text{scatt}} = \epsilon_{\text{Rai}}^{\text{scatt}} + \epsilon_{\text{Ram}}^{\text{scatt}}$. In Table I, we provide further details specifically for $N = 2$ ions

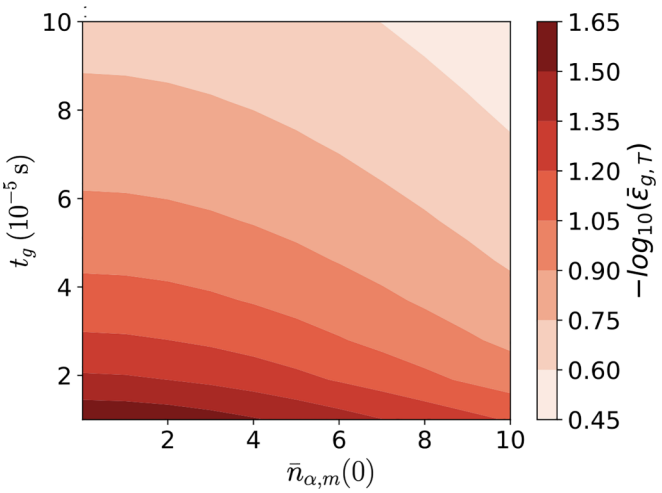

FIG. 5. Total gate error $\bar{\epsilon}_{g,T}$ as a function of the gate time t_g and the initial average vibrational occupation number $\bar{n}_{\alpha,m}(0)$. We assume here that for each axis $\alpha = x, y, z$, all modes m are cooled down to the same $\bar{n}_{\alpha,m}(0)$, before running the parity-check circuits.

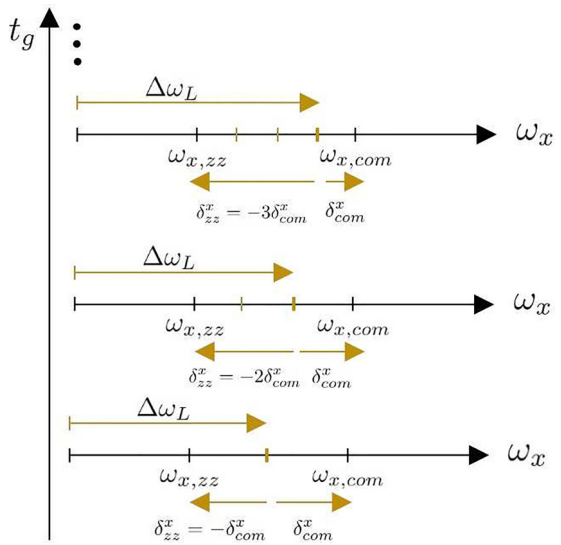

FIG. 6. Adjusting phase-loop detunings for the radial $\alpha = x$ trap frequency modes. For a target gate time t_g, we need to set the detuning δ^x_m for the $m = \{\mathrm{com}, \mathrm{zz}\}$ modes such that $\delta^x_{\mathrm{com}} = 2\pi r$ and $\delta^x_{\mathrm{zz}} = \delta^x_{\mathrm{com}} p$ with $r, p \in \mathbb{Z}$ to ensure that both trajectories are closed in phase space. The detuning $\delta^x_m = \omega_{x,m} - \Delta\omega_L$, can be adjusted by setting $\Delta\omega_L$ the beat-note frequency to different fractions of the frequency difference between $\omega_{x,\mathrm{com}}$ and $\omega_{x,\mathrm{zz}}$, that is $\Delta\omega_L = f_1\omega_{x,\mathrm{zz}} + f_2\omega_{x,\mathrm{zz}}$ with f_1 and f_2 the fractional quantities.

In Fig. 5, we present the total average gate infidelity $\bar{\epsilon}_g^{\mathrm{tot}}$ as a function of the gate time t_g, and of the initial average vibrational occupation number $\bar{n}_{\alpha,m}$. For the displayed results, we have assumed that all the modes m for the different axes $\alpha = x, y, z$ are initially Doppler- and sideband-cooled up to the same average phonon number $\bar{n}_{\alpha,m}$. The gate infidelity values shown in Fig. 5 range between 2.4×10^{-2} and 0.30, which are higher than the gate infidelity values expected for performing FT-QEC. However, to show $\mathrm{tr}(W_n\rho) = 0$ we consider higher possible errors. Recall that we are focusing on two-qubit light-shift gates mediated by the radial phonons along the x axis. The values for the trapping frequencies are $\omega_{x,m}/2\pi = \{4.64, 4.37\}$ MHz, $\omega_{y,m}/2\pi = \{3.88, 3.57\}$ MHz and $\omega_{z,m}/2\pi = \{1.49, 2.57\}$ MHz for the two normal modes $m = \{\mathrm{com}, \mathrm{zz}\}$ [38]. The laser beams are slightly misaligned with respect to the $\alpha = x$ axis, $\Delta\vec{k}_L \parallel \boldsymbol{e}_x = -0.5$ rad. The Rabi frequency of the dipole-allowed transitions is set to $\omega_L = 0.1\omega_{x,\mathrm{com}}$, and the detuning of both lasers from the dipole-allowed transitions are set to $\Delta_l/2\pi = -100$ GHz, with the decay from the P-manifold set by the decay rate $\Gamma/2\pi \approx 22$ MHz.

For the light-shift gate, the beat-note frequency of the laser $\Delta\omega_L$ is set to $f_1\omega_{x,\mathrm{com}} + f_2\omega_{x,\mathrm{zz}}$ where f_1 and f_2 are constants. The detunings to close the loops in phase space $\delta^x_m = \omega_{x,m} - \Delta\omega_L$ satisfy $\delta^x_{\mathrm{com}} = 2\pi r$ and $\delta^x_{\mathrm{zz}} = 2\pi p$ with $r, p \in \mathbb{Z}$. In Fig. 6, we show the way we adjusted the detunings when sweeping across gate times from 10 to 100 μs. If the gate time increases, the values of the frequency modes have to be reduced to achieve smaller detunings δ^x_m. However, to keep values consistent with the experiment, we cannot reduce the trap frequencies indefinitely. What we do instead is to change where we set the beat-note frequency in 1/2, 2/3, 3/4, … and so on. This helps to decrease the detuning values without the need to reduce the trap frequencies, at the expense of increasing the number of loops in one of the modes. We consider a coherence time $T_2 = 2.1$ s [15] and the T_1 time which is set at $T_1 = 1/2\Gamma^{\mathrm{Ram}}_{\mathrm{em},i} \approx [2(\frac{\Gamma}{\Delta_l})\frac{\omega_L^2}{\Delta_l}]^{-1}$ according to the Raman-scattering rate. We also ensure that $T_2^{\mathrm{eff}}(\Gamma/\Delta_l) \ll 1$ is fulfilled.

G. Effective error channels

During QEC cycles, the individual parity-check readout circuits consist of sequences of single-qubit gates and two-qubit light-shift gates that map the information from data qubits onto ancillary qubits. Typically, the circuit noise is modeled by introducing a quantum noise channel after each gate which, with some probability p, leads to a single or two-qubit error on the physical qubits participating in the gate, whereas with a probability $1 - p$, the qubits are left unaffected.

In this section, we discuss different effective error models for two-qubit light-shift gates, which are the bottleneck in the current trapped-ion implementations. We use all the microscopic error contributions to the U_{id} gate calculated in Sec. III to extract the error rate p that is fed into different two-qubit error channels, such as the depolarizing channel and the two-qubit dephasing channel, instead of assuming arbitrary values of p.

We can achieve this by establishing a connection between the analytical expression of the microscopic gate infidelity (i) $\bar{\epsilon}_{g,T}(\epsilon_g^{\mathrm{th}} + \epsilon_g^{\mathrm{off}} + \epsilon_g^{\mathrm{deph}} + \epsilon_g^{\mathrm{scatt}})$, and (ii) the gate infidelity we get when introducing an effective two-qubit noise channel [e.g., depolarizing $\bar{\epsilon}_{g,T}(p_{dp})$ or dephasing $\bar{\epsilon}_{g,T}(p_{\mathrm{deph}})$] following the ideal unitary, with p_{dp} and p_{deph} being the error rates for each channel, respectively. By matching expressions (i) and (ii), the error rates p_{dp} and p_{deph} can be written in terms of the microscopic error parameters, i.e., $p_{dp}, p_{\mathrm{deph}} \to \epsilon_g^{\mathrm{th}} + \epsilon_g^{\mathrm{off}} + \epsilon_g^{\mathrm{deph}} + \epsilon_g^{\mathrm{scatt}}$.

1. Two-qubit depolarizing noise

For a two-qubit depolarizing noise channel, each pair of ions involved in a light-shift gate can undergo 15 possible one- and two-qubit Pauli errors, so that the total error channel is described as

$$\epsilon_{dp}(\rho) = (1 - p_{dp})\rho + \frac{p_{dp}}{15} \sum_{(\sigma_i,\kappa_j)\in\mathcal{Y}} \sigma_i\kappa_j\rho\kappa_j\sigma_i. \tag{76}$$

Here, i and j with $i \neq j$ denote the active ions involved in each two-qubit entangling gate, p_{dp} is the error probability, and the sum on the right runs over the six nontrivial single-qubit and the nine nontrivial two-qubit Pauli operators in $\mathcal{Y} = \{I, X, Y, Z\}^2/(I, I)$. Here, we have considered a symmetric two-qubit depolarizing channel, where the probability of single and two-qubit errors is the same. Next, by making $\epsilon_{dp}(\rho) = \epsilon(|\phi_m\rangle\langle\phi_m|)$ we calculate the entanglement fidelity (42) in terms of p_{dp}. One finds

$$\bar{\mathcal{F}}_e = |1 - p_{dp}|^2 = 1 - 2p_{dp} + O\big(p_{dp}^2\big), \tag{77}$$

which means that the effect of all the possible errors perturbing the target state, i.e., bit and phase-flip errors, is on average null. In this case, we find that the two-qubit errors $\{XX, YZ, ZY\}$ contribute positively $(+1)$ or negatively (-1) to the probability p_{dp} depending on the initial input state $|\alpha\rangle \in \{|{+}{+}\rangle, |{+}{-}\rangle, |{-}{+}\rangle, |{-}{-}\rangle\}$ so that, on average, their effects cancel out. Finally, the average gate fidelity from Eq. (43) allows us to fix the channel error rate to

$$\bar{\mathcal{F}}_g = 1 - \tfrac{8}{5}p_{dp} \rightarrow p_{dp} = \tfrac{5}{8}\bar{\epsilon}_{g,T}, \tag{78}$$

where we have used $\bar{\epsilon}_{g,T} = 1 - \bar{\mathcal{F}}_g$.

2. Two-qubit dephasing noise

As per discussion in the previous section, there is a privileged basis for error channels (except the Raman scattering), namely, the Z basis. With the exception of the Raman scattering, all the other sources of error act on such a phase-flip basis. Accordingly, it is expected that dephasing-type errors be more dominant than bit-flip errors, or a combination of both. Thus, it is more reasonable to consider a two-qubit dephasing channel

$$\epsilon_{\text{deph}}(\rho) = (1 - p_{\text{deph}})\rho + \frac{p_{\text{deph}}}{3} \sum_{(\sigma_i,\kappa_j)\in\mathcal{I}} \sigma_i\kappa_j\rho\kappa_j\sigma_i, \tag{79}$$

where i and j represent the active ions involved in the two-qubit gate, and $\mathcal{I} = \{I, Z\}^2/(I, I)$. The quantum channel in Eq. (79) is also symmetric, where all the errors $\{IZ, ZI, ZZ\}$ occur with the same probability p_{deph}. As before, we can compute the entanglement fidelity for this channel by introducing $\epsilon_{\text{deph}} = \epsilon(|\phi_m\rangle\langle\phi_m|)$ into the entanglement fidelity (42). We arrive at a similar result as for the depolarizing channel, $\bar{\mathcal{F}}_e \approx 1 - p_{\text{deph}}$. In this case, all single and two-qubit dephasing errors affect the expected output state. Thus, the relation between the dephasing error rate p_{deph} and the average gate infidelity is

$$\bar{\mathcal{F}}_g = 1 - \tfrac{8}{5}p_{\text{deph}} \rightarrow p_{\text{deph}} = \tfrac{5}{8}\bar{\epsilon}_{g,T}, \tag{80}$$

leading to a similar relation as in the depolarizing noise model. Note, however, that the effect of these channels will be different for the specific circuits and target n-qubit entangled states.

We have thus shown how to relate the error probabilities for different effective noise channels with the average gate infidelities of the light-shift gates that arise from detailed microscopic calculations. Here, even though the weight of the error probability with the average gate fidelity is the same for both cases, i.e., $5/8$, the structure of the noise is different and would propagate differently through the circuit [58]. In the following section, we address this question: can the noise structure of both channels lead to better or worse performance of the corresponding circuit? And can one modify the circuits to leverage our detailed knowledge of the microscopic noise?

IV. CHARACTERIZATION OF NOISY TRAPPED-ION QUANTUM ERROR CORRECTION CIRCUITS VIA ENTANGLEMENT WITNESSES

In this section, taking previous works [38,58] a step further we evaluate the performance of the parity check measurement circuits in terms of their ability to generate GME states in the presence of realistic microscopic noise. For the numerical simulations, the chosen error model in this work includes perfect light-shift gate operations followed by a two-qubit depolarizing (76) or a two-qubit dephasing (79) channel on the active qubits. We include measurement errors for the Pauli operator readouts and neglect errors on single-qubit gates since it has been shown that for this particular experimental setup [33], they are negligible in comparison to the two-qubit and measurement errors.

We focus on experiments with trapped-ion crystals of a single atomic species, which are shuttled around in order to perform the sequence of single- and two-qubit gates by bringing the corresponding ions to operation zones of a segmented trap where they can be coupled to lasers. In this work, we assume that all the vibrational modes, active and spectator, have the same average number of phonons after the Doppler and sideband cooling processes. Since we do not have mixed species at our disposal, no sympathetic cooling is considered, and the entangling gates will get worse due to the heating caused by the intermediate shuttling operations. This effect is directly accounted for by our expressions of the gate errors i.e., thermal errors contributions in Table I and their relations to the error-channel rates. Finally, we note that in Ref. [15], it was shown that stable magnetic fields lead to a negligible dephasing of qubits during the idle-time intervals in which they are not acted upon. Thus, we assume that during gates and shuttling operations in between, idle qubits do not suffer from dephasing noise.

For the numerical simulations, we model the errors during measurement by including an effective noise channel for the projection operators. The single-qubit Pauli operator $\sigma \in \{X, Y, Z\}$ can be measured using the corresponding error-free positive operator-valued measure (POVM) [1] $\{P_{\pm}^{\sigma} = (I \pm \sigma)/2\}$. However, for each measurement outcome, a bit-flip error can take place with probability p_{me}, which gives rise to the erroneous effect operators

$$P_{+}^{\sigma} \mapsto (1 - p_{\text{me}})P_{+}^{\sigma} + p_{\text{me}}P_{-}^{\sigma}, \tag{81}$$

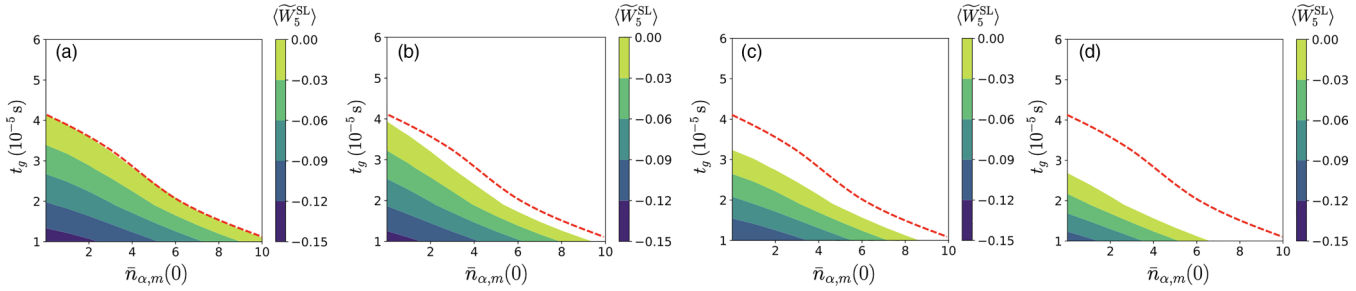

FIG. 7. SL witnessing for a X-type parity-check readout circuit under effective microscopic noise channels. The color bar indicates the value of the witness. For all the colors represented, the witness takes a negative value signaling the presence of entanglement. The white area represents all positive values of the witness values where the verification is inconclusive. The red dashed line fits the perimeter area of the (a) non-FT X-type circuit under a two-qubit depolarizing noise channel. Then, the red dashed line is plotted on top of the following graphs to benchmark the size of the enclosed colored area on the (b) flag-based FT X-type circuit under depolarizing noise, and for (c) the non-FT and (d) FT X-type circuits under dephasing noise, respectively. This witness is reconstructed using the following 5-qubit stabilizer generators $g_1 = Z_1Z_2$, $g_2 = Z_2Z_3$, $g_3 = Z_3Z_4$, $g_4 = Z_4Z_5$, $g_5 = X_1X_2X_3X_4X_5$ of the state $(|00000\rangle + |11111\rangle)/\sqrt{2}$.

and

$$P_-^\sigma \mapsto (1 - p_{\mathrm{me}})P_-^\sigma + p_{\mathrm{me}}P_+^\sigma. \tag{82}$$

For all the simulation results shown in this paper, the measurement error probability is set to $p_{me} = 10^{-3}$ [13]. We now analyze the numerical results for the SL and the CL witnessing methods.

1. Numerics for the standard linear witnessing

In Fig. 7, we show the entanglement witnessing results for the X-type parity-check readout circuits of Figs. 2 and 3 following the standard linear method described in Sec. II C 1. The results for the Z-type parity checks measurement circuits are practically the same since the error propagation of one- and two-qubit Pauli operators from either depolarizing or dephasing channel through the native gates leads to a similar result in terms of number of expectation values of the stabilizer generators flipped, which is the same profile and the number of $\langle g_i \rangle = -1$ as when the propagation of errors is evaluated in an X-type parity-check circuit. Note that, when the stabilizers (15) flip, the corresponding values of the test operators described above will decrease, which can make the result of the witness measurement inconclusive.

For the simulation, we have used the same parameters used to generate Fig. 5. We plot the results for different gate times t_g and for different initial average phonon numbers $\bar{n}_{\alpha,m}(0)$, which will change the gate error and the corresponding channel parameters. Recall that all modes are cooled down to the same initial phonon occupation number. However, after each entangling gate, the phonon number increases, which can be estimated to contribute with $\dot{\bar{n}}_{ax} = 3.9$ phonons for the z-axial direction (shuttling axis), and $\dot{\bar{n}}_{ra} = 0.255$ for the radial x- and y-axis directions [101]. In our simulations, after each entangling gate: $\bar{n}_{\alpha,m}(0) \to \bar{n}_{\alpha,m}(0) + k\dot{\bar{n}}_{\alpha,m}$, where $k \in \mathbb{Z}$ indicates the location of the gate in the circuit. In this model, the average phonon number grows linearly with the gate's position in the circuit (depth).

Figures 7(a) and 7(b) show the results for the non-FT and flag-based X-type circuits under the effective depolarizing channel described in Sec. III G 1. Figures 7(c) and 7(d) show the results for the same circuits in the presence of the effective dephasing channel of Sec. III G 2. The red dashed line represents the boundary between the region in parameter space where errors are low, and we can conclusively detect GME via the witness, and an inconclusive outer region. One can notice that, in Fig. 7, the entanglement witnessed area reduces from left to right. With the SL witness built from stabilizers $\langle g_1 = Z_1Z_2,\ g_2 = Z_2Z_3,\ g_3 = Z_3Z_4,\ g_4 = Z_4Z_5,\ g_5 = X_1X_2X_3X_4X_5 \rangle$ we can detect more entangled states for the same physical parameters when the circuits are affected by the depolarizing noise channel (76) than when they are subjected to the dephasing channel (79). We refer to them as the nearest-neighbor (NN) generators.

Another way to visualize the performance of the entanglement witness is by comparing its expectation value as a function of the effective error probability, denoted $p(t_g, \bar{n}_{\alpha,m}(0))$. The latter is a function of the gate time t_g and the initial average number of phonons $\bar{n}_{\alpha,m}(0)$. Recall from Eqs. (78) and (80) that both the depolarizing error probability p_{dp} and the dephasing error probability p_{deph} are equally weighted in the total average gate infidelity, i.e., 5/8. Hence, we can use the same values $p(t_g, \bar{n}_{\alpha,m}(0))$ to simulate both channels. In Fig. 8, we present the entanglement witnessing results, similar to Fig. 7, as a function of $p(t_g)$, while fixing the initial average phonon numbers, $\bar{n}_{\alpha,m}(0)$. Each column in Fig. 8, labeled (a) to (d), corresponds to the four scenarios depicted in Fig. 7: X-type (a) non-FT circuit and (b) flag-based FT circuit under a two-qubit depolarizing noise; (c) non-FT circuit, and (d) FT flag-based circuit under dephasing noise. Within each column, the subplots, denoted i = 1, 2, and, 3, represent three different initial values of $\bar{n}_{\alpha,m}(0) = 0.01$, 2, and 6. The red dashed line, where $\widetilde{W}_5^{\mathrm{SL}} = 0$, serves as the boundary between the conclusive and inclusive witnessing domains. The threshold value of $p(t_g)$ at which the witness line (black solid) intersects with the boundary gives us the maximum error probability per entangling gate that the circuit in Figs. 2 and 3 can tolerate before the entanglement detection becomes inconclusive. The threshold value decreases from left to right, following a similar pattern as described in Fig. 7, and decreases in all cases (from top to bottom within each column) with increasing the initial average phonon number.

To better understand the entanglement witnessing areas and the noise channels, we count the number of stabilizers

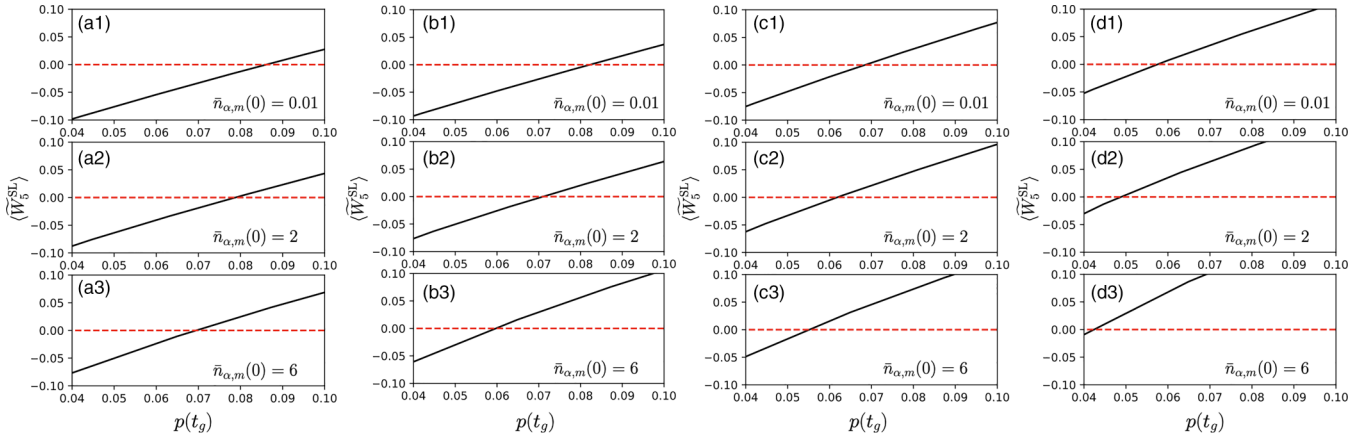

FIG. 8. SL witnessing for an X-type parity-check readout circuit in terms of the effective error probability $p(t_g)$ derived from microscopic noise parameter. The red dashed line, where $\widetilde{W}_5^{\mathrm{SL}} = 0$, indicates the boundary above which the verification is inconclusive. From left to right, the subplots depict the result for X-type (ai) non-FT circuit, (bi) flag-based FT, under a two-qubit depolarizing noise channel, (ci) non-FT circuit, and (di) flag-based FT under dephasing noise. Within each column, the index i = 1, 2, 3 represents different initial values of $\bar{n}_{\alpha,m} = 0.01, 2, 6$, respectively. The SL witness is reconstructed using the following 5-qubit stabilizer generators $g_1 = Z_1Z_2$, $g_2 = Z_2Z_3$, $g_3 = Z_3Z_4$, $g_4 = Z_4Z_5$, $g_5 = X_1X_2X_3X_4X_5$ of the state $(|00000\rangle + |11111\rangle)/\sqrt{2}$.

flipped by the error operators (cf. Table II), that is, how many turns into $\langle g_i \rangle = -1$, when a single or a two-qubit error from the depolarizing channel propagates through the circuit of Fig. 2. Let us note that these tables are expected to provide a rough estimate of the performance of the GME witness for finite error rates, which should become more and more reliable as the error rate decreases, as errors are only linear in p. In Table III, we show the same results but for the single and two-qubit phase errors. We calculate the ratio between the number of stabilizer generators that change sign when an error occurs, versus the total number of generators measured for all different types of errors. These error propagations and stabilizer flips show that using a dephasing channel after each entangling gate leads to more stabilizer flips than a depolarizing channel. In fact, Table II, the percentage of "-1" goes as %21, %32, %32, %32, for the depolarizing errors applied after the first, second, third, and fourth entangling gate, respectively. However, for the dephasing-type errors in Table III, that percentage increases up to %40. A larger number of $\langle g_i \rangle = -1$, consequently reduces the value of the witness test operator against the entanglement bound [see Eq. (17)], and thus the negativity of the witness.

From the perspective of the different behavior of the errors with respect to the flipped stabilizers, it is possible to try to construct witnesses that are more robust for a particular type of noise by just looking at its error propagation through the circuit. In Figs. 9 and 10, we plot the numerical results for the X-type parity-check readout circuits depicted in Figs. 2 and 3. These results follow the standard linear method described before but we employ a different set of stabilizer generators compared with those mentioned above. Specifically, $\langle g'_1 = Z_1Z_5,\ g'_2 = Z_2Z_5,\ g'_3 = Z_3Z_5,\ g'_4 = Z_4Z_5,\ g_5 = X_1X_2X_3X_4X_5 \rangle$, which will be referred the in the text as Z_5-biased generators. With these new generators, we are able to construct a witness that exhibits a larger witnessed entanglement area for the dephasing channel [see Figs. 9(c) and 10(ci)] than it does for the depolarizing channel, as shown in Figs. 9(a) and 10(ai), respectively. This reverts the behavior observed in Figs. 7 and 8. The fact that, under the dephasing channel, we obtain better results for the Z_5-biased generators than for the NN ones can be justified as follows: (i) the Z_dI_5 errors with $d = 1, 2, 3, 4$, transforms into the X_dI_5 type of errors at the end of the circuit, causing just one "-1" sign flip for the Z_5-biased stabilizers. On the other hand, for the NN-type generators, it can contribute with up to two, e.g., $Z_2I_5 \rightarrow X_2I_5$ flips the Z_1Z_2 and Z_2Z_3 generators. (ii) I_dZ_5 errors change the sign of $g_5 = X_1X_2X_3X_4X_5$ for both type of generators. Finally, (iii) Z_dZ_5 errors, which are the product of the other two types, contribute to up to three sign flips of the NN-type generators. On the other hand, at most two sign flips can occur for the Z_5-biased generators. In other words, the Z_5-biased stabilizers commute with more dephasing errors than the NN-type generators do, and consequently, there are more "$+1$" values helping to increase the difference between the entanglement test operator and its entanglement bound, and consequently, the negativity of the witness. We can also corroborate these results by looking at the individual error propagation for the depolarizing and dephasing channels of the Z_5-biased generators in Tables IV and V, respectively. We note that the percentage of "-1" sign flips for the dephasing channel is around %27, while it is, in the majority of cases, higher for the depolarizing channel. We note, then, that the numerical and tabulated results agree for the case of the non-FT circuits. By looking at Figs. 9(b) and 9(d), and similarly, in Figs. 10(bi) and 10(di), we confirm again that the FT circuit design with the flag-qubit is not advisable for gates with high failure rates. Thus, if one wants to qualitatively characterize the performance of QEC circuits in terms of SL witnesses, it is important to construct an optimal witness; that is, one whose generators commute with the largest number of errors propagated through the circuit.

Similarly, for the flag based FT circuits in Figs. 7(b) and 7(d) [Figs 8(bi) and 8(di)], it looks like the flag qubit and the associated postselection does not help to increase the robustness of the GME witness. In fact, the additional entangling gates between the syndrome and flag qubits, which are

TABLE II. One- and two-qubit depolarizing errors propagating through a non-FT X-type parity-check circuit. The subscripts on the Pauli operators refer to the qubits affected by the errors after the application of the entangling light-shift gate on those two qubits. ±1 numbers refers to the expectation of the stabilizer generators $g_1 = Z_1Z_2$, $g_2 = Z_2Z_3$, $g_3 = Z_3Z_4$, $g_4 = Z_4Z_5$, $g_5 = X_1X_2X_3X_4X_5$.

Error	g_1	g_2	g_3	g_4	g_5	No. of -1s	Error	g_1	g_2	g_3	g_4	g_5	No. of -1s
X_1I_5	-1	1	1	1	-1	2	X_2I_5	-1	-1	1	1	-1	3
I_1X_5	-1	1	1	1	-1	2	I_2X_5	1	-1	1	1	1	1
X_1X_5	1	1	1	1	1	0	X_2X_5	-1	1	1	1	-1	2
X_1Y_5	1	1	1	1	-1	1	X_2Y_5	-1	1	1	1	1	1
Y_1X_5	-1	1	1	1	1	1	Y_2X_5	1	-1	1	1	-1	2
X_1Z_5	-1	1	1	1	1	1	X_2Z_5	-1	-1	1	1	1	2
Z_1X_5	1	1	1	1	-1	1	Z_2X_5	-1	1	1	1	1	1
Y_1I_5	1	1	1	1	-1	1	Y_2I_5	1	1	1	1	-1	1
I_1Y_5	-1	1	1	1	1	1	I_2Y_5	1	-1	1	1	-1	2
Y_1Y_5	-1	1	1	1	-1	2	Y_2Y_5	1	-1	1	1	1	1
Y_1Z_5	1	1	1	1	1	0	Y_2Z_5	1	1	1	1	1	0
Z_1Y_5	1	1	1	1	1	0	Z_2Y_5	-1	1	1	1	-1	2
Z_1I_5	-1	1	1	1	1	1	Z_2I_5	-1	-1	1	1	1	2
I_1Z_5	1	1	1	1	-1	1	I_2Z_5	1	1	1	1	-1	1
Z_1Z_5	-1	1	1	1	-1	2	Z_2Z_5	-1	-1	1	1	-1	3
Total: 16/75; %21							Total: 22/75; %32						
X_3I_5	1	-1	-1	1	-1	3	X_4I_5	1	1	-1	-1	-1	3
I_3X_5	1	1	-1	1	-1	2	I_4X_5	1	1	1	-1	1	1
X_3X_5	1	-1	1	1	1	1	X_4X_5	1	1	-1	1	-1	2
X_3Y_5	1	-1	1	1	-1	2	X_4Y_5	1	1	-1	1	1	1
Y_3X_5	1	1	-1	1	1	1	Y_4X_5	1	1	1	-1	-1	2
X_3Z_5	1	-1	-1	1	1	2	X_4Z_5	1	1	-1	-1	1	2
Z_3X_5	1	-1	1	1	-1	2	Z_4X_5	1	1	-1	1	1	1
Y_3I_5	1	1	1	1	-1	1	Y_4I_5	1	1	1	1	-1	1
I_3Y_5	1	1	-1	1	1	1	I_4Y_5	1	1	1	-1	-1	2
Y_3Y_5	1	1	-1	1	-1	2	Y_4Y_5	1	1	1	-1	1	1
Y_3Z_5	1	1	1	1	1	0	Y_4Z_5	1	1	1	1	1	0
Z_3Y_5	1	-1	1	1	1	1	Z_4Y_5	1	1	-1	1	-1	2
Z_3I_5	1	-1	-1	1	1	2	Z_4I_5	1	1	-1	-1	1	2
I_3Z_5	1	1	1	1	-1	1	I_4Z_5	1	1	1	1	-1	1
Z_3Z_5	1	-1	-1	1	-1	3	Z_4Z_5	1	1	-1	-1	-1	3
Total: 24/75; %32							Total: 24/75; %32						

TABLE III. One- and two-qubit dephasing errors propagating through a non-FT X-type parity-check circuit. The subscripts on the Pauli operators refer to the qubits affected by the errors after the application of the entangling light-shift gate on those two qubits. The ±1 numbers refers to the expectation of the stabilizer generators $g_1 = Z_1Z_2$, $g_2 = Z_2Z_3$, $g_3 = Z_3Z_4$, $g_4 = Z_4Z_5$, $g_5 = X_1X_2X_3X_4X_5$.

Error	g_1	g_2	g_3	g_4	g_5	No. of -1s	Error	g_1	g_2	g_3	g_4	g_5	No. of -1s
Z_1I_5	-1	1	1	1	1	1	Z_2I_5	-1	-1	1	1	1	2
I_1Z_5	1	1	1	1	-1	1	I_2Z_5	1	1	1	1	-1	1
Z_1Z_5	-1	1	1	1	-1	2	Z_2Z_5	-1	-1	1	1	-1	3
Total: 4/15; %27							Total:6/15; %40						
Z_3I_5	1	-1	-1	1	1	2	Z_4I_5	1	1	-1	-1	1	2
I_3Z_5	1	1	1	1	-1	1	I_4Z_5	1	1	1	1	-1	1
Z_3Z_5	1	-1	-1	1	-1	3	Z_4Z_5	1	1	-1	-1	-1	3
Total: 6/15; %40							Total: 6/15; %40						

included to catch dangerous weight-2 errors to allow for an FT readout, actually add more noise in terms of spin flips for the stabilizer generators of the GHZ-type state. To show this, we have proceeded similarly as before, performing the error propagation for the flag-based circuits of Fig. 3. In Tables VI and VII, we show the error propagation of the depolarizing and dephasing channels, counting only the flipped $\langle g_i\rangle = -1$ instances in which the flag-qubit has been measured, and post-selected in the $|+\rangle$ state; that is, when $M_f(X) = +1$ and we get right of dangerous weight-2 errors. We can clearly verify the increased number of stabilizer flips for the dephasing noise, by comparing these tables with those of the non-FT circuits, i.e., Tables III and VII. Even if the postselection gets rid of some weight-2 errors that would deteriorate the GHZ-type state, the price to pay is to introduce more faulty light-shift gates that result in more stabilizer flips and thus do not reduce the percentage of "-1" values, but instead add an extra %6 per entangling gate between syndrome and flag. This trend matches qualitatively the simulation results shown in Figs. 7(c) and 7(d).

All the errors in the Z basis are nondetectable by the flag, and, consequently, adding more gates, will just introduce more errors in the circuit. On the other hand, for the depolarizing channel, the simulations and the tabulated results seem contradictory. The flag qubit in Table VI helps to reduce the percentage of errors for the intermediate gates almost in half, at the expense, although, of putting in an extra %11 per entangling gate between syndrome and flag qubit. Despite this extra noise, the net result of having the flag is favorable, a lower number of "-1" are produced in the presence of the flag qubit. This apparently contradicts the results displayed in Figs. 7(a) and 7(b), where the enclosed GME-witnessing area for the flag-based circuit is smaller than for the non-FT case.

This discrepancy can be primarily due to the fact that we are considering high error probabilities, whereas the tables only consider erroneous events linear in such a probability. For the depolarizing channel, we are considering $p_{dp} > 10^{-2}$, which increases due to shuttling as the circuit proceeds, and similarly for the dephasing channel with $p_{\text{deph}} > 10^{-2}$. For the dephasing channel, as discussed above, the flag qubit under a dephasing channel would always add more noise than it could help to remove, even for low-error probabilities. On the other hand, for the depolarizing channel, this is not always the case. For lower failure probabilities, it has been shown that the flag-qubit helps to increase pseudothresholds in FT-QEC protocols [72]. For the GME-witnessing studied here, we need to use higher values of p_{dp} to show the boundary between the entanglement witnessed and the nonwitnessed regions. For such values, terms of order $O(p_{dp}^2)$ and higher become relevant, and the flag cannot cope with them. If we go to low failure probabilities with one error propagating at most in the circuit; that is, of the order of $O(p_{dp})$, the flag-qubit has indeed a positive effect, as it is shown in Table VI. On the

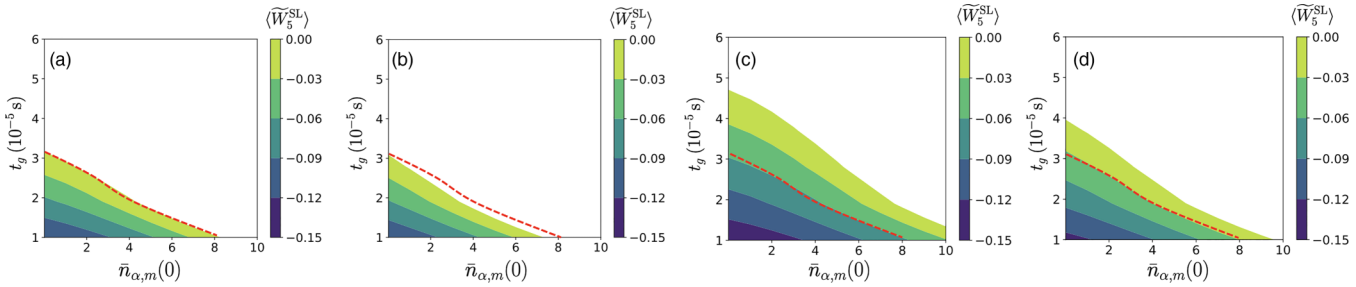

FIG. 9. SL witnessing for an X-type parity-check readout circuit under effective microscopic noise channels. The color bar indicates the value of the witness. For all the colors represented, the witness takes a negative value signaling the presence of entanglement. The white area represents all positive values of the witness values where the verification is inconclusive. The red solid line fits the perimeter area of the (a) non-FT X-type circuit under a two-qubit depolarizing noise channel. Then, the red dashed line is plotted on top of the following graphs to benchmark the size of the enclosed colored area on the (b) flag-based FT X-type circuit under depolarizing noise, and for (c) the non-FT and (d) FT X-type circuits under dephasing noise, respectively. This witness is reconstructed using the following 5-qubit stabilizer generators $g_1 = Z_1Z_5$, $g_2 = Z_2Z_5$, $g_3 = Z_3Z_5$, $g_4 = Z_4Z_5$, $g_5 = X_1X_2X_3X_4X_5$ of the state $(|00000\rangle + |11111\rangle)/\sqrt{2}$.

other hand, having a more negative witness cannot be used to ascertain that the circuit is performing better, as we can only detect when the state has GME. On the other hand, if we compute the state fidelity, its quantitative value can give us further confirmation that the above reasoning is correct.

In Figs. 11 and 12, we study a low-to-high error probability regime for p_{dp} and p_{deph} in terms of the state fidelity $\mathcal{F}_s$ of the output state generated by the X-type circuit. The three plots in Fig. 11 show the results for gate times t_g ranging from 1 μs up to 100 μs. In Fig. 11, we study the state fidelity as a function of t_g fixing $\bar{n}_{\alpha,m}(0)$, whereas in Fig. 12, we plot the state fidelities of both channels, as well as for the FT and non-FT X-type circuits as a function of $\bar{n}_{\alpha,m}(0)$ while fixing the gate time. From top to bottom, in Figs. 11(a)–11(c) we consider an initial phonon occupation number of $\bar{n}_{\alpha,m}(0) = 0.01$, $\bar{n}_{\alpha,m}(0) = 2$, and $\bar{n}_{\alpha,m}(0) = 6$, respectively. Meanwhile, Figs. 12(a)–12(c) correspond to a gate time $t_g = 1 \times 10^{-6}$ s, $t_g = 5 \times 10^{-6}$ s, and $t_g = 1 \times 10^{-5}$ s, respectively. Across all cases, the error probabilities increase from panels (a) to (c). In both figures, the black solid lines represent the state fidelities of the ideal output GME state against the output state generated by the non-FT X-type circuit in the presence of a depolarizing channel. The blue lines do the same but, for a flag-based FT circuit. The green lines represent the state fidelity values of the output state generated with a non-FT X-type parity check circuit in the ideal case and in the presence of a dephasing channel. The red line shows the results for the flag-based version under dephasing errors. We note that, just in Fig. 11(a) (see inset) and Fig. 12(a), which represent the lowest error probabilities, the flag qubit mitigates the effect of the depolarizing channel, yielding higher state fidelity results than for the non-FT version. However, for increasing error probabilities, as indicated by a smaller increase in $\bar{n}_{\alpha,m}(0)$ or t_g, the flag-qubit has a detrimental effect, as it can be seen in already in Fig. 11(a) for larger gate times, and in both figures for the plots in Figs. 11(b)–11(c) and Figs. 12(b)–12(c). That is the reason why there was an apparent discrepancy between the tabulated results in Table VI, which represent the low-error rate regime, and those in Figs. 7(a) and 7(b), which represent the higher-error regime. It is important to highlight

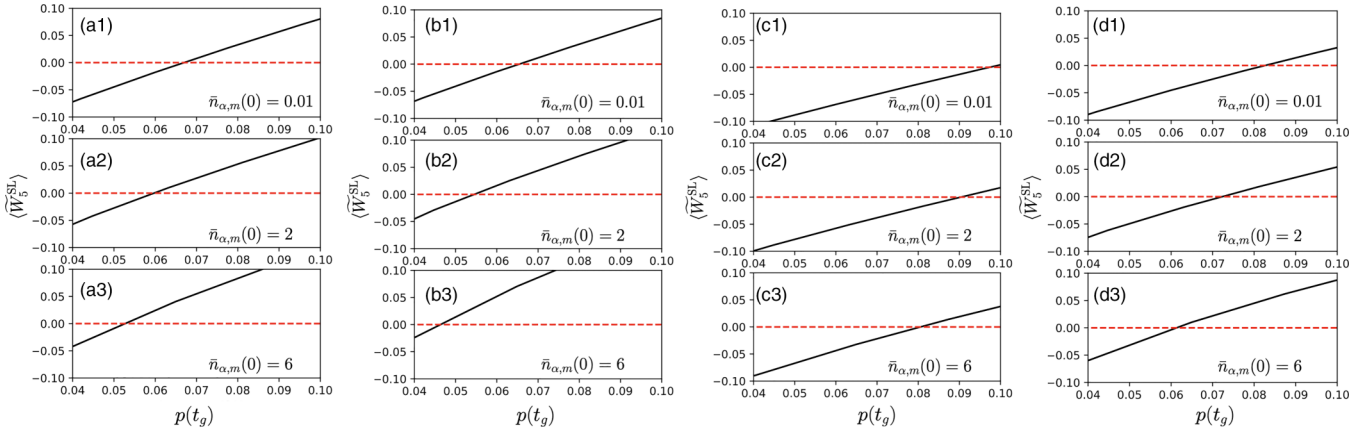

FIG. 10. SL witnessing for a X-type parity-check readout circuit in terms of the effective error probability $p(t_g)$ derived from microscopic noise parameter. The red dashed line, where $\widetilde{W}_5^{\mathrm{SL}} = 0$, indicates the boundary above which the verification is inconclusive. From left to right, the subplots depict the result for X-type (ai) non-FT circuit, (bi) flag-based FT, under a two-qubit depolarizing noise channel, (ci) non-FT circuit, and (di) flag-based FT under dephasing noise. Within each column, the index i = 1, 2, 3 represents different initial values of $\bar{n}_{\alpha,m} = 0.01, 2, 6$, respectively. The SL witness is reconstructed using the following 5-qubit stabilizer generators $g_1 = Z_1Z_5$, $g_2 = Z_2Z_5$, $g_3 = Z_3Z_5$, $g_4 = Z_4Z_5$, $g_5 = X_1X_2X_3X_4X_5$ of the state $(|00000\rangle + |11111\rangle)/\sqrt{2}$.

TABLE IV. One and two-qubit depolarizing errors propagating through a non-FT X-type parity-check circuit. The subscripts on the Pauli operators refer to the qubits affected by the errors after the application of the entangling light-shift gate on those two qubits. ±1 numbers refer to the expectation of the stabilizer generators $g_1' = Z_1Z_5$, $g_2' = Z_2Z_5$, $g_3' = Z_3Z_5$, $g_4' = Z_4Z_5$, $g_5 = X_1X_2X_3X_4X_5$.

Error	Syndrome	No. of -1s	Error	Syndrome	No. of -1s
X_1I_5	$-1\ 1\ 1\ 1-1$	2	X_2I_5	$1\ -1\ 1\ 1\ -1$	2
I_1X_5	$-1\ 1\ 1\ 1-1$	2	I_2X_5	$-1-1\ 1\ 1\ 1$	2
X_1X_5	$1\ 1\ 1\ 1\ 1$	0	X_2X_5	$-1\ 1\ 1\ 1\ -1$	2
X_1Y_5	$1\ 1\ 1\ 1-1$	1	X_2Y_5	$-1\ 1\ 1\ 1\ 1$	1
Y_1X_5	$-1\ 1\ 1\ 1\ 1$	1	Y_2X_5	$-1-1\ 1\ 1\ -1$	3
X_1Z_5	$-1\ 1\ 1\ 1\ 1$	1	X_2Z_5	$1\ -1\ 1\ 1\ 1$	1
Z_1X_5	$1\ 1\ 1\ 1-1$	1	Z_2X_5	$-1\ 1\ 1\ 1\ 1$	1
Y_1I_5	$1\ 1\ 1\ 1-1$	1	Y_2I_5	$1\ 1\ 1\ 1\ -1$	1
I_1Y_5	$-1\ 1\ 1\ 1\ 1$	1	I_2Y_5	$-1-1\ 1\ 1\ -1$	3
Y_1Y_5	$-1\ 1\ 1\ 1-1$	2	Y_2Y_5	$-1-1\ 1\ 1\ 1$	2
Y_1Z_5	$1\ 1\ 1\ 1\ 1$	0	Y_2Z_5	$1\ 1\ 1\ 1\ 1$	0
Z_1Y_5	$1\ 1\ 1\ 1\ 1$	0	Z_2Y_5	$-1\ 1\ 1\ 1\ -1$	2
Z_1I_5	$-1\ 1\ 1\ 1\ 1$	1	Z_2I_5	$1\ -1\ 1\ 1\ 1$	1
I_1Z_5	$1\ 1\ 1\ 1-1$	1	I_2Z_5	$1\ 1\ 1\ 1\ -1$	1
Z_1Z_5	$-1\ 1\ 1\ 1-1$	2	Z_2Z_5	$1\ -1\ 1\ 1\ -1$	2
Total: 16/75; %21			Total: 24/75; %32		
X_3I_5	$1\ 1\ -1\ 1-1$	2	X_4I_5	$1\ 1\ 1\ -1-1$	2
I_3X_5	$-1-1-1\ 1-1$	4	I_4X_5	$-1-1-1-1\ 1$	4
X_3X_5	$-1-1\ 1\ 1\ 1$	1	X_4X_5	$-1-1-1\ 1\ -1$	4
X_3Y_5	$-1-1\ 1\ 1-1$	3	X_4Y_5	$-1-1-1\ 1\ 1$	3
Y_3X_5	$-1-1-1\ 1\ 1$	3	Y_4X_5	$-1-1-1-1-1$	5
X_3Z_5	$1\ 1\ -1\ 1\ 1$	1	X_4Z_5	$1\ 1\ 1\ -1\ 1$	1
Z_3X_5	$-1-1\ 1\ 1-1$	3	Z_4X_5	$-1-1-1\ 1\ 1$	3
Y_3I_5	$1\ 1\ 1\ 1-1$	1	Y_4I_5	$1\ 1\ 1\ 1\ -1$	1
I_3Y_5	$-1-1-1\ 1\ 1$	3	I_4Y_5	$-1-1-1-1-1$	5
Y_3Y_5	$-1-1-1\ 1-1$	4	Y_4Y_5	$-1-1-1-1\ 1$	4
Y_3Z_5	$1\ 1\ 1\ 1\ 1$	0	Y_4Z_5	$1\ 1\ 1\ 1\ 1$	0
Z_3Y_5	$-1-1\ 1\ 1\ 1$	2	Z_4Y_5	$-1-1-1\ 1\ -1$	4
Z_3I_5	$1\ 1\ -1\ 1\ 1$	1	Z_4I_5	$1\ 1\ 1\ -1\ 1$	1
I_3Z_5	$1\ 1\ 1\ 1-1$	1	I_4Z_5	$1\ 1\ 1\ 1\ -1$	1
Z_3Z_5	$1\ 1\ -1\ 1-1$	2	Z_4Z_5	$1\ 1\ 1\ -1-1$	2
Total: 31/75; %41			Total: 40/75; %53		

here the different behaviors of the fidelity with respect to t_g and $\bar{n}_{\alpha,m}(0)$. This can be deduced by examining the analytical expression of the state fidelity in terms of $p(t_g, \bar{n}_{\alpha,m}(0))$, where gate time t_g, and the initial average phonon number $\bar{n}_{\alpha,m}(0)$ are the only free parameters in our simulation, the rest are fixed according to the experimental values in Ref. [38]. For simplicity, we compute an approximate state fidelity $\tilde{\mathcal{F}}_s$ for a particular example: a non-FT weight-4 X-type parity-check circuit expressed in terms of CNOT gates, resembling the one shown in Fig. 2(b), where a two-qubit dephasing channel (79) is applied after each entangling gate with error probability $p = p_{\text{deph}}$. We assume that the error probability p after each gate is the same and constant, whereas in our simulations it

TABLE V. One and two-qubit dephasing errors propagating through a non-FT X-type parity-check circuit. The subscripts on the Pauli operators refer to the qubits affected by the errors after the application of the entangling light-shift gate on those two qubits. ±1 numbers refer to the expectation of the stabilizer generators $g_1' = Z_1Z_5$, $g_2' = Z_2Z_5$, $g_3' = Z_3Z_5$, $g_4' = Z_4Z_5$, $g_5 = X_1X_2X_3X_4X_5$.

Error	Syndrome	No. of -1s	Error	Syndrome	No. of -1s
Z_1I_5	$-1\ 1\ 1\ 1\ 1$	1	Z_2I_5	$1\ -1\ 1\ 1\ 1$	1
I_1Z_5	$1\ 1\ 1\ 1-1$	1	I_2Z_5	$1\ 1\ 1\ 1\ -1$	1
Z_1Z_5	$-1\ 1\ 1\ 1-1$	2	Z_2Z_5	$1\ -1\ 1\ 1\ -1$	2
Total: 4/15; %27			Total: 4/15; %27		
Z_3I_5	$1\ 1-1\ 1\ 1$	1	Z_4I_5	$1\ 1\ 1-1\ 1$	1
I_3Z_5	$1\ 1\ 1\ 1-1$	1	I_4Z_5	$1\ 1\ 1\ 1\ -1$	1
Z_3Z_5	$1\ 1-1\ 1-1$	2	Z_4Z_5	$1\ 1\ 1-1-1$	2
Total: 4/15; %27			Total: 4/15; %27		

increases with the depth of the circuit. However, this increase is a constant heating rate, $\dot{\bar{n}}_{\alpha,m}$, so it will just add an offset with respect to the results shown in Figs. 11 and 12. Under these assumptions, the fidelity of recovering the ideal 4-qubit GHZ state on the output, $\tilde{\mathcal{F}}_s$, can be written as

$$\tilde{\mathcal{F}}_s = \sum_{k=0}^{n=4} \binom{n}{k} (1-p)^{n-k} \left(\frac{p}{3}\right)^k + \sum_{k\text{even}\,\&\,k>0}^{n=4} \binom{n}{k} \left[(1-p) + \frac{p}{3}\right]^{n-k} \left(\frac{2p}{3}\right)^k, \tag{83}$$

with $n = 4$ the number of faulty positions in the circuit, i.e., each location after a two-qubit gate. To first order, expression (83) can be approximated as

$$\tilde{\mathcal{F}}_s \approx 1 - \tfrac{11}{3}p + \cdots + O(p^4). \tag{84}$$

According to (80), the error probability, $p = p_{\text{deph}}$, varies with the microscopic error parameters, as

$$p = \tfrac{5}{8}\bar{\epsilon}_{g,T} = \tfrac{5}{8}\left[\epsilon_g^{\text{th}} + \epsilon_g^{\text{off}} + \epsilon_g^{\text{deph}} + \epsilon_g^{\text{scatt}}\right]. \tag{85}$$

Here, ϵ_g^{th}, ϵ_g^{off}, ϵ_g^{deph}, and $\epsilon_g^{\text{scatt}}$ represent the contributions of thermal error, off-resonant forces error, local dephasing, and residual photon-scattering error sources, respectively, to the gate infidelity. The exact expression for each of these contributions in terms of experimental parameters is shown in Table I and in Appendix. By fixing all the parameters apart from the gate time and the initial average number of phonons, each error contribution now becomes a function of either of these two free variables, and thus the error probability,

$$p\left(\bar{n}_{\alpha,m}(0), t_g\right) = \tfrac{5}{8}\left[\epsilon_g^{\text{th}}\left(\bar{n}_{\alpha,m}^2(0)\right) + \epsilon_g^{\text{off}}(\bar{n}_{\alpha,m}(0)) + \epsilon_g^{\text{deph}}(t_g) + \epsilon_g^{\text{scatt}}(t_g)\right]. \tag{86}$$

TABLE VI. One and two-qubit depolarizing errors propagating through a flag-based FT X-type parity-check circuit. The subscripts on the Pauli operators refer to the qubits affected by the errors after the application of the entangling light-shift gate on those two qubits. ±1 numbers refers to the expectation of the stabilizer generators $g_1 = Z_1Z_2$, $g_2 = Z_2Z_3$, $g_3 = Z_3Z_4$, $g_4 = Z_4Z_5$, $g_5 = X_1X_2X_3X_4X_5$.

Error	g_1	g_2	g_3	g_4	g_5	No. of -1s	$M_f(X)$	Error	g_1	g_2	g_3	g_4	g_5	No. of -1s	$M_f(X)$	Error	g_1	g_2	g_3	g_4	g_5	No. of -1s	$M_f(X)$
X_1I_5	-1	1	1	1	-1	2	$+1$	X_5I_6	-1	1	1	1	1	1	-1	X_2I_5	-1	-1	1	1	-1	3	$+1$
I_1X_5	-1	1	1	1	-1	2	$+1$	I_5X_6	1	1	1	1	-1	1	-1	I_2X_5	1	-1	1	1	-1	2	-1
X_1X_5	1	1	1	1	1	0	$+1$	X_5X_6	-1	1	1	1	-1	2	$+1$	X_2X_5	-1	1	1	1	1	1	-1
X_1Y_5	1	1	1	1	-1	1	$+1$	X_5Y_6	-1	1	1	1	-1	2	-1	X_2Y_5	-1	1	1	1	-1	2	-1
Y_1X_5	-1	1	1	1	1	1	$+1$	Y_5X_6	-1	1	1	1	1	1	$+1$	Y_2X_5	1	-1	1	1	1	1	-1
X_1Z_5	-1	1	1	1	1	1	$+1$	X_5Z_6	-1	1	1	1	1	1	$+1$	X_2Z_5	-1	-1	1	1	1	2	$+1$
Z_1X_5	1	1	1	1	-1	1	$+1$	Z_5X_6	1	1	1	1	1	0	-1	Z_2X_5	-1	1	1	1	-1	2	-1
Y_1I_5	1	1	1	1	-1	1	$+1$	Y_5I_6	-1	1	1	1	-1	2	-1	Y_2I_5	1	1	1	1	-1	1	$+1$
I_1Y_5	-1	1	1	1	1	1	$+1$	I_5Y_6	1	1	1	1	-1	1	$+1$	I_2Y_5	1	-1	1	1	1	1	-1
Y_1Y_5	-1	1	1	1	-1	2	$+1$	Y_5Y_6	-1	1	1	1	1	1	-1	Y_2Y_5	1	-1	1	1	-1	2	-1
Y_1Z_5	1	1	1	1	1	0	$+1$	Y_5Z_6	-1	1	1	1	-1	2	$+1$	Y_2Z_5	1	1	1	1	1	0	$+1$
Z_1Y_5	1	1	1	1	1	0	$+1$	Z_5Y_6	1	1	1	1	1	0	$+1$	Z_2Y_5	-1	1	1	1	1	1	-1
Z_1I_5	-1	1	1	1	1	1	$+1$	Z_5I_6	1	1	1	1	-1	1	$+1$	Z_2I_5	-1	-1	1	1	1	2	$+1$
I_1Z_5	1	1	1	1	-1	1	$+1$	I_5Z_6	1	1	1	1	1	0	-1	I_2Z_5	1	1	1	1	-1	1	$+1$
Z_1Z_5	-1	1	1	1	-1	2	$+1$	Z_5Z_6	1	1	1	1	-1	1	-1	Z_2Z_5	-1	-1	1	1	-1	3	$+1$
Total							16/75; %21	Total							8/75; %11	Total							12/75; %16
X_3I_5	1	-1	-1	1	-1	3	$+1$	X_5I_6	1	1	-1	1	-1	2	$+1$	X_4I_5	1	1	-1	-1	-1	3	$+1$
I_3X_5	1	1	-1	1	1	1	-1	I_5X_6	1	1	1	1	1	0	$+1$	I_4X_5	1	1	1	-1	1	1	$+1$
X_3X_5	1	-1	1	1	-1	2	-1	X_5X_6	1	1	-1	1	-1	2	$+1$	X_4X_5	1	1	-1	1	-1	2	$+1$
X_3Y_5	1	-1	1	1	1	1	-1	X_5Y_6	1	1	-1	1	-1	2	-1	X_4Y_5	1	1	-1	1	1	1	$+1$
Y_3X_5	1	1	-1	1	-1	2	-1	Y_5X_6	1	1	-1	1	1	1	$+1$	Y_4X_5	1	1	1	-1	-1	2	$+1$
X_3Z_5	1	-1	-1	1	1	2	$+1$	X_5Z_6	1	1	-1	1	-1	2	-1	X_4Z_5	1	1	-1	-1	1	2	$+1$
Z_3X_5	1	-1	1	1	1	1	-1	Z_5X_6	1	1	1	1	-1	1	$+1$	Z_4X_5	1	1	-1	1	1	1	$+1$
Y_3I_5	1	1	1	1	-1	1	$+1$	Y_5I_6	1	1	-1	1	1	1	$+1$	Y_4I_5	1	1	1	1	-1	1	$+1$
I_3Y_5	1	1	-1	1	-1	2	-1	I_5Y_6	1	1	1	1	1	0	-1	I_4Y_5	1	1	1	-1	-1	2	$+1$
Y_3Y_5	1	1	-1	1	1	1	-1	Y_5Y_6	1	1	-1	1	1	1	-1	Y_4Y_5	1	1	1	-1	1	1	$+1$
Y_3Z_5	1	1	1	1	1	0	$+1$	Y_5Z_6	1	1	-1	1	1	1	-1	Y_4Z_5	1	1	1	1	1	0	$+1$
Z_3Y_5	1	-1	1	1	-1	2	-1	Z_5Y_6	1	1	1	1	-1	1	-1	Z_4Y_5	1	1	-1	1	-1	2	$+1$
Z_3I_5	1	-1	-1	1	1	2	$+1$	Z_5I_6	1	1	1	1	-1	1	$+1$	Z_4I_5	1	1	-1	-1	1	2	$+1$
I_3Z_5	1	1	1	1	-1	1	$+1$	I_5Z_6	1	1	1	1	1	0	-1	I_4Z_5	1	1	1	1	-1	1	$+1$
Z_3Z_5	1	-1	-1	1	-1	3	$+1$	Z_5Z_6	1	1	1	1	-1	1	-1	Z_4Z_5	1	1	-1	-1	-1	3	$+1$
Total							12/75; %16	Total							8/75; %11	Total							24/75; %32

TABLE VII. One and two-qubit dephasing errors propagating through a flag-based FT X-type parity-check circuit. The subscripts on the Pauli operators refer to the qubits affected by the errors after the application of the entangling light-shift gate on those two qubits. ±1 numbers refers to the expectation of the stabilizer generators $g_1 = Z_1Z_2$, $g_2 = Z_2Z_3$, $g_3 = Z_3Z_4$, $g_4 = Z_4Z_5$, $g_5 = X_1X_2X_3X_4X_5$.

Error	g_1	g_2	g_3	g_4	g_5	No. of -1s	$M_f(X)$	Error	g_1	g_2	g_3	g_4	g_5	No. of -1s	$M_f(X)$	Error	g_1	g_2	g_3	g_4	g_5	No. of -1s	$M_f(X)$
Z_1I_5	-1	1	1	1	1	1	$+1$	Z_5I_6	1	1	1	1	-1	1	$+1$	Z_2I_5	-1	-1	1	1	1	2	$+1$
I_1Z_5	1	1	1	1	-1	1	$+1$	I_5Z_6	1	1	1	1	1	0	-1	I_2Z_5	1	1	1	1	-1	1	$+1$
Z_1Z_5	-1	1	1	1	-1	2	$+1$	Z_5Z_6	1	1	1	1	-1	1	-1	Z_2Z_5	-1	-1	1	1	-1	3	$+1$
Total							4/15; %27	Total							1/15; %6	Total							6/15; %40
Z_3I_5	1	-1	-1	1	1	2	$+1$	Z_5I_6	1	1	1	1	-1	1	$+1$	Z_4I_5	1	1	-1	-1	1	2	$+1$
I_3Z_5	1	1	1	1	-1	1	$+1$	I_5Z_6	1	1	1	1	1	0	-1	I_4Z_5	1	1	1	1	-1	1	$+1$
Z_3Z_5	1	-1	-1	1	-1	3	$+1$	Z_5Z_6	1	1	1	1	-1	1	-1	Z_4Z_5	1	1	-1	-1	-1	3	$+1$
Total							6/15; %40	Total							1/15; %6	Total							6/15; %40

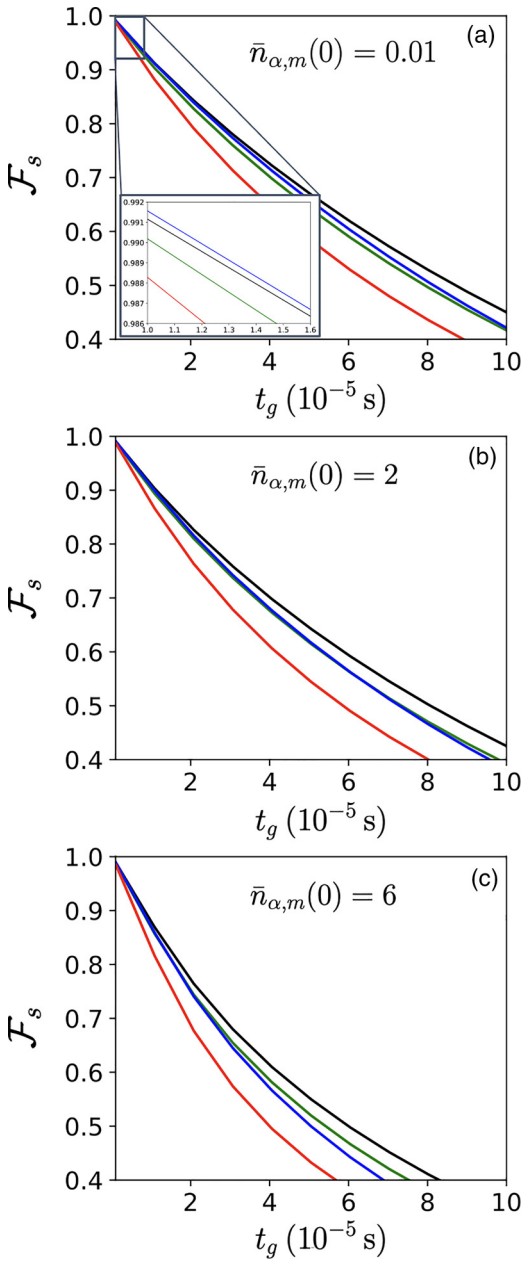

FIG. 11. Fidelity $\mathcal{F}_s$ between the output state generated by an ideal performance of the X-type circuit and the output state generated in the presence of two-qubit depolarizing and two-qubit dephasing error channels for different gate times and initial average phonon number. All modes are initially cooled down to the same $\bar{n}_{\alpha,m}(0)$. The three figures show the results for gate times t_g ranging from 1 μs up to 100 μs for different initial $\bar{n}_{\alpha,m}(0)$. Panel (a) shows the result for an initial phonon occupation number of $\bar{n}_{\alpha,m}(0) = 0.01$, on the results for the range from 1 to 1.6 μs. Panel (b) displays the results for $\bar{n}_{\alpha,m}(0) = 2$ and panel (c) does it for $\bar{n}_{\alpha,m}(0) = 6$. The black solid line represents the state fidelity in a non-FT X-type circuit run in the presence of the depolarizing channel. The blue line does the same but, for a flag-based FT circuit. The green line represents the state fidelity for the non-FT X-type parity check circuit in the presence of the dephasing channel, and the red line shows the results for the flag-based version under dephasing errors.

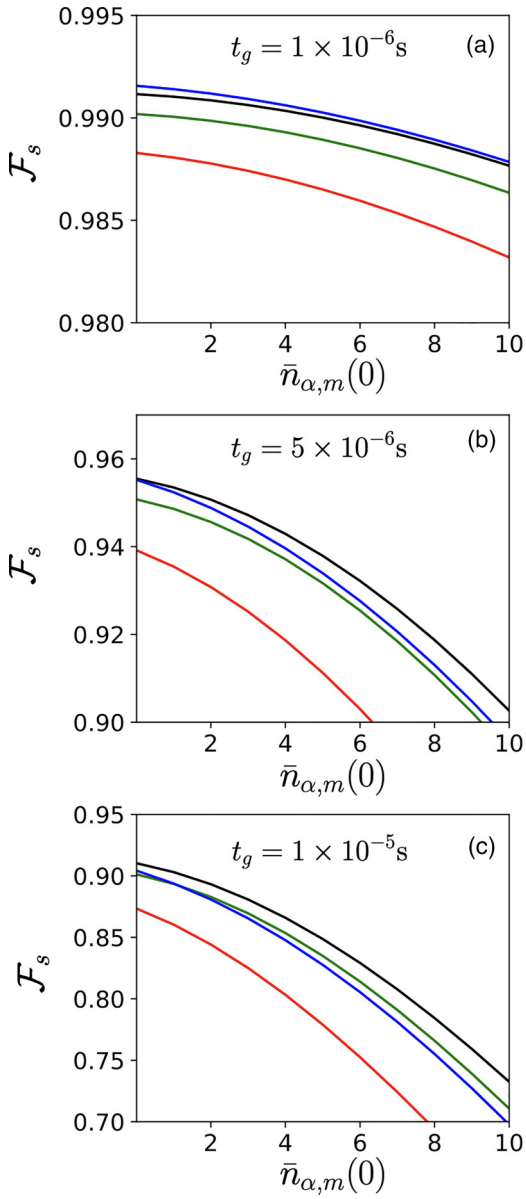

FIG. 12. Fidelity $\mathcal{F}_s$ between the output state generated by an ideal performance of the X-type circuit and the output state generated in the presence of two-qubit depolarizing and two-qubit dephasing error channels for different initial average phonon number and gate times. The three figures show the results for initial average phonon numbers $\bar{n}_{\alpha,m}(0)$ ranging from 0.01 up to 10 for different initial gate times t_g. All modes are initially cooled down to the same $\bar{n}_{\alpha,m}(0)$. Panel (a) shows the result for a gate time of $t_g = 1 \times 10^{-6}$ s, panel (b) for $t_g = 5 \times 10^{-6}$ s and panel (c) does it for $t_g = 1 \times 10^{-5}$ s. The black solid line represents the state fidelity in a non-FT X-type circuit run in the presence of the depolarizing channel. The blue line does the same but, for a flag-based FT circuit. The green line represents the state fidelity for the non-FT X-type parity check circuit in the presence of the dephasing channel, and the red line shows the results for the flag-based version under dephasing errors.

By introducing the above expression for $p(\bar{n}_{\alpha,m}(0), t_g)$ into Eq. (84), we can gain a better understanding of why in Fig. 11, the state fidelity decreases exponentially with the gate time when the initial average of phonons is fixed. For small

values of t_g, the state fidelity can be approximated by a linear decay, $\mathcal{F}_s \approx 1 - O(t_g)$. However, when we fix t_g, as seen in Fig. 12, we observe a quadratic dependence on $\bar{n}_{\alpha,m}(0)$. In this case, the state fidelity can be approximated as $\mathcal{F}_s \approx 1 - O(\bar{n}_{\alpha,m}(0)) - O(\bar{n}^2_{\alpha,m}(0))$.

Let us close this section by drawing some conclusions. We have characterized trapped-ion QEC circuits by their ability to generate multipartite entanglement. We have shown that it is important to incorporate realistic microscopic modeling of the noise to draw general conclusions about the benefits of an FT circuit design. From the perspective of GME witnessing, the added complexity of FT circuit designs is detrimental, as the region in parameter space where GME can be inferred from the measurements decreases when moving from non-FT to FT designs. Despite the fact that the postselection on the flag avoids certain weight-2 errors that are dangerous regarding the stabilizers of the QEC code, the extra gates lead to further errors that induce more sign flips of the stabilizers of the GHZ-type GME state, which is detrimental for the performance of the entanglement witness. The severity of this trend actually depends on the noise channel that is used to model errors. For the more realistic dephasing channel of trapped-ion light-shift gates, this trend is generic: the flag qubit does not help at mitigating the effects of dephasing noise on the entanglement witness for both low- and high-error probabilities. On the other hand, for a depolarizing channel, the capability of the flag-qubit FT circuit to generate GME states can actually improve for low-error rates, even if the region of witnessed GME that is characterized by larger errors does also decrease for the FT construction. From these results, it follows that one would be overestimating the power of the FT design if a depolarizing channel is used in the simulation of a trapped-ion device. On the other hand, as also discussed above, one can modify the circuits to measure other stabilizers that are more robust to a dephasing noise model. In this respect, information about the microscopic noise model can actually be used to improve the design of the QEC circuits, both with respect to the low-error regime for QEC or with respect to the GME witnessing region at higher errors.

2. *Numerics for the conditional linear witnessing*

In this section, we characterize the ability to generate GME of the X-type parity check circuits of Figs. 2 and 3 using the conditional linear witnessing method. Recall from Sec. II C 2 that this method is also efficient in the verification of ME. In contrast with the standard linear witnessing method, which uses n stabilizer generators of the n-partite systems to construct the test operators, the conditional method follows a slightly different approach. It was shown in Ref. [58] that, for the certification of ME of an n-partite system, it is sufficient to verify entanglement in just $n-1$ bipartitions. In this case, we choose to certify entanglement between the subsystems s_5 and s_x for all $s_x \in \{s_5\}^c = \{s_1, \ldots, s_4\}$ with s_5 being the syndrome qubit. This is achieved by postselecting on the state $|+\rangle\langle+|$ for the remaining $n-2=3$ qubits that are not involved in the specific bipartition. Altogether, the X-basis witness test operator in Eq. (21) can be expressed as a linear combination of two-point correlations (24), requiring three measurement basis per bipartition.

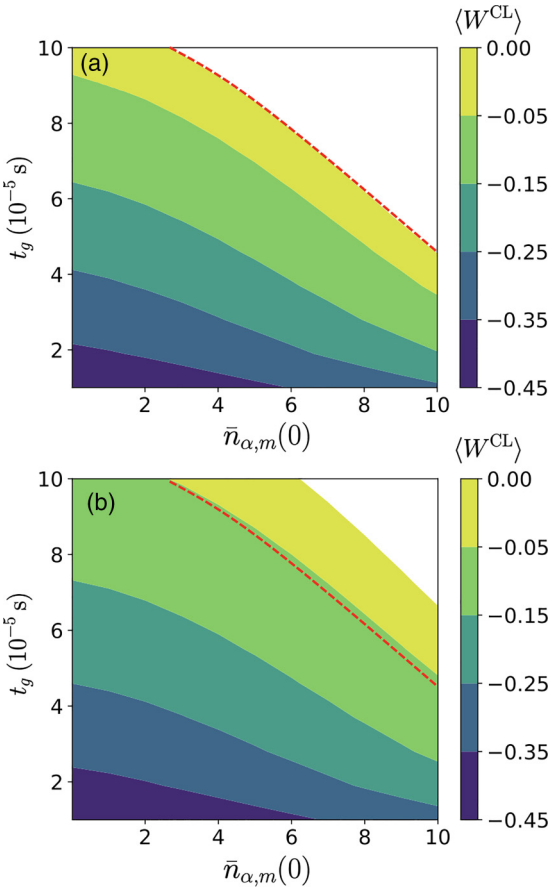

FIG. 13. CL witnessing for an X-type parity-check readout circuit. The color bar indicates the value of the witness under effective microscopic noise channels. For all the colors represented, the witness takes a negative value signaling the presence of entanglement. The white area represents all positive values of the witness values where the verification is inconclusive. The red dashed line fits the perimeter area of the (a) non-FT X-type circuit under a two-qubit depolarizing noise channel. Then, the solid line is plotted on top of the following graphs to benchmark the size of the enclosed colored area in panel (b), the non-FT X-type circuits under dephasing noise, respectively. This witness is reconstructed using the products of the Bell-pair stabilizer generators for the $[s_5|s_1]$ bipartition output state $(|00\rangle + |11\rangle)/\sqrt{2}$ which are $g_1 = X_1X_5$, $g_2 = Z_1Z_5$. The resulting Bell pair is obtained after postselecting on $|+\rangle\langle+|^{\otimes 3}$ for s_2, s_3, and s_4 subsystem qubits.

Figures 13(a) and 13(b) show the numerical simulations for the non-FT circuit in the presence of the effective two-qubit depolarizing and dephasing channels, respectively. We only display the values of the CL witness for the bipartition $[s_5|s_1]$, which actually has the lowest performance under the noise channels in comparison to the other bipartitions. The red dashed line is the boundary between the entanglement witnesses region and the inconclusive outer region for the depolarizing channel. This line is then plotted on top of the results for the dephasing channel for comparison, as shown in Fig. 13(b). We note that the conditioned ME witnessed region is greater when the effective noise channel is a dephasing channel than when it is a depolarizing channel. However, this may not be the case for other bipartitions.

In fact, for the rest of the bipartitions, which we do not show here to avoid redundancy, the region of witnessed entanglement in the presence of dephasing noise barely changes its size, while the depolarizing area increases. For the bipartition $[s_5|s_4]$, the witnessed entanglement area, in the presence of depolarizing noise, surpasses the one obtained under the dephasing channel. The majority of the depolarizing errors with a Pauli-operator of the type X_5 or Y_5, occurring on the syndrome, propagate to multiple errors through the light-shift gates, and consequently, it is more likely to find errors that have propagated on s_3, s_4, and s_5. This implies that the Bell pair generators with support in these subsystem qubits commute more times with the propagated errors, yielding better results for the witnessed entanglement regions.

The main conclusion that can be drawn from the results from Figs. 7 and 13 is that, for both types of noise channels, the conditional linear witness encloses a larger area of witnessed entanglement than the one obtained via the standard linear witness. For brevity, in Fig. 13 we do not show the results for the CL method using the flag-based FT circuit, as the behavior is the same as we extensively discussed in Sec. IV 1. For the high probability error rates needed to show the performance of the witnesses, the flag-based circuits would always add more noise and perform worse than the bare non-FT circuits.

V. CONCLUSIONS AND OUTLOOK

In this paper, we have presented a detailed microscopic error model for the trapped-ion light-shift gates in terms of the average gate error. We have discussed a microscopic derivation of this error in terms of entanglement fidelity, which can be condensed into an analytical formula that contains various possible error sources and experimental parameters. We then fed this gate error into effective noise models for the two-qubit light shift gates. In this way, the dynamical quantum map that describes the evolution of the imperfect entangling gate has error rates that connect to realistic microscopic calculations, instead of giving them arbitrary values from zero to one, as we had previously done in Ref. [58].

We have used this noise model to assess the performance of the parity-check QEC circuits in terms of their ability to generate n-qubit entangled output states. Multipartite entanglement, then, is detected by two entanglement witnessing operators, which require a number of bipartitions in which entanglement must be checked that grows linearly with the qubit register size. These methods correspond to the standard linear (SL) method used experimentally in this context in Ref. [38], and the conditional linear (CL) method that we introduced in Ref. [58]. We verify that the CL method is again more robust than the standard linear method for the current, more realistic, noise model. In spite of this improvement, it should be noted that the CL witness can lead to an increase in statistical errors due to the conditional evaluation or postselection of the remaining subsystems. Besides, the CL needs twelve measurement settings, while the SL only needs two, so that, in order to choose one method with respect to the other, one must first evaluate the trade-off between robustness and experimental feasibility.

Regarding the flag-based FT results, we have shown that for high failure rates on the two-qubit entangling gates, the flag-qubit does not have a positive effect on the GME witnessed certification. We have argued that the two additional entangling gates between syndrome and flag qubit designed to catch weight-2 dangerous errors, introduce additional errors which, at high failure rates, are not eliminated after postselecting on the flag, and lead to more sign flips of the stabilizers that reduce the expectation value of the witness operator.

An interesting direction for further research could be to work on the design of optimal SL witnesses by a thorough analysis of the particular output state generated by the QEC primitives, and the propagation of the effective noise channel through it. We have shown in the text that, by changing the stabilizer generators for the SL method, the region of witnessed GME can be greater for the biased dephasing noise. Therefore, if one knows the noise structure, and how the propagation through the circuit affects the resulting witness test operators, it is possible to optimize the design of entanglement witnesses to choose the most robust option. We believe that our work can also help experimentalists working with these gates to realize which experimental parameters can be modified to minimize the two-qubit gate infidelity values in their setups.

ACKNOWLEDGMENTS

We acknowledge support from PID2021-127726NB-I00 (MCIU/AEI/FEDER, UE), from the Grant IFT Centro de Excelencia Severo Ochoa CEX2020-001007-S, funded by MCIN/AEI/10.13039/501100011033, from the grant QUITEMAD+ S2013/ICE-2801, and from the CSIC Research Platform on Quantum Technologies PTI-001. A.R.B. acknowledges support from the Universidad Complutense de Madrid-Banco Santander Predoctoral Fellowship. A.R.B. also thanks J.G.F.U for providing access to computing capabilities to carry out numerical simulations. F.S. acknowledges the Research Fellowship by the Royal Commission for the Exhibition of 1851. A.B. acknowledges support from the EU Quantum Technology Flagship grant AQTION under Grant Agreement No. 820495, and by the US Army Research Office through Grant No. W911NF-21-1-0007. The project leading to this application/publication has received funding from the European Union's Horizon Europe research and innovation programme under Grant Agreement No. 101114305 ("MILLENION-SGA1" EU Project).

APPENDIX: DETAILED ANALYTICAL FORMULAS FOR THE GATE INFIDELITY CAUSED BY THERMAL ERRORS

To highlight the quadratic dependence of the thermal error on the average phonon number, this Appendix presents more explicit expressions for the analytical formulas derived for the thermal error contributions, as shown in Table I. We cover both warm active and spectator phonons.

1. Gate infidelity due to warm active phonons

By expanding the covariance in Eq. (49), we obtain the expression for the gate infidelity due to warm active phonons:

$$\epsilon_{\rm th}^{\rm act} = \left(\frac{\pi\eta_{x,1}^2}{4}\right)^2 \left\{ 2\bar{n}_{x,1}^2 + \bar{n}_{x,1} + 2\left(\frac{\omega_{x,1}}{\omega_{x,2}}\right)\bar{n}_{x,1}\bar{n}_{x,2} + \left(\frac{\omega_{x,1}}{\omega_{x,2}}\right)^2 \left(2\bar{n}_{x,2}^2 + \bar{n}_{x,2}\right) \right\}. \tag{A1}$$

$\bar{n}_{x,1} \equiv \bar{n}_{x,1}(0)$ and $\bar{n}_{x,2} \equiv \bar{n}_{x,2}(0)$ represent the initial average phonon number for the both radial modes along the x axis. Recall that for the simulations, the two-ion light-shift gates are mediated by the radial phonons along this axis, referred to as the active modes. $\omega_{x,m}$ and $\eta_{x,m}$ with $m = \{1, 2\}$ are the mode frequencies and the Lamb-Dicke parameters for the two-ion crystal in the x radial direction, respectively.

2. Gate infidelity due to warm spectator phonons

Following a similar procedure as above, and expanding the covariance in Eq. (54), we obtain the expression for the gate infidelity due to warm spectator phonons

$$\begin{aligned}
\epsilon_{\rm th}^{\rm spec} = \frac{1}{4}\Bigg[& \left(\frac{\pi\eta_{y,1}^2}{4}\right)^2 \left\{ 2\bar{n}_{y,1}^2 + \bar{n}_{y,1} + 2\left(\frac{\omega_{y,1}}{\omega_{y,2}}\right)\bar{n}_{y,1}\bar{n}_{y,2} + \left(\frac{\omega_{y,1}}{\omega_{y,2}}\right)^2 \left(2\bar{n}_{y,2}^2 + \bar{n}_{y,2}\right) \right\} \\
& + \left(\frac{\pi\eta_{z,1}^2}{4}\right)^2 \left\{ 2\bar{n}_{z,1}^2 + \bar{n}_{z,1} + 2\left(\frac{\omega_{z,1}}{\omega_{z,2}}\right)\bar{n}_{z,1}\bar{n}_{z,2} + \left(\frac{\omega_{z,1}}{\omega_{z,2}}\right)^2 \left(2\bar{n}_{z,2}^2 + \bar{n}_{z,2}\right) \right\} \Bigg] \\
& - \bar{n}_{x,1}\left(\frac{\pi\eta_{x,1}^2\omega_{x,1}}{4}\right)^2 \left[\frac{\bar{n}_{y,1}}{\omega_{y,1}^2} + \frac{\bar{n}_{z,1}}{\omega_{z,1}^2} + \frac{\bar{n}_{y,2}}{\omega_{y,2}^2} + \frac{\bar{n}_{z,2}}{\omega_{z,2}^2} \right] - \bar{n}_{x,2}\left(\frac{\pi\eta_{x,2}^2\omega_{x,2}}{4}\right)^2 \left[\frac{\bar{n}_{y,1}}{\omega_{y,1}^2} + \frac{\bar{n}_{z,1}}{\omega_{z,1}^2} + \frac{\bar{n}_{y,2}}{\omega_{y,2}^2} + \frac{\bar{n}_{z,2}}{\omega_{z,2}^2} \right] \\
& - \frac{1}{2}\left(\frac{\pi}{4}\right)^2 \left[\bar{n}_{y,1}\omega_{y,1}\eta_{y,1}^4 + \bar{n}_{y,2}\omega_{y,2}\eta_{y,2}^4 \right] \left[\frac{\bar{n}_{z,1}}{\omega_{z,1}} - \frac{\bar{n}_{z,2}}{\omega_{z,2}} \right].
\end{aligned} \tag{A2}$$

Here, $\bar{n}_{y,m} \equiv \bar{n}_{y,m}(0)$ represents the average number of phonons for the $m = \{1, 2\}$ modes along the y axis, and $\bar{n}_{z,m} \equiv \bar{n}_{z,m}(0)$ represent the average number of phonons for the modes $m = \{1, 2\}$ along the z axis. We refer to these modes as spectator modes, which in an ideal scenario are not involved in the entangling operation. The mode frequencies and the Lamb-Dicke parameters for the spectator modes are given by $\omega_{\alpha,m}$ and $\eta_{\alpha,m}$, respectively, with $\alpha = y, z$ and $m = \{1, 2\}$.

[1] M. A. Nielsen and I. L. Chuang, *Quantum Computation and Quantum Information* (Cambridge University Press, Cambridge, 2000).

[2] A. Montanaro, Quantum algorithms: An overview, npj Quantum Inf. **2**, 15023 (2016).

[3] T. D. Ladd, F. Jelezko, R. Laflamme, Y. Nakamura, C. Monroe, and J. L. O'Brien, Quantum computers, Nature (London) **464**, 45 (2010).

[4] J. Preskill, Quantum computing in the NISQ era and beyond, Quantum **2**, 79 (2018).

[5] F. Arute *et al.*, Quantum supremacy using a programmable superconducting processor, Nature (London) **574**, 505 (2019).

[6] H.-S. Zhong, H. Wang, Y.-H. Deng, M.-C. Chen, L.-C. Peng, Y.-H. Luo, J. Qin, D. Wu, X. Ding, Y. Hu, P. Hu, X.-Y. Yang, W.-J. Zhang, H. Li, Y. Li, X. Jiang, L. Gan, G. Yang, L. You, Z. Wang *et al.*, Quantum computational advantage using photons, Science **370**, 1460 (2020).

[7] A. R. Calderbank and P. W. Shor, Good quantum error-correcting codes exist, Phys. Rev. A **54**, 1098 (1996).

[8] A. M. Steane, Error correcting codes in quantum theory, Phys. Rev. Lett. **77**, 793 (1996).

[9] B. M. Terhal, Quantum error correction for quantum memories, Rev. Mod. Phys. **87**, 307 (2015).

[10] D. Aharonov and M. Ben-Or, Fault-tolerant quantum computation with constant error, SIAM J. Comput. **38**, 1207 (2008).

[11] K. M. Svore, A. W. Cross, I. L. Chuang, and A. V. Aho, A flow-map model for analyzing pseudothresholds in fault-tolerant quantum computing, Quantum Inf. Comput. **6**, 193 (2006).

[12] A. W. Cross, D. P. DiVincenzo, and B. M. Terhal, A comparative code study for quantum fault-tolerance, Quantum Inf. Comput. **9**, 0541 (2009).

[13] C. D. Bruzewicz, J. Chiaverini, R. McConnell, and J. M. Sage, Trapped-ion quantum computing: Progress and challenges, Appl. Phys. Rev. **6**, 021314 (2019).

[14] T. P. Harty, D. T. C. Allcock, C. J. Ballance, L. Guidoni, H. A. Janacek, N. M. Linke, D. N. Stacey, and D. M. Lucas, High-fidelity preparation, gates, memory, and readout of a trapped-ion quantum bit, Phys. Rev. Lett. **113**, 220501 (2014).

[15] T. Ruster, C. T. Schmiegelow, H. Kaufmann, C. Warschburger, F. Schmidt-Kaler, and U. G. Poschinger, A long-lived Zeeman trapped-ion qubit, Appl. Phys. B: Lasers Opt. **122**, 254 (2016).

[16] A. Keselman, Y. Glickman, N. Akerman, S. Kotler, and R. Ozeri, High-fidelity state detection and tomography of a single-ion Zeeman qubit, New J. Phys. **13**, 073027 (2011).

[17] J. Emerson, R. Alicki, and K. Życzkowski, Scalable noise estimation with random unitary operators, J. Opt. B: Quantum Semiclassical Opt. **7**, S347 (2005).

[18] T. Monz, D. Nigg, E. A. Martinez, M. F. Brandl, P. Schindler, R. Rines, S. X. Wang, I. L. Chuang, and R. Blatt, Realization of a scalable Shor algorithm, Science **351**, 1068 (2016).

[19] C. Hempel, C. Maier, J. Romero, J. McClean, T. Monz, H. Shen, P. Jurcevic, B. P. Lanyon, P. Love, R. Babbush, A. Aspuru-Guzik, R. Blatt, and C. F. Roos, Quantum chemistry calculations on a trapped-ion quantum simulator, Phys. Rev. X **8**, 031022 (2018).

[20] C. Sanz-Fernandez, R. Hernandez, C. D. Marciniak, I. Pogorelov, T. Monz, F. Benfenati, S. Mugel, and R. Orus, Quantum portfolio value forecasting, arXiv:2111.14970.

[21] K. Mølmer and A. Sørensen, Multiparticle entanglement of hot trapped ions, Phys. Rev. Lett. **82**, 1835 (1999).

[22] A. Sørensen and K. Mølmer, Entanglement and quantum computation with ions in thermal motion, Phys. Rev. A **62**, 022311 (2000).

[23] J. P. Gaebler, T. R. Tan, Y. Lin, Y. Wan, R. Bowler, A. C. Keith, S. Glancy, K. Coakley, E. Knill, D. Leibfried, and D. J. Wineland, High-fidelity universal gate set for $^{9+}$Be ion qubits, Phys. Rev. Lett. **117**, 060505 (2016).

[24] A. Erhard, J. J. Wallman, L. Postler, M. Meth, R. Stricker, E. A. Martinez, P. Schindler, T. Monz, J. Emerson, and R. Blatt, Characterizing large-scale quantum computers via cycle benchmarking, Nat. Commun. **10**, 5347 (2019).

[25] A. Bermudez, P. O. Schmidt, M. B. Plenio, and A. Retzker, Robust trapped-ion quantum logic gates by continuous dynamical decoupling, Phys. Rev. A **85**, 040302 (2012).

[26] A. Lemmer, A. Bermudez, and M. B. Plenio, Driven geometric phase gates with trapped ions, New J. Phys. **15**, 083001 (2013).

[27] T. R. Tan, J. P. Gaebler, R. Bowler, Y. Lin, J. D. Jost, D. Leibfried, and D. J. Wineland, Demonstration of a dressed-state phase gate for trapped ions, Phys. Rev. Lett. **110**, 263002 (2013).

[28] T. P. Harty, M. A. Sepiol, D. T. C. Allcock, C. J. Ballance, J. E. Tarlton, and D. M. Lucas, High-fidelity trapped-ion quantum logic using near-field microwaves, Phys. Rev. Lett. **117**, 140501 (2016).

[29] D. Leibfried, B. DeMarco, V. Meyer, D. Lucas, M. Barrett, J. Britton, W. M. Itano, B. Jelenkovic, C. Langer, T. Rosenband, and D. J. Wineland, Experimental demonstration of a robust, high-fidelity geometric two ion-qubit phase gate, Nature (London) **422**, 412 (2003).

[30] C. J. Ballance, T. P. Harty, N. M. Linke, M. A. Sepiol, and D. M. Lucas, High-fidelity quantum logic gates using trapped-ion hyperfine qubits, Phys. Rev. Lett. **117**, 060504 (2016).

[31] C. H. Baldwin, B. J. Bjork, M. Foss-Feig, J. P. Gaebler, D. Hayes, M. G. Kokish, C. Langer, J. A. Sedlacek, D. Stack, and G. Vittorini, High-fidelity light-shift gate for clock-state qubits, Phys. Rev. A **103**, 012603 (2021).

[32] D. Kielpinski, C. Monroe, and D. J. Wineland, Architecture for a large-scale ion-trap quantum computer, Nature (London) **417**, 709 (2002).

[33] V. Kaushal, B. Lekitsch, A. Stahl, J. Hilder, D. Pijn, C. Schmiegelow, A. Bermudez, M. Müller, F. Schmidt-Kaler, and U. Poschinger, Shuttling-based trapped-ion quantum information processing, AVS Quantum Sci. **2**, 014101 (2020).

[34] J. P. Home, D. Hanneke, J. D. Jost, J. M. Amini, D. Leibfried, and D. J. Wineland, Complete methods set for scalable ion trap quantum information processing, Science **325**, 1227 (2009).

[35] H. Kaufmann, T. Ruster, C. T. Schmiegelow, M. A. Luda, V. Kaushal, J. Schulz, D. von Lindenfels, F. Schmidt-Kaler, and U. G. Poschinger, Scalable creation of long-lived multipartite entanglement, Phys. Rev. Lett. **119**, 150503 (2017).

[36] J. M. Pino *et al.*, Demonstration of the trapped-ion quantum CCD computer architecture, Nature (London) **592**, 209 (2021).

[37] C. Ryan-Anderson, J. G. Bohnet, K. Lee, D. Gresh, A. Hankin, J. P. Gaebler, D. Francois, A. Chernoguzov, D. Lucchetti, N. C. Brown, T. M. Gatterman, S. K. Halit, K. Gilmore, J. A. Gerber, B. Neyenhuis, D. Hayes, and R. P. Stutz, Realization of real-time fault-tolerant quantum error correction, Phys. Rev. X **11**, 041058 (2021).

[38] J. Hilder, D. Pijn, O. Onishchenko, A. Stahl, M. Orth, B. Lekitsch, A. Rodriguez-Blanco, M. Müller, F. Schmidt-Kaler, and U. G. Poschinger, Fault-tolerant parity readout on a shuttling-based trapped-ion quantum computer, Phys. Rev. X **12**, 011032 (2022).

[39] S. Debnath, N. M. Linke, C. Figgatt, K. A. Landsman, K. Wright, and C. Monroe, Demonstration of a small programmable quantum computer with atomic qubits, Nature (London) **536**, 63 (2016).

[40] C. Figgatt, A. Ostrander, N. M. Linke, K. A. Landsman, D. Zhu, D. Maslov, and C. Monroe, Parallel entangling operations on a universal ion-trap quantum computer, Nature (London) **572**, 368 (2019).

[41] I. Pogorelov, T. Feldker, C. D. Marciniak, L. Postler, G. Jacob, O. Krieglsteiner, V. Podlesnic, M. Meth, V. Negnevitsky, M. Stadler, B. Höfer, C. Wächter, K. Lakhmanskiy, R. Blatt, P. Schindler, and T. Monz, Compact ion-trap quantum computing demonstrator, PRX Quantum **2**, 020343 (2021).

[42] A. Bermudez *et al.*, Assessing the progress of trapped-ion processors towards fault-tolerant quantum computation, Phys. Rev. X **7**, 041061 (2017).

[43] M. Gutiérrez, M. Müller, and A. Bermúdez, Transversality and lattice surgery: Exploring realistic routes toward coupled logical qubits with trapped-ion quantum processors, Phys. Rev. A **99**, 022330 (2019).

[44] A. Bermudez, X. Xu, M. Gutiérrez, S. C. Benjamin, and M. Müller, Fault-tolerant protection of near-term trapped-ion topological qubits under realistic noise sources, Phys. Rev. A **100**, 062307 (2019).

[45] P. Parrado-Rodríguez, C. Ryan-Anderson, A. Bermudez, and M. Müller, Crosstalk suppression for fault-tolerant quantum error correction with trapped ions, Quantum **5**, 487 (2021).

[46] C. J. Trout, M. Li, M. Gutiérrez, Y. Wu, S.-T. Wang, L. Duan, and K. R. Brown, Simulating the performance of a distance-3 surface code in a linear ion trap, New J. Phys. **20**, 043038 (2018).

[47] D. M. Debroy, M. Li, S. Huang, and K. R. Brown, Logical performance of 9 qubit compass codes in ion traps with crosstalk errors, Quantum Sci. Technol. **5**, 034002 (2020).

[48] P. Murali, D. M. Debroy, K. R. Brown, and M. Martonosi, Architecting noisy intermediate-scale trapped ion quantum computers, arXiv:2004.04706.

[49] X.-C. Wu, D. M. Debroy, Y. Ding, J. M. Baker, Y. Alexeev, K. R. Brown, and F. T. Chong, in *2021 IEEE International Symposium on High-Performance Computer Architecture (HPCA)* (IEEE Computer Society, Los Alamitos, CA, 2021), pp. 153–166.

[50] H. N. Tinkey, A. M. Meier, C. R. Clark, C. M. Seck, and K. R. Brown, Quantum process tomography of a Mølmer-Sørensen gate via a global beam, Quantum Sci. Technol. **6**, 034013 (2021).

[51] P. Schindler *et al.*, A quantum information processor with trapped ions, New J. Phys. **15**, 123012 (2013).

[52] C. Ballance, High-fidelity quantum logic in Ca^+, Ph.D. thesis, University of Oxford, 2017.

[53] R. T. Sutherland, Q. Yu, K. M. Beck, and H. Häffner, One- and two-qubit gate infidelities due to motional errors in trapped ions and electrons, Phys. Rev. A **105**, 022437 (2022).

[54] J. Preskill, *Lecture notes for Physics 219: Quantum Computation* (California Institute of Technology, Pasadena, 1998).

[55] C. H. Bennett, D. P. DiVincenzo, J. A. Smolin, and W. K. Wootters, Mixed-state entanglement and quantum error correction, Phys. Rev. A **54**, 3824 (1996).

[56] D. A. Lidar and T. A. Brun, *Quantum Error Correction* (Cambridge University Press, United Kingdom, 2013).

[57] A. Almheiri, X. Dong, and D. Harlow, Bulk locality and quantum error correction in ADS/CFT, J. High Energy Phys. 04 (2015) 163.

[58] A. Rodriguez-Blanco, A. Bermudez, M. Müller, and F. Shahandeh, Efficient and robust certification of genuine multipartite entanglement in noisy quantum error correction circuits, PRX Quantum **2**, 020304 (2021).

[59] D. Gottesman, Stabilizer codes and quantum error correction, arXiv:quant-ph/9705052.

[60] J. Chiaverini, D. Leibfried, T. Schaetz, M. D. Barrett, R. B. Blakestad, J. Britton, W. M. Itano, J. D. Jost, E. Knill, C. Langer, R. Ozeri, and D. J. Wineland, Realization of quantum error correction, Nature (London) **432**, 602 (2004).

[61] P. Schindler, J. T. Barreiro, T. Monz, V. Nebendahl, D. Nigg, M. Chwalla, M. Hennrich, and R. Blatt, Experimental repetitive quantum error correction, Science **332**, 1059 (2011).

[62] D. Nigg, M. Müller, E. A. Martinez, P. Schindler, M. Hennrich, T. Monz, M. A. Martin-Delgado, and R. Blatt, Quantum computations on a topologically encoded qubit, Science **345**, 302 (2014).

[63] N. M. Linke *et al.*, Fault-tolerant quantum error detection, Sci. Adv. **3**, e1701074 (2017).

[64] R. Stricker, D. Vodola, A. Erhard, L. Postler, M. Meth, M. Ringbauer, P. Schindler, T. Monz, M. Müller, and R. Blatt, Experimental deterministic correction of qubit loss, Nature (London) **585**, 207 (2020).

[65] A. Erhard *et al.*, Entangling logical qubits with lattice surgery, Nature (London) **589**, 220 (2021).

[66] L. Egan, D. M. Debroy, C. Noel, A. Risinger, D. Zhu, D. Biswas, M. Newman, M. Li, K. R. Brown, M. Cetina, and C. Monroe, Fault-tolerant control of an error-corrected qubit, Nature (London) **598**, 281 (2021).

[67] D. M. Debroy, L. Egan, C. Noel, A. Risinger, D. Zhu, D. Biswas, M. Cetina, C. Monroe, and K. R. Brown, Optimizing stabilizer parities for improved logical qubit memories, Phys. Rev. Lett. **127**, 240501 (2021).

[68] L. Postler, S. Heußen, I. Pogorelov, M. Rispler, T. Feldker, M. Meth, C. D. Marciniak, R. Stricker, M. Ringbauer, R. Blatt, P. Schindler, M. Müller, and T. Monz, Demonstration of fault-tolerant universal quantum gate operations, Nature (London) **605**, 675 (2022).

[69] C. Ryan-Anderson, N. C. Brown, M. S. Allman, B. Arkin, G. Asa-Attuah, C. Baldwin, J. Berg, J. G. Bohnet, S. Braxton, N. Burdick, J. P. Campora, A. Chernoguzov, J. Esposito, B. Evans, D. Francois, J. P. Gaebler, T. M. Gatterman, J. Gerber, K. Gilmore, D. Gresh *et al.*, Implementing fault-tolerant entangling gates on the five-qubit code and the color code, arXiv:2208.01863.

[70] H. Bombin and M. A. Martin-Delgado, Topological quantum distillation, Phys. Rev. Lett. **97**, 180501 (2006).

[71] R. Chao and B. W. Reichardt, Quantum error correction with only two extra qubits, Phys. Rev. Lett. **121**, 050502 (2018).

[72] C. Chamberland and M. E. Beverland, Flag fault-tolerant error correction with arbitrary distance codes, Quantum **2**, 53 (2018).

[73] R. Chao and B. W. Reichardt, Flag fault-tolerant error correction for any stabilizer code, PRX Quantum **1**, 010302 (2020).

[74] A. Steane, Multiple-particle interference and quantum error correction, Proc. R. Soc. London, Ser. A **452**, 2551 (1996).

[75] C. A. Sackett, D. Kielpinski, B. E. King, C. Langer, V. Meyer, C. J. Myatt, M. Rowe, Q. A. Turchette, W. M. Itano, D. J. Wineland, and C. Monroe, Experimental entanglement of four particles, Nature (London) **404**, 256 (2000).

[76] J. Benhelm, G. Kirchmair, C. F. Roos, and R. Blatt, Towards fault-tolerant quantum computing with trapped ions, Nat. Phys. **4**, 463 (2008).

[77] U. G. Poschinger, G. Huber, F. Ziesel, M. Deiß, M. Hettrich, S. A. Schulz, K. Singer, G. Poulsen, M. Drewsen, R. J. Hendricks, and F. Schmidt-Kaler, Coherent manipulation of a $^{40}Ca^+$ spin qubit in a micro ion trap, J. Phys. B: At., Mol. Opt. Phys. **42**, 154013 (2009).

[78] D. Leibfried, R. Blatt, C. Monroe, and D. Wineland, Quantum dynamics of single trapped ions, Rev. Mod. Phys. **75**, 281 (2003).

[79] V. Nebendahl, H. Häffner, and C. F. Roos, Optimal control of entangling operations for trapped-ion quantum computing, Phys. Rev. A **79**, 012312 (2009).

[80] F. Schmidt-Kaler, H. Häffner, M. Riebe, S. Gulde, G. P. T. Lancaster, T. Deuschle, C. Becher, C. F. Roos, J. Eschner, and R. Blatt, Realization of the Cirac-Zoller controlled-not quantum gate, Nature (London) **422**, 408 (2003).

[81] D. P. DiVincenzo and P. W. Shor, Fault-tolerant error correction with efficient quantum codes, Phys. Rev. Lett. **77**, 3260 (1996).

[82] D. P. DiVincenzo and P. Aliferis, Effective fault-tolerant quantum computation with slow measurements, Phys. Rev. Lett. **98**, 020501 (2007).

[83] C. Chamberland and A. W. Cross, Fault-tolerant magic state preparation with flag qubits, Quantum **3**, 143 (2019).

[84] B. W. Reichardt, Fault-tolerant quantum error correction for Steane's seven-qubit color code with few or no extra qubits, Quantum Sci. Technol. **6**, 015007 (2021).

[85] T. Tansuwannont, C. Chamberland, and D. Leung, Flag fault-tolerant error correction, measurement, and quantum

computation for cyclic Calderbank-Shor-Steane codes, Phys. Rev. A **101**, 012342 (2020).
[86] C. Chamberland, A. Kubica, T. J. Yoder, and G. Zhu, Triangular color codes on trivalent graphs with flag qubits, New J. Phys. **22**, 023019 (2020).
[87] M. Horodecki, P. Horodecki, and R. Horodecki, Separability of mixed states: Necessary and sufficient conditions, Phys. Lett. A **223**, 1 (1996).
[88] B. M. Terhal, Bell inequalities and the separability criterion, Phys. Lett. A **271**, 319 (2000).
[89] M. Lewenstein, B. Kraus, J. I. Cirac, and P. Horodecki, Optimization of entanglement witnesses, Phys. Rev. A **62**, 052310 (2000).
[90] J. Sperling and W. Vogel, Multipartite entanglement witnesses, Phys. Rev. Lett. **111**, 110503 (2013).
[91] R. Horodecki, P. Horodecki, M. Horodecki, and K. Horodecki, Quantum entanglement, Rev. Mod. Phys. **81**, 865 (2009).
[92] G. Tóth and O. Gühne, Entanglement detection in the stabilizer formalism, Phys. Rev. A **72**, 022340 (2005).
[93] G. Tóth and O. Gühne, Detecting genuine multipartite entanglement with two local measurements, Phys. Rev. Lett. **94**, 060501 (2005).
[94] R. F. Werner, Quantum states with Einstein-Podolsky-Rosen correlations admitting a hidden-variable model, Phys. Rev. A **40**, 4277 (1989).
[95] S. J. Devitt, W. J. Munro, and K. Nemoto, Quantum error correction for beginners, Rep. Prog. Phys. **76**, 076001 (2013).
[96] O. Gühne and G. Tóth, Entanglement detection, Phys. Rep. **474**, 1 (2009).
[97] M. Huber, F. Mintert, A. Gabriel, and B. C. Hiesmayr, Detection of high-dimensional genuine multipartite entanglement of mixed states, Phys. Rev. Lett. **104**, 210501 (2010).
[98] F. Verstraete, M. Popp, and J. I. Cirac, Entanglement versus correlations in spin systems, Phys. Rev. Lett. **92**, 027901 (2004).
[99] M. Popp, F. Verstraete, M. A. Martín-Delgado, and J. I. Cirac, Localizable entanglement, Phys. Rev. A **71**, 042306 (2005).
[100] D. F. V. James, Quantum dynamics of cold trapped ions with application to quantum computation, Appl. Phys. B: Lasers Opt. **66**, 181 (1998).
[101] A. Bermudez, P. Schindler, T. Monz, R. Blatt, and M. Müller, Micromotion-enabled improvement of quantum logic gates with trapped ions, New J. Phys. **19**, 113038 (2017).
[102] W. Magnus, On the exponential solution of differential equations for a linear operator, Commun. Pure Appl. Math. **7**, 649 (1954).
[103] S. Blanes, F. Casas, J. A. Oteo, and J. Ros, A pedagogical approach to the magnus expansion, Eur. J. Phys. **31**, 907 (2010).
[104] D. Porras and J. I. Cirac, Effective quantum spin systems with trapped ions, Phys. Rev. Lett. **92**, 207901 (2004).
[105] S.-L. Zhu, C. Monroe, and L.-M. Duan, Trapped ion quantum computation with transverse phonon modes, Phys. Rev. Lett. **97**, 050505 (2006).
[106] G.-D. Lin, S.-L. Zhu, R. Islam, K. Kim, M.-S. Chang, S. Korenblit, C. Monroe, and L.-M. Duan, Large-scale quantum computation in an anharmonic linear ion trap, Europhys. Lett. **86**, 60004 (2009).
[107] K. A. Brickman Soderberg and C. Monroe, Phonon-mediated entanglement for trapped ion quantum computing, Rep. Prog. Phys. **73**, 036401 (2010).
[108] B. Schumacher, Sending entanglement through noisy quantum channels, Phys. Rev. A **54**, 2614 (1996).
[109] M. Horodecki, P. Horodecki, and R. Horodecki, General teleportation channel, singlet fraction, and quasidistillation, Phys. Rev. A **60**, 1888 (1999).
[110] M. A. Nielsen, A simple formula for the average gate fidelity of a quantum dynamical operation, Phys. Lett. A **303**, 249 (2002).
[111] K. Kim, M.-S. Chang, R. Islam, S. Korenblit, L.-M. Duan, and C. Monroe, Entanglement and tunable spin-spin couplings between trapped ions using multiple transverse modes, Phys. Rev. Lett. **103**, 120502 (2009).
[112] F. Reiter and A. S. Sørensen, Effective operator formalism for open quantum systems, Phys. Rev. A **85**, 032111 (2012).
[113] A. Bermudez, J. Almeida, K. Ott, H. Kaufmann, S. Ulm, U. Poschinger, F. Schmidt-Kaler, A. Retzker, and M. B. Plenio, Quantum magnetism of spin-ladder compounds with trapped-ion crystals, New J. Phys. **14**, 093042 (2012).
[114] R. Ozeri, C. Langer, J. D. Jost, B. DeMarco, A. Ben-Kish, B. R. Blakestad, J. Britton, J. Chiaverini, W. M. Itano, D. B. Hume, D. Leibfried, T. Rosenband, P. O. Schmidt, and D. J. Wineland, Hyperfine coherence in the presence of spontaneous photon scattering, Phys. Rev. Lett. **95**, 030403 (2005).
[115] H. Uys, M. J. Biercuk, A. P. VanDevender, C. Ospelkaus, D. Meiser, R. Ozeri, and J. J. Bollinger, Decoherence due to elastic rayleigh scattering, Phys. Rev. Lett. **105**, 200401 (2010).